Compton Image Reconstruction Algorithms and Demonstration Across Multiple Devices: From the Lab to the Field

by

Andrew Haefner

A dissertation submitted in partial satisfaction of the

requirements for the degree of

Doctor of Philosophy

in

Engineering - Nuclear Engineering

in the

Graduate Division

of the

University of California, Berkeley

Committee in charge:

Professor Kai Vetter, Chair
Professor Eric Norman
Professor Steven Conolly
Dr. Donald Gunter

Fall 2014

Compton Image Reconstruction Algorithms and Demonstration Across Multiple Devices: From the Lab to the Field

Abstract

Compton Image Reconstruction Algorithms and Demonstration Across Multiple Devices: From the Lab to the Field

by

Andrew Haefner

Doctor of Philosophy in Engineering - Nuclear Engineering

University of California, Berkeley

Professor Kai Vetter, Chair

Compton cameras image gamma-rays in the range from hundreds of keV to several MeV and are useful for a range of applications including astrophysics, contamination remediation, medical imaging and nuclear security. The data acquired from Compton cameras needs to be inverted to recover the desired gamma-ray distribution in space and energy using reconstruction algorithms. The focus of this work is the process of converting measured Compton camera interaction data into gamma-ray images via such methods. Several approaches are covered, including filtered back-projection and iterative methods. This work makes advances in each of these approaches both theoretically and through demonstration measurements. Some of these methods are optimized for real-time imaging.

Working in the Applied Nuclear Physics group at Lawrence Berkeley Lab and in Nuclear Engineering at UC Berkeley provided a unique opportunity to analyze data from three different Compton cameras. This provided a cross device perspective that ultimately made the imaging algorithms developed for one system more robust for another. Having this perspective also made it more clear which factors of the image reconstruction algorithms were essential. Using these different systems, techniques are described to analyze the quality of data that can be collected from a Compton imaging system. The three imaging systems cover a variety of semiconductor materials: Si, CdZnTe and HPGe. These devices range from lab development platforms to a small compact Compton camera device. The compact device, called HEMI, was taken to Fukushima, Japan and flown on a remote control helicopter to map the cesium contamination. The results from that measurement are detailed and shown.

Another focus of this work is sensor fusion with auxiliary data sources, which include visual cameras, depth cameras, GPS and IMU sensors. This is used to expand the number of reconstruction dimensions. This also provides contextual information for the gamma-ray intensity reconstruction and can be used to overcome some limitations with gamma-ray imaging, such as inherent low count rates. This approach of sensor fusion is demonstrated with lab measurements and the measurement taken in Fukushima, Japan.

Contents

Acknowledgments

Prof. Kai Vetter created the Applied Nuclear Physics group that allowed me to interact with multiple different imaging projects. He also created the environment where it was useful to learn cross discipline research, especially in computing. I am very grateful for having been a part of this unique research environment and having his constant support and guidance for heading in a fruitful research direction.

Don Gunter was a constant source of encouragement and was a daily inspiration. Many of the results here are due to his guidance and expertise. Typically Don would solve problems mathematically and I would test them programatically. This was a very fruitful collaboration and dynamic that I thoroughly enjoyed. Also, he was a great source of discussions about exotic math and physics concepts. His insights and enthusiasm were always a source of encouragement and made the work interesting.

The multi-device approach I have taken in this thesis would not be possible were it not for all the people who have built such incredible hardware and often provided data.

Ross Barnowski was an accomplice in research, and post-research beers. Our biggest accomplishment was the real-time acquisition and analysis software we co-wrote. He also maintained the CCI2 system which ensured a constant, reliable source of data.

Lucian Mihailescu provided a unique environment where we could explore imaging concepts, without judgement on the ideas. This was a valuable source of encouragement for innovative ideas and a great source of discussion for new topics.

I am grateful for Ryan Pavlovsky and Brian Plimley for providing data from the CCD detector. They also offered insights into the electron track data that proved useful.

HEMI was developed by a great team of people including Paul Luke, Mark Amman, Michelle Galloway and Andreas Zoglauer. It is rare to have access to a working and reliable piece of hardware, and that's what was achieved with HEMI. Additionally John Kua and others build the enclosure that allowed HEMI to successfully take data in Fukushima, Japan. And finally, the measurements taken in Fukushima would not have been possible without collaboration with the University of Tokyo and the JAEA.

Chapter 1

Introduction and Overview of Concepts

Gamma-ray imaging refers to the well-established method of mapping the spatial distribution of gamma-ray emitting objects by measuring the direction of the incident photon. It enables the reconstruction of objects in two or three spatial dimensions and, dependent on the detection modality, can enable the reconstruction of the energy of the incident gamma ray without depositing its full energy. Compton imaging is a technique not requiring collimation that works well in the range of a hundred keV to several MeV where Compton scattering is the dominant interaction mechanism. These materials are often man made, such as medical tracers, generated from nuclear power plants or from nuclear weapons. In medical imaging, known tracers are injected into patients to image metabolic functions in the body. Compton imaging has applications in astrophysics [8], in nuclear security and safety [27], and in biomedical imaging [39].

Compton cameras are one type of gamma-ray imaging devices that were conceived of 40 years ago [41]. Many advancements in semiconductor technology and electronics have improved Compton cameras in recent history. This work focuses on the algorithms and software used to process the data from advanced semi-conductor based Compton imaging systems. These algorithms have been developed and tested for three different Compton imaging systems. Often the aim of developing advanced software for processing Compton data is in overcoming some of the detector weaknesses, such as low count rate or sampling issues. In the past several years several Compton camera systems have become commercially available. One system is based on a single crystal of pixelated CZT [33]. Another is based on a strip HPGe design with mechanical cooling [31]. This recent commercialization shows promise for applications of Compton cameras.

1.1 Applications

Compton imaging has applications ranging across astrophysics, medical imaging, nuclear security and contamination remediation. One successful application of Compton cameras thus far has been in astrophysics. Comptel was a Compton camera that was deployed in space and produced results relevant to astrophysics, including the observation of an Al-26 line as evidence of nucleosynthesis in the galactic core [8]. Another system was flown on a balloon and successfully imaged the crab nebula [1]. Medical imaging remains an area of research for Compton cameras where it is demonstrated with imaging tracers in rodents[39] or designed as a system for proton beam range verification[35].

This work focuses on demonstration measurements related to nuclear security and safeguards. This includes unknown source identification in real-world environment and treaty verification of non-proliferation. A more recent application is contamination remediation specifically related to the nuclear reactor accident in Fukushima, Japan. Much of the contamination dispersed from the reactor accident is Cs-137 and Cs-134, which emit gamma rays in the energy range where Compton scattering is the dominant interaction mechanism. The common challenge of these applications is that the imaging domain is expansive, including possibly unknown source energies and locations. This includes not having prior information about the scene geometry. This is in contrast to medical imaging where the source domain is spatially limited to the patients body and the source energy is known. Compton cameras have a 4π field of view, making them a preferred device for wide area source mapping. These proposed applications have many computational challenges given the range of unknowns. Often, limits need to be placed on how the images are computed to make them computationally tractable. Additionally, in the case of cesium contamination in Fukushima, the source is distributed, which makes the reconstruction task more challenging compared to point sources.

Throughout this work, a variety of lab measurements were taken to demonstrate imaging concepts related to these applications. Lastly, a measurement was taken in Fukushima with a Compton camera and is discussed in Ch. 6. Throughout this work, a mixture of lab measurements and simplified simulations were used to test and compare different effects. Advanced gamma-ray transport simulations were not the focus of this work because simulations also offer much uncertainty.

1.2 Compton Scattering and Imaging

Compton scattering kinematics are discussed in this section as a precursor to the analytic approach to imaging used in later chapters. The approach shown here is basic, but useful for setting the stage for later work. A diagram of Compton scattering is shown in Figure 1.1. The diagram shows a gamma ray with direction $\vec{\Omega} \in S^2$ with $|\vec{\Omega}| = 1$ and energy E_0 incident on an electron at rest. The gamma ray then undergoes Compton scattering on an electron at rest. This generates two particles: a scattered gamma ray and an ejected electron. Each

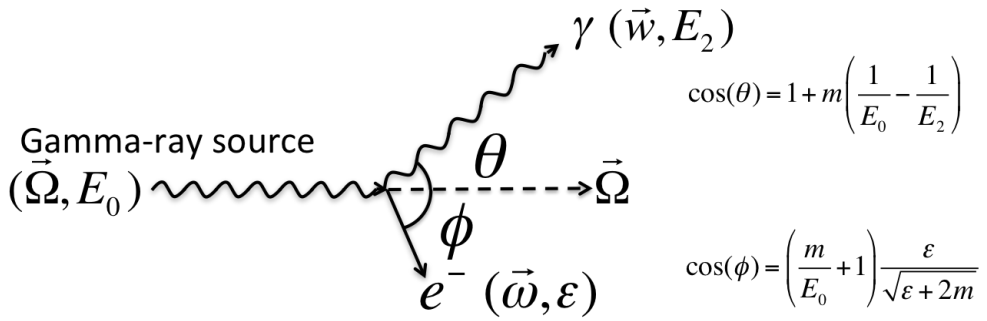

Figure 1.1: A diagram of Compton scattering.

of these particles carries information about the incident gamma rays.

First we focus on the scattered gamma ray. The gamma ray scatters at an angle of θ with direction $\vec{w} \in S^2$ where $|\vec{w}| = 1$ and energy E_2. Relativistic kinematics results in the following equation relating these parameters:

$$cos(\theta) = 1 + m_e \left(\frac{1}{E_0} + \frac{1}{E_2}\right) \tag{1.1}$$

$$cos(\theta) = \mu \tag{1.2}$$

Where m_e is the rest mass of the electron, E_0 is the initial energy of the gamma-ray and E_2 is the outgoing energy of the gamma-ray. This information can be related to the geometry of the scattering direction by the following equations:

$$\cos(\theta) = \vec{\Omega} \cdot \vec{w} \tag{1.3}$$

$$\mu_k = \mu_g \tag{1.4}$$

where μ_g is the geometric term from the dot product of the incident direction and outgoing direction and μ_k is the kinematic term. This gives a convenient relation of the geometry and kinematics of Compton scattering. Because $\vec{\Omega}$ and $\vec{w}$ are unit vectors, equation 1.3 is the equation for a cone, thus revealing the cone geometry for Compton imaging. This relation will be used in Ch. 3 to solve for the incident gamma-ray distribution. Working in this space of dot products has several advantages over working in the angular space, as will be shown later. Additionally, because this equation relates directly to imaging, it is useful as a metric space for gauging a systems imaging performance.

A similar analysis can be performed for the electron. The kinematics equation for the electron is as follows:

$$cos(\phi) = \left(\frac{m_e}{E_0} + 1\right) \frac{\epsilon}{\sqrt{\epsilon + 2m_e}} \tag{1.5}$$

$$cos(\phi) = \nu \tag{1.6}$$

where ϵ is the kinematic energy of the electron. The equation relating geometry and kinematics for the electron is as follows:

$$\cos(\phi) = \vec{\Omega} \cdot \vec{\omega}$$
$$\nu_k = \nu_g$$

This equation again reveals another Compton cone, albeit a different cone than the gamma ray based cone. These equations will be used in Ch. 4 to solve for the incident gamma-ray distribution when electrons are measured. It is interesting to note that Eq. 1.5 is separable into terms describing the incident gamma ray from terms describing the resulting electron. The relation of the electron cone and the gamma ray cone has been shown and discussed previously[55].

These equations are a simplification of Compton scattering. Specifically they do not include doppler broadening, which occurs in real Compton imaging systems because the electron is bound to an atom. This gives the electron an unknown initial momentum based on the binding energy of the atom. This is known to be the fundamental resolution limit for Compton imaging systems [56].

1.3 Compton Imaging Modalities

Different Compton imaging modalities result from the type of particle being measured and the variety of possible imaging domains. The particle can be the scattered gamma ray, the ejected electron or both. The different imaging domains result from combinations of the following: near-field or far-field; static or moving detector system; and single energy versus spectral deconvolution.

As will be shown throughout this work, the information of the incident gamma-ray distribution that can be determined from the two particles differs due to the scattering properties of the two resulting particles. Gamma-ray tracking has been used for several decades and has seen improvements as semiconductor detector technologies have evolved. More recently electron tracking devices have been developed as a result of improving spatial resolution of detector systems. Tracking electron trajectories inherently requires higher resolution systems because the charged particle nature of electrons results in a shorter interaction distance compared to gamma-rays. Measuring both particles simultaneously is not discussed in this work, but has been discussed in the past [53].

Throughout this work there will be a reference to the surface of possible gamma-ray directions. This refers to the possible locations in space and/or energy where a gamma-ray could have originated given the measurement of a single particle. This surface is different depending on the imaging modality and the assumptions made about the incident flux. The value of this surface is to relate the measured data space to the incident flux space. For example, in the simplest case of 2-D directional imaging where the incident energy is measured or assumed, a ring of possible directions results. When this surface is extended to 3-D it is a cone. More exotic surfaces result when the incident energy is not assumed. Some

different sources and modalities are listed in Table 1.1 and are discussed more thoroughly in the chapters dedicated to that modality.

Modality	Particle	Dimension	Assumption	Surface
Directional - Far field	gamma-ray	2	Energy Measured	Ring
Energy Image - Far field	electron	3		Hyperbolic
Volumetric Far field	gamma-ray	3	Energy Measured	Cone

Table 1.1: This table lists some properties about different Compton imaging modalities.

Conventionally, Compton imaging is based on the measurement of a sequence of Compton scattered gamma ray interactions followed by a photo-electric absorption measured in time coincidence as shown in event B in Fig 1.2. Based on the energy of the first interaction

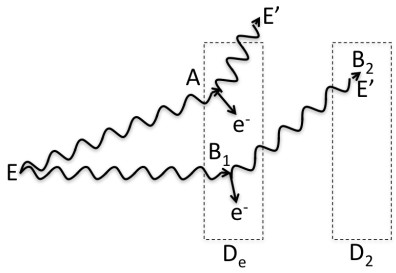

Figure 1.2: This is a schematic of Compton scattering events from a source at energy E. D_e represent an electron tracking detector and D_2 a position sensitive gamma-ray tracking detector. Conventional Compton imaging requires coincidence events like sequence B, while event A is lost to imaging. Our approach is applicable to either type of event and removes the requirement of having the second D_2 detector.

and of the full gamma-ray energy, the scattering angle can be determined. This scattering angle defines a cone of possible incident angles whose symmetry axis is given by the the locations of the first two interactions. Generally, sequencing of these interactions must be performed computationally for semi-conductor based systems because the timing resolution is inadequate to measure it directly[21]. Some fraction of events will be incorrectly sequenced and the effect of mis-sequencing is discussed throughout this work.

The scattering cone makes determining the gamma-ray incident flux challenging and thus inversion methods are needed to recover that distribution. Inversion methods and results based on gamma-ray tracking are discussed in chapters 3, 5 and 6.

More recently detectors have been developed that have fine enough spatial resolution to measure individual electron trajectories. Measuring the electron trajectories has several advantages for Compton imaging. Generally this information has been combined with

gamma-ray tracking devices to break the scattering cone symmetry and reduce the surface to an arc [6]. In this work, the ability to reconstruct the incident gamma-ray direction and energy distribution using only the electron track is presented[17]. This approach is described in Ch. 4.

The angular range into which the resulting Compton particles can scatter are different for the electron and the gamma-ray. A stationary electron can be scattered across a range of 90 degrees in the forward direction. The gamma-ray can scatter at a range of 180 degrees. This has implications for reconstructing the incident gamma-ray distributions. The main observation about the electrons scattering at a range of 90 degrees is that its surface of possible incident gamma-rays can be more easily transformed to retain the directional information, thus making an analytic reconstruction possible. This same technique is not easily extendable to gamma-ray tracking because the gamma-rays scatter across 180 degrees, thus transforming the surface of possible gamma-ray directions while retaining the direction information is not easily accomplished.

1.4 Image Reconstruction Overview

Image reconstruction is the general technique of recovering an image from measured data when the data and image spaces are different. Often it is possible to relate the incident flux to the measured data, either by an integral or statistical equation. The desired equation is the opposite: a transforms from the measured data to the distribution of interest. This general class of problems are called inverse problems, of which image reconstruction is a subset.

Image reconstruction techniques are widely used in medical imaging including CT, MRI, SPEC and PET imaging techniques. Due to the commercial success of medical imaging, much research has been done on image reconstruction techniques. Each of these imaging modalities offers its own complications for image reconstruction.

Compton imaging is another imaging modality that also requires image reconstruction techniques. Compton imaging offers unique challenges for image reconstruction not typically encountered in medical imaging. The geometry of the medical modalities is often projections along lines or planes, whereas the geometry of Compton imaging consists of cone surface projections. Some of the methods developed for medical techniques are sufficiently general that they can, and have been, applied to Compton imaging. One such technique that has had much success in MRI, wavelet de-noising, is applied to Compton imaging in Ch. 6.

There are two main types of image reconstruction algorithms: direct methods, such as filtered back-projection (FBP) and iterative methods, such as Maximum Likelihood-Expectation Maximization (ML-EM). These methods have fundamental differences in their formulation. FBP generally requires solving a set of integral equations, often relating to the geometry or kinematics of a specific imaging modality. This then leads to a filtering solutions, often in Fourier space, to remove data ambiguities at an the individual level. In the case of Compton imaging, this method overcomes the ambiguity from individual scattering

cones. Analytically solving these sets of equations can be challenging for imaging modalities with complicated geometry. Ch. 3 and 4 focus on FBP methods for Compton imaging.

Iterative methods are fundamentally a different approach. Iterative methods often result when a set of statistical equations are written, or when trying to use prior information in the form of penalty functions. An example iterative method, ML-EM for emission tomography, starts with the assumption that measuring gamma rays is modeled by a Poisson distribution due to the approach of counting individual photons. Maximizing this set of equations does not have a direct solution and thus must be solved by iteration methods. From this assumption, a set of statistical equations is generated that are used to compute the image reconstruction by iteration. This method is flexible and can be applied to nearly any Compton imaging modality. Much of the effort in using ML-EM reconstruction is centered around building accurate system matrices to adequately model the system and imaging modality of interest. Ch. 5 and Ch. 6 show results from iterative methods.

When FBP is analyzed from a statistical approach, it is equivalent to the assumption that the data has gaussian noise with uniform variance. This is not an accurate assumption given that the image noise varies with intensity. However, it works well in cases where high numbers of counts are expected, such as when measurement time is not limited, which can be the case for certain safeguards applications. FBP methods can still reconstruct images on a low numbers of counts, but this will create noise in the images.

1.5 The Need for Data Fusion

When trying to localize unknown sources in complex environments, Compton imaging can often suffer from low count rates. Also, when measuring gamma-ray distributions by moving a Compton camera through an unknown area, it might be impossible to acquire data on a sufficient path for accurate reconstruction, thus making image reconstruction in these situations an ill-posed problem. One possible way to overcome these issues is to use visual data in combination with gamma-ray data. This information can be used to constrain the imaging space and thus make the problem more tractable. Constraining reconstruction problems is a typical way to produce better results.

Additionally combining the gamma-ray distribution with visual information provides context to the location of the gamma-ray emitting materials. Otherwise ambiguous source distributions would be generated. Sensors that are useful for fusion with gamma-ray data include visual cameras, LIDAR, IMU and GPS. Data fusion with Compton imaging is demonstrated in Ch. 5 and Ch. 6.

1.6 Dimensionality of Compton Imaging, Towards 6-D imaging

Compton image reconstruction can be analyzed with regard to the dimensionality of interest for each modality. Generally when performing spatial Compton image reconstruction, a single source energy is measured or assumed. The most basic level of mapping gamma-ray distributions is measuring energy spectra. This can be thought of as a 1-D mapping problem in energy.

In the spatial domain, a 1-D spatial imaging example is GRETINA [22] which is a 1-D Compton imaging system for measuring short lived nuclear states for nuclear physics research. The single spatial dimension results from the source being constrained to the beam-line.

2-D spatial imaging can either be directional imaging, such as a far-field 4π system, or projection imaging where the image is reconstructed at a particular plane at a known distance from the detector. For Compton imaging, this means that the distribution of a single energy is being mapped. In practice, 2-D Compton imaging is performed when the detector is stationary. 2-D far-field imaging is the focus of Ch. 3.

Extending to 3-D spatial Compton imaging is achieved in one of two ways: either near-field or far-field. In the near-field case the source distribution must be sufficiently close to the devices so that the 3-D position within the detector can be used to reconstruct the depth of the source. This is often the case in medical imaging. In the far-field case, the detector moves in 3-D space. This requires tracking the detectors motion in space. One way to track a detectors movements is by using visual information and a Simultaneous Localization and Mapping (SLAM) algorithm [10]. This allows a detector to move freely in an imaging environment and its position can be determined by visual sensors. Ch. 5 demonstrates this approach.

Another approach to expanding the dimensionality of Compton imaging is to add an energy dimension to create a correlated spatial-energy image. 2-D directional imaging can be expanded with an energy dimension resulting in 3-D gamma-ray momentum reconstruction. Gamma-ray momentum implies that the gamma ray has direction and energy. This implies a stationary detector that can utilize the far-field approximation and also recover energy. This approach is demonstrated in Ch. 4 by measuring electron trajectories.

Higher dimensional imaging is possible when considering the direction of emitted gamma rays. Combining 3-D momentum measurements with 3 spatial dimensions leads to the ideal case of full 6-D gamma-ray imaging. This higher dimensional imaging could be useful in applications where shielding is present and is limiting the direction that gamma-rays can travel, which could be the case in safeguards applications. Researching image reconstruction at lower dimensional modalities can be seen as an attempt to approach the ideal case of complete 6-D imaging. It is conceivable that all of these approaches can converge to make this ideal case possible. The dimensionality of Compton imaging is mapped in Figure 1.3. Additional combinations of space, energy and direction are shown resulting in other pos-

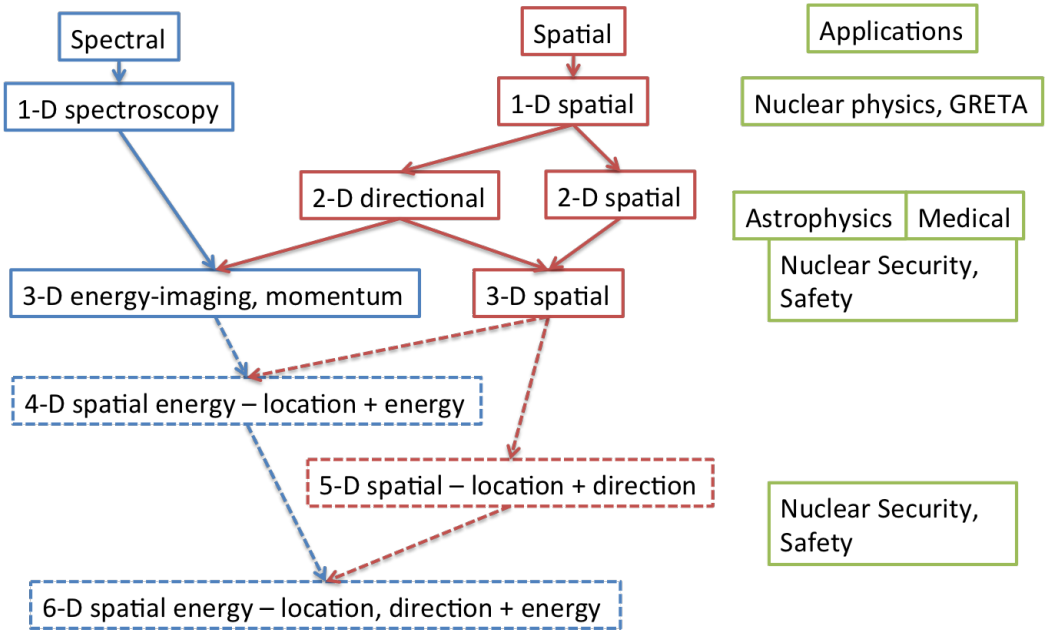

Figure 1.3: A visual representation for mapping Compton imaging domains is shown. Domains that include spectral deconvolution are shown in blue and connect back to the spectral box in the upper left. Domains shown in red are spatial domains at a single energy. Applications associated with each dimension are listed on the right. Domains that are dashed are yet to be achieved from Compton imaging.

sible reconstruction dimensionalities. This diagram organizes the reconstruction domains according to imaging a single energy, or trying to reconstruct the energies. Modalities that are represented in outlined boxes are yet to be achieved and represent recommended future research directions.

1.7 Compton Camera Device Imaging Quality

Analyzing the quality of Compton camera data can be challenging because of the high number of raw data dimensions. These dimensions consist of event time, position (3 coordinates), energy, and other parameters a system can measure. Converting the interaction data from energy and position to Compton cone data of direction and opening angle reduces the number of dimensions to 3. This is achieved when analyzing one particular source energy.

One metric that is used for Compton imaging is the angular resolution measure (ARM). The ARM is computed by measuring a point source at a known location and then computing the angular difference of the known source location and the angle computed from kinematics. ARM is however rather limited in describing a systems imaging performance, especially its ability to image extended sources. One limitation is that the image resolution can vary

across the field of view of the system, while the ARM reveals the image resolution at only one position.

From this work, a variation on the ARM is introduced that is a so called 2-D ARM plot. The 2-D ARM plot is a plot of the geometric dot product with respect to the kinematic cosine, both from Eq. 1.4. The geometric angle is computed from the dot product of the scattering direction and the known direction of the point source. The kinematic angle is computed from the energy deposited in the first interaction.

One use of this plot is to clearly show mis-sequenced events. An ideal 2-D ARM plot is shown in Figure 1.4. The line along $\mu_g = \mu_k$ shows where correctly sequenced events will occur. Events that are mis-sequenced are shown on the curved line, which is computed analytically using equation 1.1, and observed from experiment in Ch. 2.

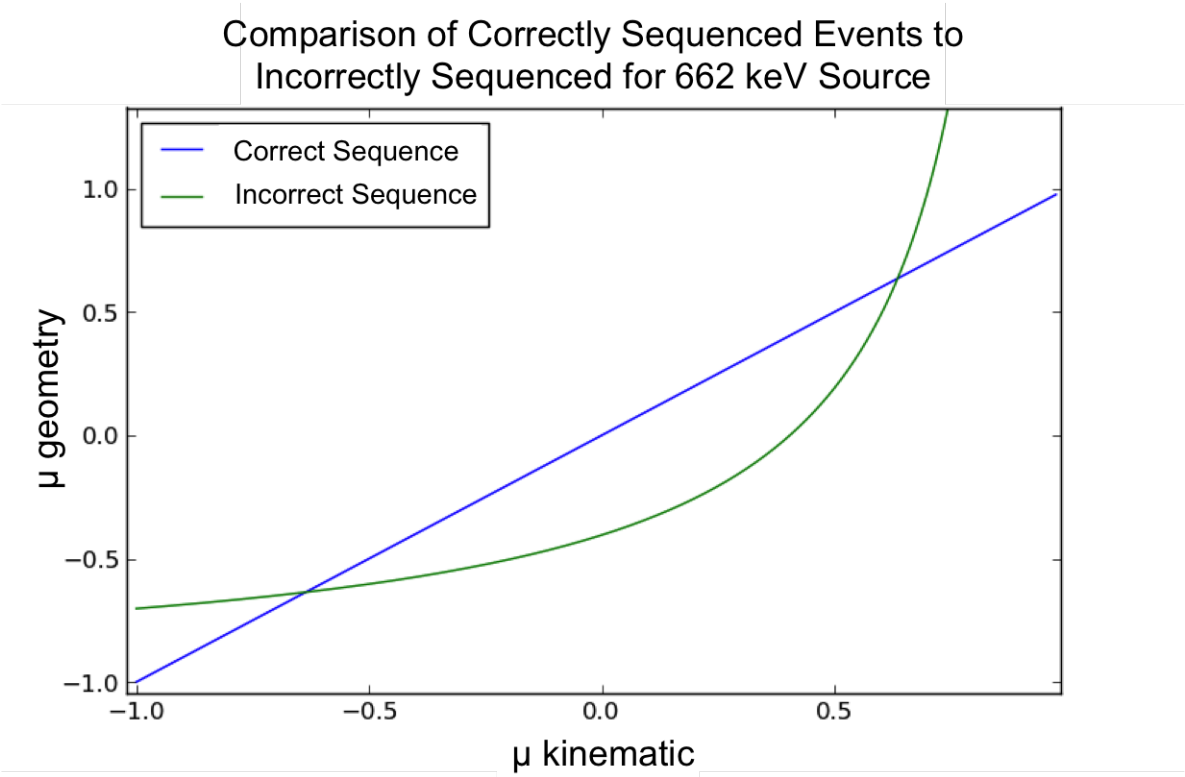

Figure 1.4: This plot shows analytically how mis-sequencing of two interaction Compton coincidence events can be observed. The axes compare the kinematic measurement and the geometric measurement. The blue straight line is from properly sequenced events. The curved green line is from events where the wrong interaction sequence is chosen. The physical limits of each of these axes are from -1 to 1. However, due to measurement errors, actual events can extend slightly beyond those limits. This curve is specific for a 662 keV source energy.

One insight of this work is the importance of data sampling for adequate image recon-

struction. This has been a major consideration in medical imaging, but has been somewhat neglected in Compton imaging. This is especially important for imaging extended or distributed sources distributions. The importance of sampling is compared in Ch. 2 and Ch. 6.

1.8 Image Convention

This work contains many 4π directional images. The imaging convention used in this work is to plot these images as a single 2D histogram, where the (0,0) point corresponds to the detector plane normal. Left to right in the image corresponds to rotating around the detector in the lab frame. Moving up to down corresponds to moving from above to below in the detector. Figure 1.5 shows a descriptive diagram of this orientation. The boundaries of this

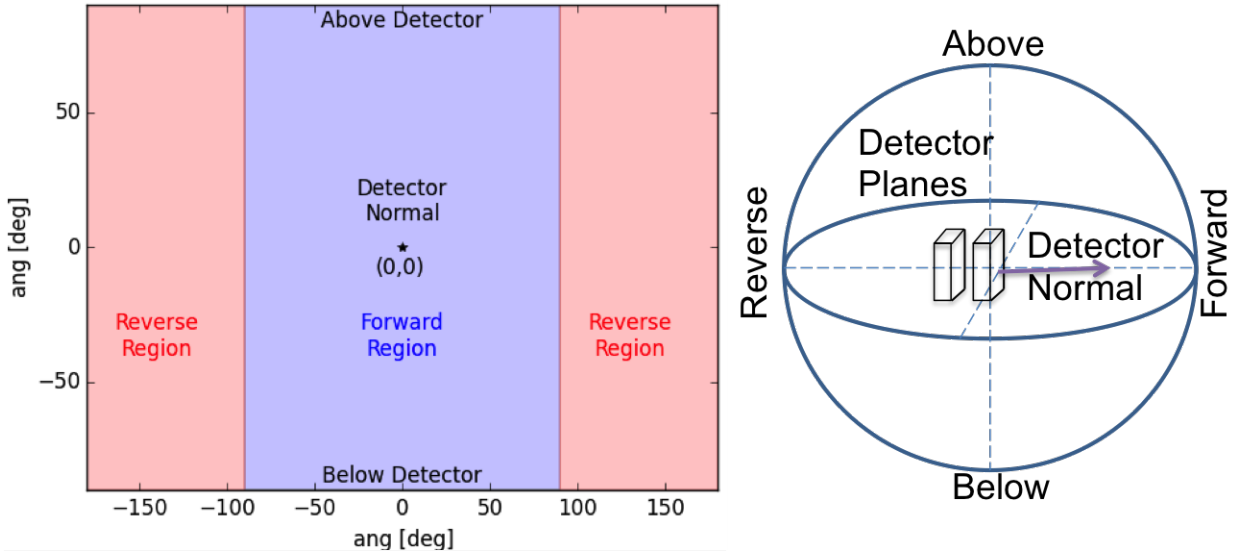

Figure 1.5: The orientation of far-field images are described in these figures. The figure on the left shows a labeled image. The figure on the right relates these descriptions to the 3-D detector geometry. The Compton camera shown in the 3-D diagram consists of multiple detector planes.

image are repeating because it represents S^2, the surface of a sphere.

1.9 Software Tools

All of the analysis performed in this work utilized the open source programing language Python. There is an especially rich set of open source tools for scientific computing built on Python. Common computational tasks often have an open source implementation. Choosing

Python allows for rapid testing and implementation of algorithms. Several of the algorithms in this work run in real-time with Python implementations. We have also built an acquisition framework with Python for several detection systems. This allows for relatively straightforward transition from algorithm testing to real-time implementation on an actual detection system.

Python also has many non-numerical computing abilities that allowed for the extension of reconstruction code in useful ways, such as computer networking. This was utilized to wirelessly transfer data between two computers, where one computer was used to acquire data from a system and a second to reconstruct Compton images.

A variety of packages were instrumental in this work including: numpy, scipy, cython, IPython, matplotlib and Mayavi. Numpy was used for efficient numerical array computing. Scipy was used for some typical numerical algorithms. Cython was used to optimize computationally intense numerical algorithms, especially for real-time usage[4]. Matplotlib was used for basic 2-D plotting[19]. Mayavi proved extremely flexible for producing all the 3-D plots shown here [34]. For interactive data analysis, IPython was a vital resource[30].

1.10 What This Work Does Not Cover

There has been a lot of research to make increasingly complicated systems models for Compton cameras[45, 50, 52]. When designing these systems models, much effort goes into developing and computing a model that can be system specific. One extension of these advanced systems models is energy-image deconvolution from Compton gamma-ray data, which is not covered in this work. This work focuses at a different level of the reconstruction task and concentrates on the reconstruction algorithms themselves. These reconstruction methods are then tested across different imaging devices. Additionally, the extensive work on weighting and systems modeling could be applied to the methods described here. The other common Compton imaging modality that is not discussed in this work is near-field 3-D imaging that is useful for medical applications.

1.11 Structure of This Work

The chapters of this work are organized in increasing complexity of imaging domains. Chapter 2 describes the imaging systems used in this work. Chapters 3 - 6 are demonstrations of different imaging modalities and are nearly standalone in their information. Those chapters are ordered by reconstruction complexity, starting with the case of imaging 2D far-field directional distributions. Then the dimensionality is increased by adding energy, but for electron track based systems. Following that, far-field 3-D spatial reconstruction is explored for gamma-ray tracking based systems. The last imaging chapter, Ch. 6 is dedicated to HEMI and the complications of imaging cesium contamination in Fukushima, Japan. That chapter contains a reconstruction method designed to overcome some of HEMI's limitations.

It also includes measured results from Fukushima where HEMI was flown on a remote control helicopter.

Chapter 2

Compton Imaging Systems - an Imaging Perspective

This chapter serves to described the imaging systems used in this work. The focus of describing the systems is to provide the relevant details about how they function from an imaging perspective. Details that are relevant to the image quality produced by each system will be discussed. The electronic workings of these systems has been described in previous publications and, except where relevant for imaging, those details will be spared. Additionally, some of the systems contain auxiliary visual and positioning sensors which are described here.

Three systems were analyzed throughout the course of this work including the following:

- Scientific Si Charge Coupled Device (CCD)
- Two plane, double sided strip HPGe detector (CCI2)
- High Efficiency Multi Modal Imager (HEMI), made of coplanar grid CZT modules [24] in a two plane configuration

These systems will be described starting from lab based development systems to a deployable imaging system. Additionally, the data quality of HEMI and CCI2 will be discussed.

2.1 Scientific Si-CCD

Scientific Si-CCD devices are being developed for Compton imaging applications. The ability to measure Compton electrons in these devices has been demonstrated [43]. A picture of the system is shown in Figure 2.1. This device has been developed and used successfully in astronomy applications in the UV to infra-red light ranges [18]. The scientific distinction of the CCD refers to having a larger active detection volume compared to conventional CCDs. This means it is sensitive to energy deposited across the entire 650 μm thickness of Si, compared to conventional CCD's that have an active thickness of about 10 μm.

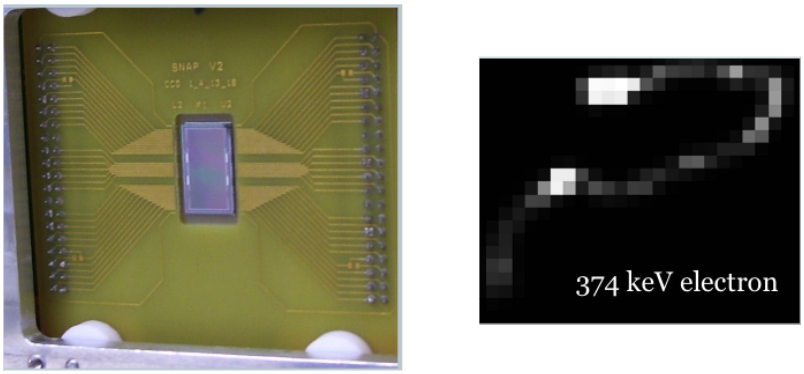

Figure 2.1: This shows a picture of the CCD system inside of its cryostat. The right picture shows one example electron track measured with this system.

This device has excellent spatial resolution with 10.5 micron pixels and thus can be used to measure individual electron tracks. The interactions of interest from this device are electrons generated from gamma rays that Compton scatter in the active Si volume. The ejected electron trajectory is then estimated from the electron track. This device offers the most sensitive information about Compton scattering.

The process of measuring the electron trajectory in the device is as follows. First, a Compton electron is generated in the active Si volume. That electron scatters randomly in the volume depositing energy along its path. The electron ejects electrons along the way that drift to the CCD charge contacts, producing a pixelated 2-D projection of the 3-D path. Individual electron tracks are segmented from the 2-D projection image. A ridge following algorithm is used to determine the direction of the electron in the plane of the CCD. Then the dE/dx is used to determine the direction of the electron out of the plane of the CCD. This approach is described in [32]. The resolution of determining the out of plane direction is worse than the in plane direction.

The concept of incorporating electron trajectory information for Compton imaging has generally been to combine that information with gamma-ray tracking. However, Compton imaging can be performed with only the data from the CCD. The algorithm to accomplish this is described and demonstrated in Ch. 4.

Current challenges, and active research areas for using these devices for Compton imaging include the following:

- Timing resolution - the readout speed of these devices is on the order of one second. This is inadequate for measuring time coincident Compton scatter events.
- Electrons can escape the active detector volume and thus not deposit their full energy.
- The directional resolution for measuring the electron trajectory is poor perpendicular to the pixel plane.

A strip CCD device is being developed to overcome the timing resolution by adding strips to the back side of the CCD. Better timing resolution is needed for using these devices as gamma-ray coincidence devices.

2.2 Compact Compton Imaging System

The Compact Compton Imaging (CCI2) system is a HPGe based Compton imaging system that utilizes gamma-ray tracking for its mode of imaging. A picture of this system is shown in Figure 2.2 This picture also shows CCI2 with a coded mask in front because it can also

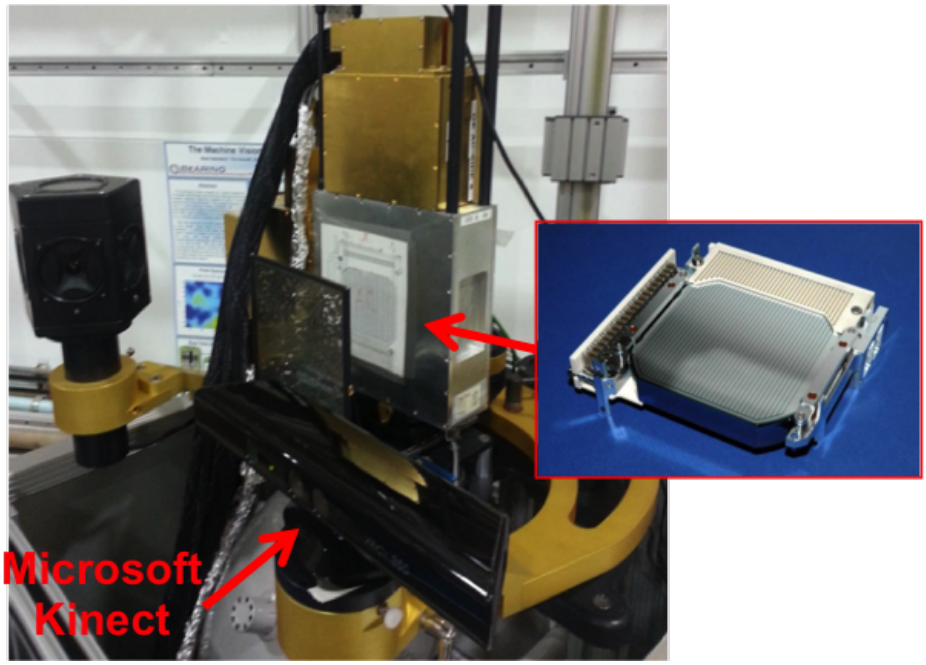

Figure 2.2: This shows the current version of the CCI system with its auxiliary sensors.

be used for coded aperture image. However, in this work the coded aperture imaging is not addressed and the measurements were taken without the mask present. The camera consists of two planes of double sided strip HPGe [44]. The strips on the front are orthogonal to the strips on the back. This orthogonality allows interactions to be positioned in the plane of the device. Neighbor strip transient signal interpolation can be used to obtain sub-pixel resolution. Depth information is gained from the timing difference of the signals from each side of the device. This results in position information with about 1 mm resolution in the device. The fundamental limit to position resolution of these devices is the path length the electron travels in the HPGe, which creates a charge cloud in the device. The ability to have depth information and sub-pixel resolution is important not only for improving imaging resolution, but also to have adequate event sampling for reconstructing extended objects. The importance of this event sampling is demonstrated and discussed throughout this work.

For this system, the imaging angular resolution at 662 keV is limited by the position resolution. This shows another potential advantage of using the CCD for Compton imaging because it can reduce the position resolution down to 10.5 μm.

Moving beyond just the Compton camera itself, CCI2 contains a Microsoft Kinect as an auxiliary visual sensor. In practice this allows for the collection of accurate 3-D visual information. Using this information allows for performing 3-D Compton imaging in arbitrary environments as described in Ch. 5. This system is currently a lab based development and demonstration platform.

Some of the challenges of this system are its weight resulting from the fact that it must be cooled to liquid nitrogen temperatures. However this weight comes with the advantage of this being a high resolution system compared to non-cooled CZT or scintillating systems.

2.3 CCI2 Data Sampling

The sampling requirements for Compton imaging are not well known. In CT imaging, the sampling conditions are known and are called Tuy's conditions [42]. In Compton imaging, the cone geometry of the scattering data complicates the mapping from the data space to the image space and makes data sufficiency conditions complicated to determine. For 4π directional imaging, the data space is 3-D and the imaging space is 2-D. It is possible that the system is over-determined but at the same time under-sampled due to detector geometry. Because these conditions are not known, the best that can be achieved is trying to cover as much of the sampling space as possible. This section shows some data analysis techniques to observe the quality of the data sampling for 4π directional imaging. These concepts are then demonstrated with the CCI2 system and later with the HEMI system.

A general convention for event sequencing is to use the higher energy event first for a 662 keV source [51]. Baysian methods have also been proposed for sequencing [54], however those are much more computationally demanding and thus not ideal for real-time applications. The effect of choosing the higher energy first can be observed. Alternatively, both possible cone directions can be used in an image reconstruction. This section will look at the effect on the data of these different sequencing choices.

Another common choice when using multi-plane Compton cameras is to only use the scattering events between different planes. The effect of this on the data will also be observed. One conclusion from these observations is that making these different choices does not have a big impact when imaging point sources. However, when trying to reconstruct distributed sources, more care needs to be taken with these choices. This section will focus on two approaches to analyzing the measured data. The first is to observe the scattering direction distributions. The second will be to observe the 2D ARM plot as described in Ch. 1.

To observe the effects described in this section and analyze CCI2's data performance, a Cs-137 point source measurement was taken with the source 2.5 m in front of the detector directly normal to the detection planes. From this measurement a variety of effects can be observed, such as event sequencing and data sampling. For the Compton telescope recon-

struction, the data space is reduced to 3 dimensions, two for the scattering direction and one for the cone opening angle. Visualizing these 3 dimensions can be challenging and usually requires reducing the data space to 2D. Thus the data plots shown here are for one source position, but this is sufficient to demonstrate the concepts. Events in a 6 keV window at 662 keV energy are used.

The scattering direction makes up two of the three dimensions of the Compton scattering data for far-field imaging of a single energy. These directions can be observed in a 2-D histogram of all measured scattering directions. This is shown in multiple plots in Figure 2.3. The top plot in this figure shows all possible scattering directions measured from a point source including one and two plane events and both possible sequencing directions. This figure shows that a large fraction of the sampling space is covered, albeit with some anomalies. This will be contrasted later with the HEMI imaging system which does not have as complete sampling. This plot is complicated to interpret directly for CCI2, but the effect of single plane events versus two planes events can be observed independently. The other two plots in this figure separate the distributions from two and single plane interactions respectively. The middle plot shows the scattering direction distribution for two plane events. In this figure there are two areas of interest. The center region representing events going from the back plane to the front plane. The blobs at the left and right of the plot represents events in the opposite direction, from the front to the back plane. It is important to note the empty space where events are not sampled. This shows one of the pitfalls in choosing only multi-plane events for image reconstruction, namely that a large fraction of the scattering space is not sampled. This can result in incomplete reconstruction or image artifacts, especially for distributed sources.

The bottom plot in Figure 2.3 shows the distribution of scattering directions for single plane events. These events cover portions of the space not sampled by the two plane events. It is important to note that depth sensing in the detection planes provides more sampling coverage of this space. As will be seen later, HEMI does not have depth sensing and the same plot from its data results in a much sparser sampling space. Thus depth sensing in planar Compton cameras is not only useful to improve image resolution, but also to better sample the scattering data space. The biasing in this distribution is caused by a combination of geometry and complications with event strip processing. This plot also demonstrates that single plane Compton camera systems have limited angular sampling.

The final scattering distribution plot shown in this section is the effect of choosing the higher energy first sequencing. Choosing the higher energy interaction as the first interaction is not always kinematically possible as there is a maximum energy for a Compton scatter. The maximum energy results when a gamma ray back-scatters and a source energy is assumed. Thus these events will actually be sequenced with the lower energy first. The scattering distribution from choosing the higher energy first is shown in Figure 2.4. This plot shows under-sampling in the center region, which corresponds to forward scattered events. This is caused by the fact that forward scattered events would have lower energy first as forward scattering deposits lower amounts of energy. This plot shows one pitfall with using only higher energy first sequencing as it reduces the sampling space for the scattering data.

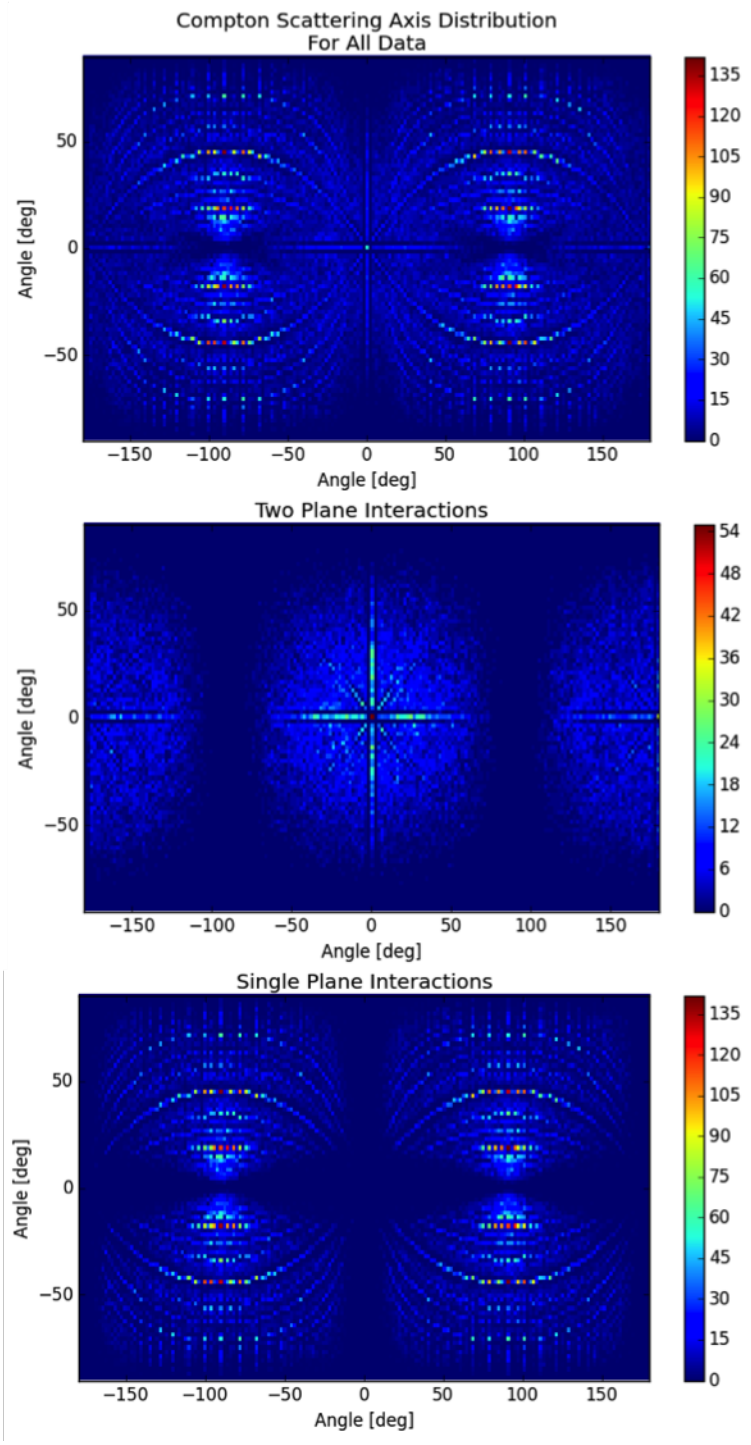

Figure 2.3: These histograms show the number of events measured in each scattering direction. The top plot shows all scattering directions measured by the CCI system. The middle plot shows only two plane Compton coincidence events. The bottom plot shows only single plane events.

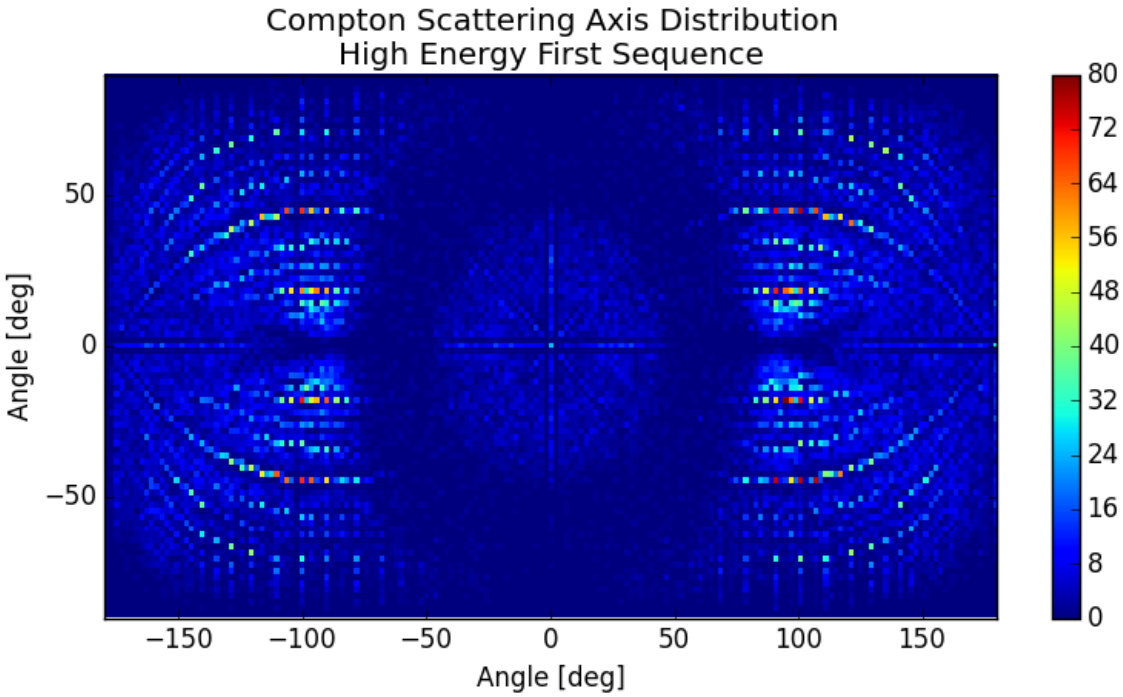

Figure 2.4: This shows the scattering distribution with higher energy first sequencing.

Now the focus will shift to how different events effect the measurement of a point source. The first plot considered is the 2-D ARM plot mentioned in Ch. 1. This plot is shown in Figure 2.5 and is represented as a 2-D histogram. The x-axis is computed from kinematics and the y-axis is computed from the known geometric position of the source. Correctly sequenced events have a one-to-one correspondence on this plot, and thus are represented by the diagonal straight line where $\mu_k = \mu_g$. There is also a curved line that represents mis-sequenced events. This plot shows horizontal streaking, which is the result of how timing information is processed for these events. The details of the events processing at the detector strip level will be discussed in detail in a future publication by Ross Barnowski[2].

We can now observe the 1-D arm plot for this same data, which is shown in Figure 2.6. Relating the 1-D and 2-D ARM plot is achieved by projecting the 2-D data along the line of correctly sampled events This figure is shown as the differences in cosine of the angle instead of difference in angular space. The expected peak at zero difference is observed, but an additional peak is observed from the mis-sequenced events. Specifically, the peak in the negative difference region corresponds to mis-sequenced single plane events. The ridge in the positive region corresponds to two plane backscatter events that are mis-sequenced as forward scatter. This is determined by observing the mis-sequenced events on the 2-D ARM plot and correlating where they will be projected on the 1-D ARM plot.

Now the effect of choosing higher energy first sampling on these ARM plots will be observed. First we can look at the 2-D ARM plot which is shown in Figure 2.7. The major

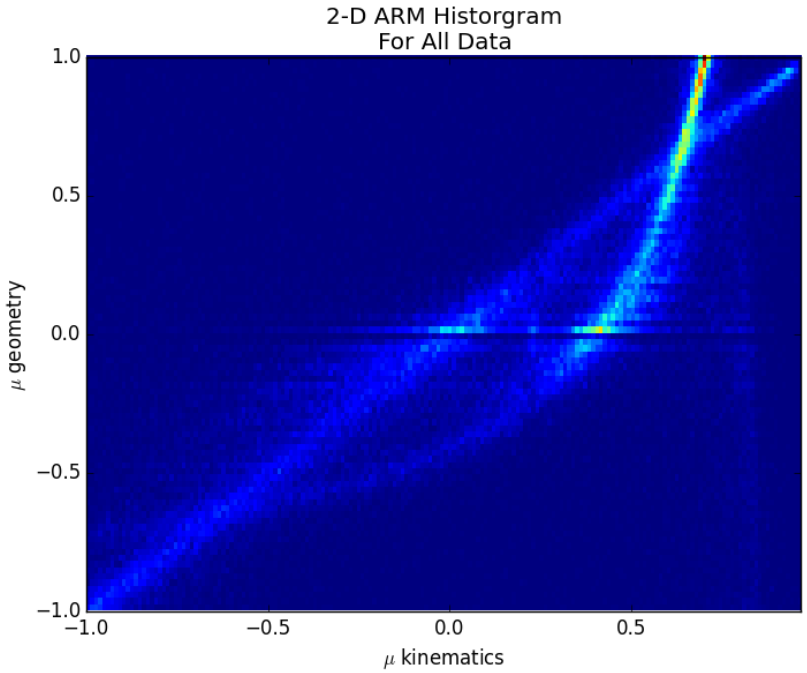

Figure 2.5: This shows a 2-D ARM plot for CCI2 data. The straight diagonal line is from correctly sequenced events. The curved line is from mis-sequenced events.

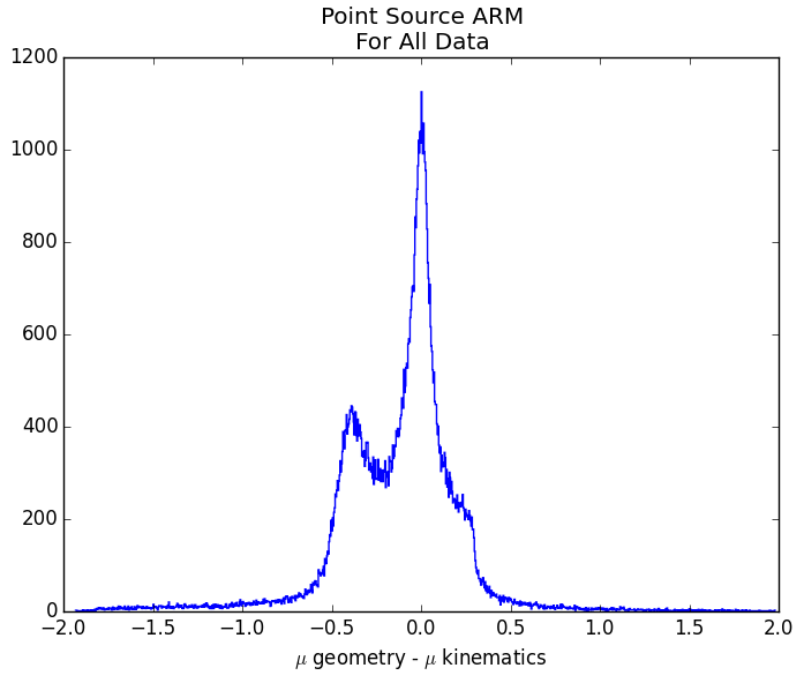

Figure 2.6: An ARM plot for all data. The data in this plot is the same as Figure 2.5.

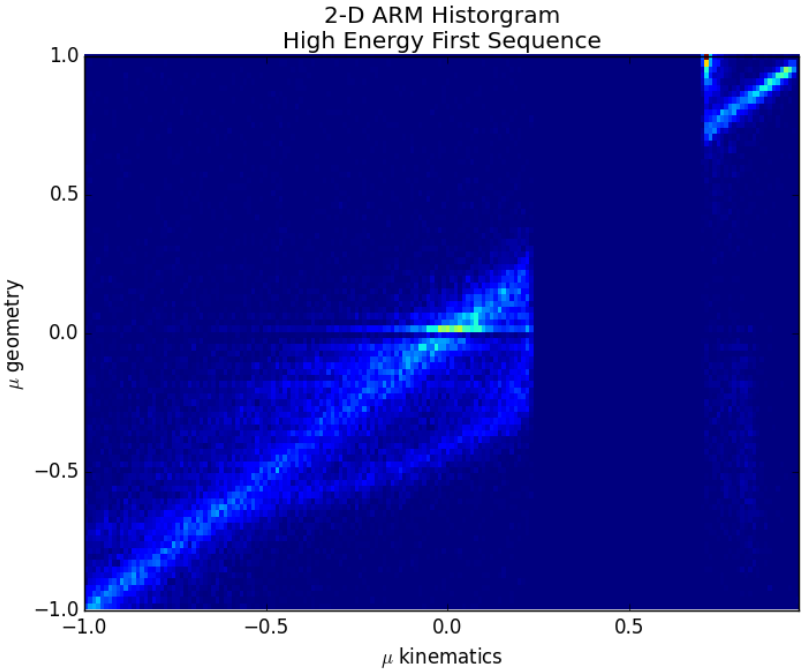

Figure 2.7: This shows a 2-D ARM plot with high energy first event sampling. Events that actually deposited the smaller amount of energy first would occur in the vertical strip where no events ever located.

difference of this plot when compared to the 2-D ARM that shows both sampling directions in Figure 2.5 is the region where no events are sampled. This is the location of events with the lower energy first. The events on the left half of the plot are from events sequenced with their higher energy first. The events on the right half of the plot represent events with energy too high to come from Compton scatter at 662 keV and thus were sequenced with the lower energy first. This plot shows one unexpected advantage of sequencing with the higher energy first: it covers the μ sampling space more completely. This happens because of the Compton scattering limit forcing some events to have sequencing with lower energy first.

The 1-D ARM plot from this higher energy first data is plotted in 2.8. This ARM removes some artifacts from the ARM with both sequence of events. There are still humps to the left and the right of the peak, which come from mis-sequenced events as observed from the 2-D ARM plot from this data.

2.4 High Efficiency Multimode Imager (HEMI)

HEMI is a multimode imaging system built with CZT modules that are 1 cm cubes. This system, in addition to auxiliary sensors, is shown in Figure 2.9 The multimode distinction in the name includes Compton imaging and coded aperture imaging. The coded aperture

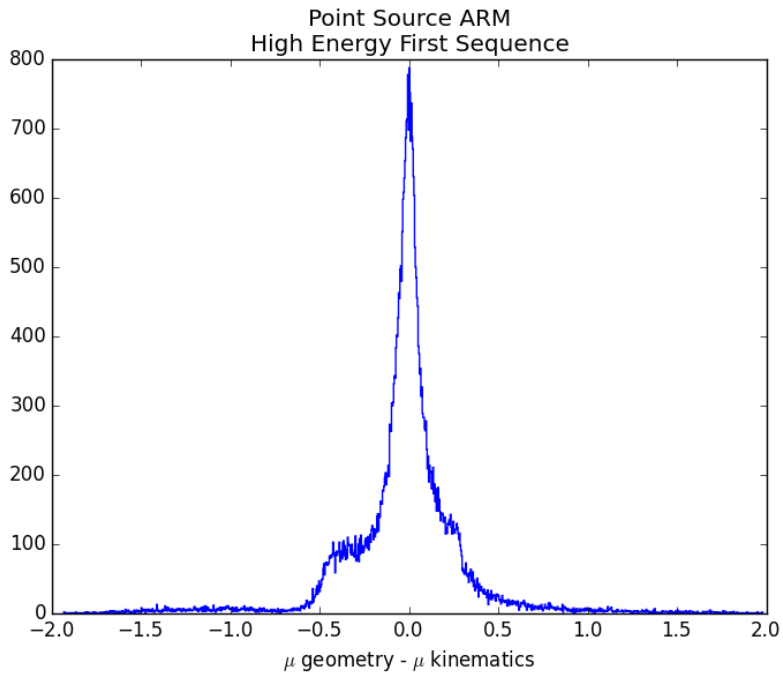

Figure 2.8: This plot shows the ARM plot for high energy first events. The asymmetric tails are caused by mis-sequenced events.

imaging is not addressed in this work and has be demonstrated previously [15]. The advantage of using CZT for a Compton imaging system is that no cooling is required and thus HEMI is a much more compact system compared to CCI2. Much work has been done to use CZT for Compton imaging by Zhong He at the University of Michigan. In his work, the CZT is pixelated to gain position information. HEMI is different in that each module of CZT serves as a pixel. This reduces the electronic complexity and event processing needed in the device, which reduces the size and weight of such a system.

HEMI contains 96 1 cm^3 CZT modules. The performance of HEMI has been characterized extensively in other work [13]. The imaging performance of HEMI is worse than that of CCI2 because it has broader energy resolution and larger position resolution. Additionally, it suffers from poor sampling conditions due to the large size of the pixels. This sampling issue is described in the next section.

HEMI was packaged with additional sensors for a demonstration measurement in Fukushima, Japan. In this configuration, HEMI was combined with a visual camera, a GPS, an IMU and an onboard computer. This package was then attached to a remote control RMAX helicopter. The results of this measurement are shown in Ch. 6.

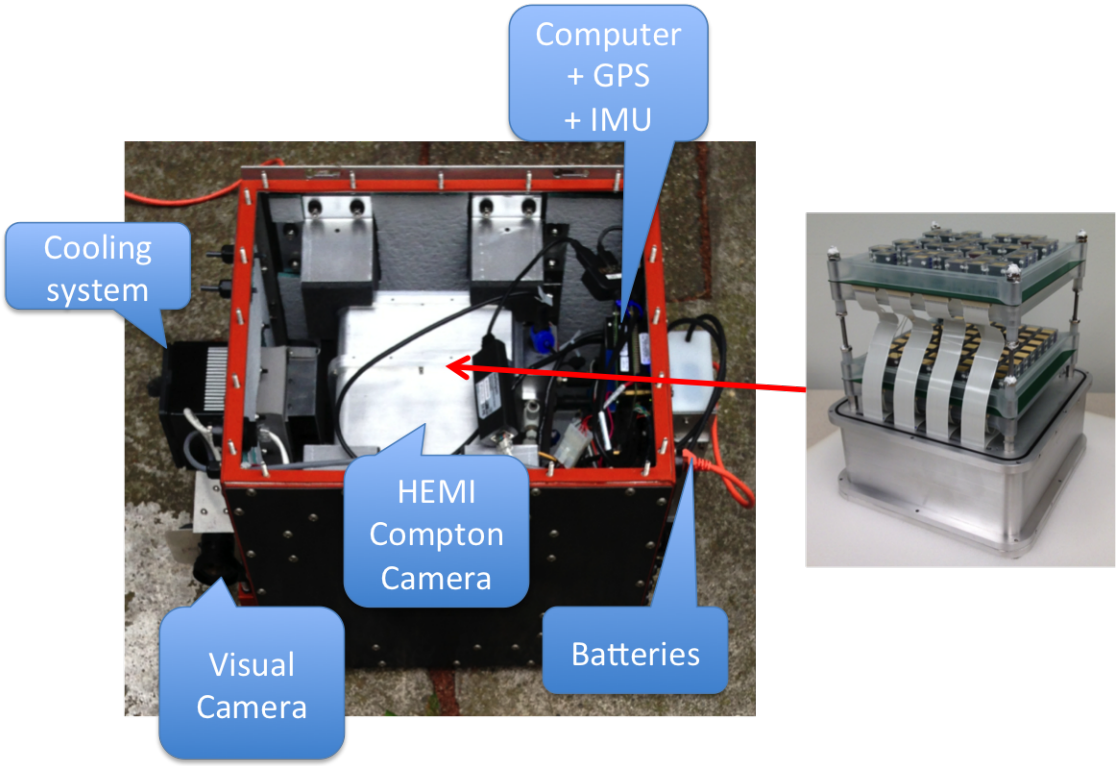

Figure 2.9: This shows a picture of the HEMI system with its auxiliary sensors. This is the packaged version used for helicopter flights.

2.5 HEMI Data Sampling

The data sampling of HEMI is explored in this section. A 50 μCi Cs-137 point source measurement is used to demonstrate HEMI's data sampling. The source was located on the axis normal to the detector face at a distance of 1.3 m in front of the detector. The duraction of the measurement was 5 hr. This long measurement time is not needed for imaging, but is useful to produce many events for the diagnostic plots. Scattering direction plots and ARM analysis will be observed for this point source measurement, as was shown with the CCI2 system previously in this chapter.

First we will observe the scattering direction histogram, which are shown in Figures 2.10 and 2.11. The difference between the two figures is the choice of background color where no events are sampled. Figure 2.10 has a blue background that helps to accent the biasing of the different direction. Figure 2.11 has a white background that accents the sparcity of the scattering direction sampling. The concentrated area in the center of the plot is from two-plane events, while the vertical lines at -90 and 90 degrees are from single plane events. The two plane events are challenging to see on the blue background due to geometric biasing, especially from neighboring pixel events which have the highest intensity on this plot. Figure

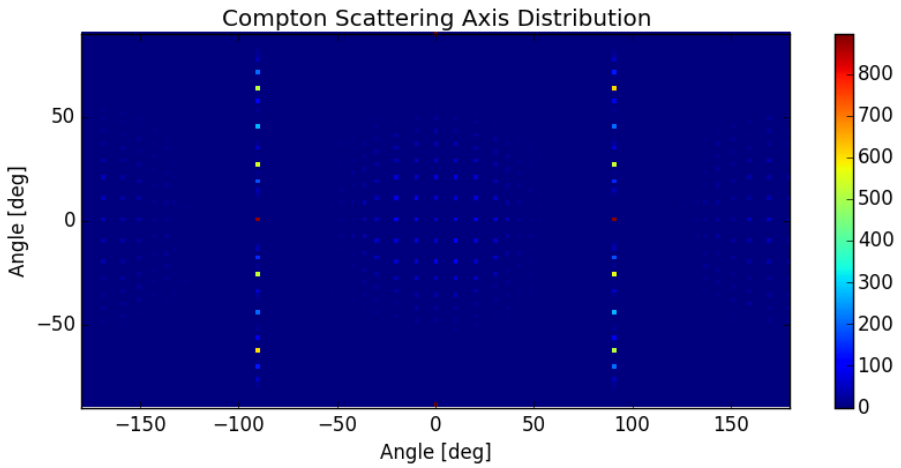

Figure 2.10: This shows the unweighted scattering distribution for a Cs-137 point source incident on HEMI. The events on a line at -90 and 90 degrees are from single plane events. The events in the center are from two plane coincidence events.

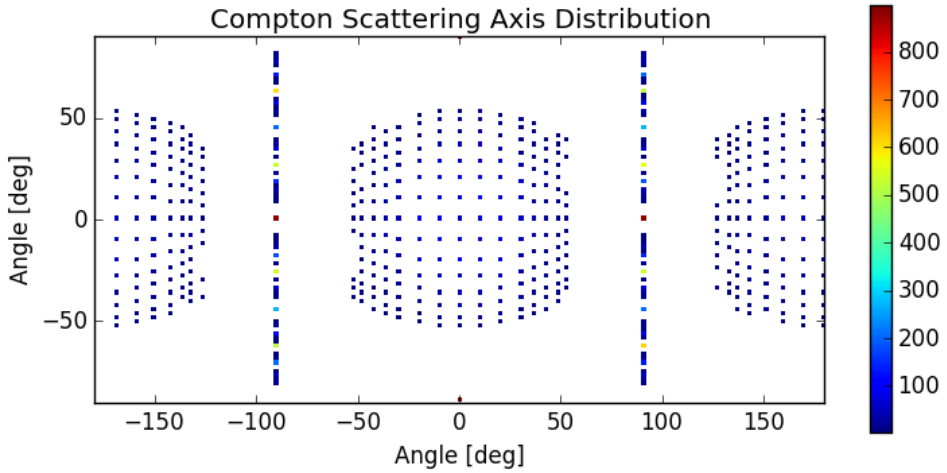

Figure 2.11: This is the same plot as Figure 2.10 except the areas that are not sampled are shown in white. This helps depict the exact areas that are not sampled. However, in this version it is challenging to see the biasing difference from single plane and two plane events.

2.11, where the areas that are not sampled are shown in white, displays several issues with this sampling. In the areas where there are two-plane events, the data are under-sampled and relatively sparse. The second issue is that ideally this space should be completely covered, however there are regions where no events are collected. One thing to note about the single plane events is that more directions are actually measured due to the extent of the individual crystals, however given the lack of position information within the crystal this

is a fair estimate for the measured direction. These sampling issues have implications for the possible accuracy of reconstruction, especially for distributed sources. Another issue is the biasing of the different scattering directions. This is partially a geometric effect caused by events with a shorter lever arm to be more probable. This can be compensated for with a L^2 weighting for each event where L is the lever arm, which is the distance between coincidence interactions. Applying this weighting to events creates a weighted version of this histogram, which is shown in Figure 2.12. This weighting makes the scattering distributions

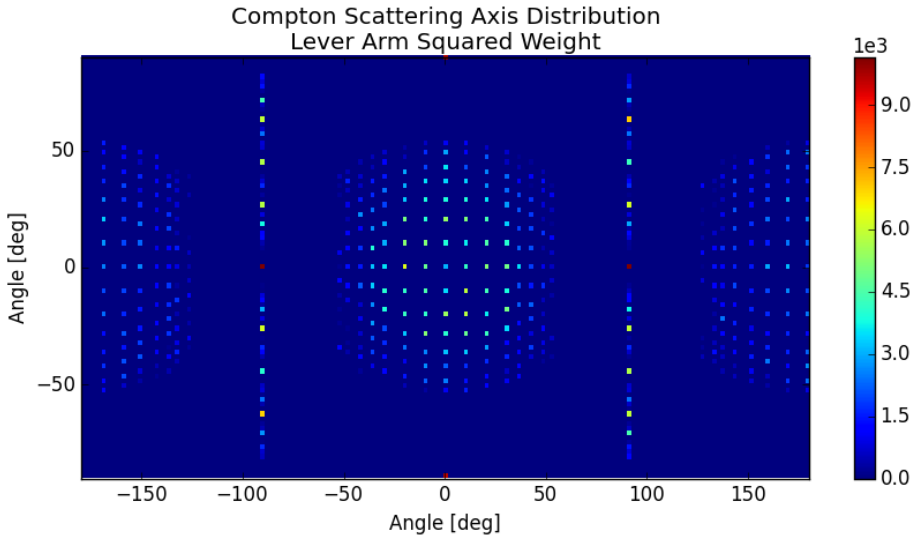

Figure 2.12: This shows the weighted scattering distribution for a Cs-137 point source incident on HEMI. The events on a line at -90 and 90 degrees are from single plane events. The events in the center are from two plane coincidence events.

more uniform and is especially important for recovering distributed or extended sources. The weighting also has the added benefit that events with short lever arm have broader imaging resolution. Because of this, they will create image artifacts if they are not properly accounted for with data cuts or weighting. One caveat with this weighting scheme is for low count rate images. In that case, adding this weighting will increase the image variance and can thus make the image look more noisy.

Another way to analyze this data is to look at the 2-D ARM plot described previously. Making this plot requires taking a point source measurement with a known location. The unweighted version of this plot is shown in Figure 2.13. The line of events at $\mu_g = 0$ is from single plane events. This is clear because the source was at the detector normal and thus single plane scatters were at about 90 degrees, which means the dot product is zero. The events in the upper right corner are foreword scatter events and events in the lower left corner are backscatter events. One thing to notice is the space where no events are collected. There are two horizontal regions on this plot where no events are located due to the lack of position information in the crystals. Comparing this with the same plot for CCI2 shown

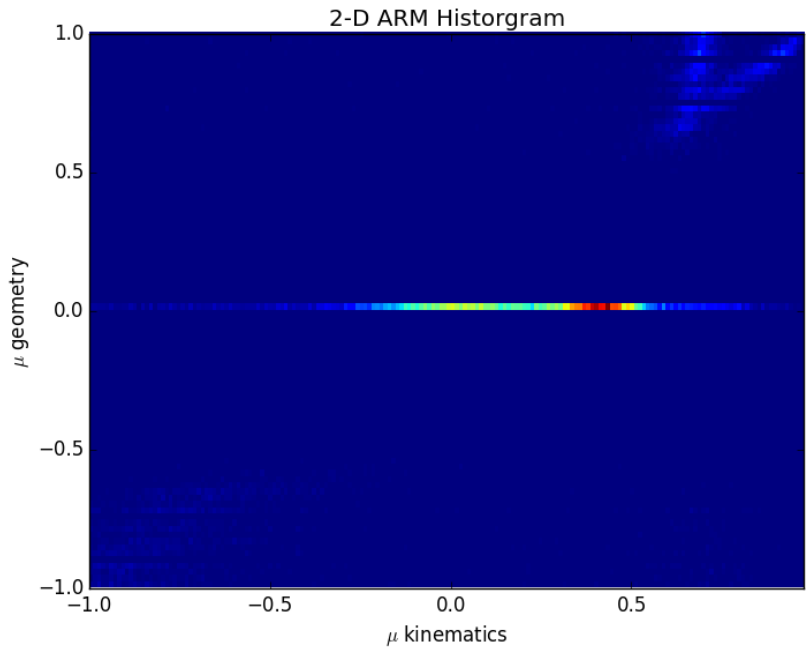

Figure 2.13: This shows a 2-D ARM plot for HEMI. The line across the center of the plot comes from single plane events, which are all at $\mu_{geometry} = 0$ due to the position of the source.

in Figure 2.5 reveals one of data sampling challenge with HEMI. Also this shows a large fraction of single plane events that get incorrectly sequenced, represented by the hot red region along the middle line.

Similarly to the CCI2 analysis, a 1-D ARM can be plotted, as shown in Figure 2.14. Again this shows an off-center peak that comes from mis-sequenced single plane events.

These ARM plots can also be improved and observed when the lever arm weighting is applied. Figure 2.15 shows the weighted version of the 2D ARM plot for this data. This plot shows some of the biasing being fixed compared to the unweighted version, especially comparing the single plane region to the two plane region. The weighted version of the 1-D ARM is shown in Figure 2.16. This also shows an improved peak compared to the unweighted version. Overall, HEMI does not sample the data space as well as the CCI2 system. These plots also show that data cuts and weighting have different levels of importance for different systems. For example, in this case HEMI appeared to have more geometric biasing compared to CCI2.

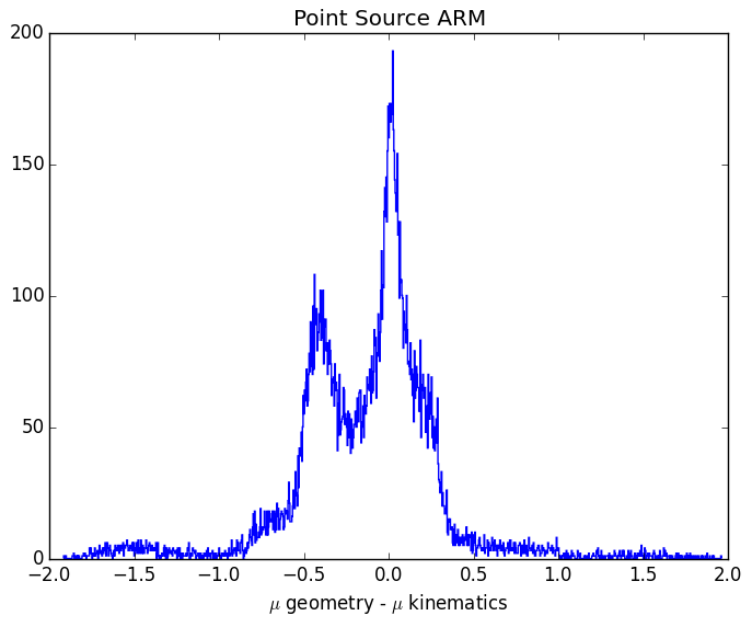

Figure 2.14: This shows the unweighted lever arm for a Cs-137 point source in front of HEMI. The prominent peak in the negative region is the result of mis-sequenced single plane events.

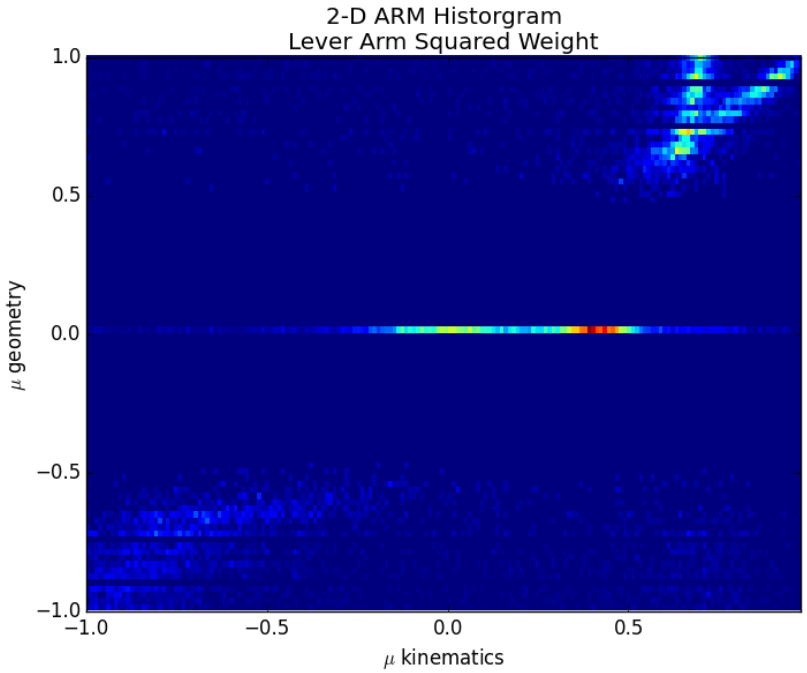

Figure 2.15: This shows the 2-D ARM weighted by the lever arm squared for a Cs-137 point source incident on HEMI. Some of the biasing is removed when compared to the unweighted version in Figure 2.13.

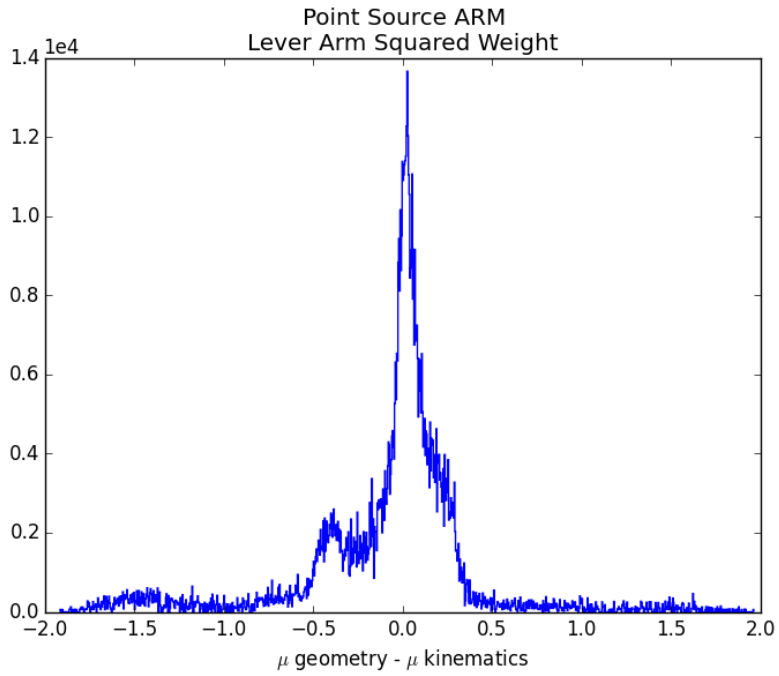

Figure 2.16: This shows an ARM plot for HEMI with the events weighted by the lever arm squared.

Chapter 3

2-D Directional Compton Imaging by FBP Algorithm

The focus of this chapter is on the reconstruction of 2-D far-field directional images from a Compton camera. In this imaging scenario, the detector is stationary and no auxiliary sensors are needed, although this type of reconstruction could easily be merged with a visual image. The reconstruction method in this chapter is demonstrated with CCI2, but this method is general to any far-field Compton imaging system, or any system resulting in cone data, such as neutron scatter cameras[26].

This type of reconstruction is often referred to as the Compton telescope problem. In the past, filtered back-projection solutions for Compton telescope data required sums of spherical harmonics or stereographically mapping the back-projection, which can result in imaging artifacts. This chapter presents a solution to this inversion problem that removes these complexities by embedding the 2-D directional image on the surface of a sphere S^2 into R^3 where it is easily solvable. In this manner 2-D Compton 4π imaging is related to the 3-D Radon transform, which has known solutions. To accomplish this, the cone data is converted to planar data. Additionally it is shown how the planar geometry can be used to produce a computationally efficient implementation.

3.1 Introduction and Background

This chapter focuses on 4π directional imaging with a Compton camera that is sensitive to gamma rays from all directions. A position sensitive gamma-ray detector with good energy and position resolution is required for Compton imaging. Compton imaging is conventionally based on the measurement of gamma-rays that interact in at least two distinct locations and deposit their full energy in the detector. The two-interaction coincidence requirement is one factor that limits efficiency in Compton cameras. Measurement of two interaction positions gives a scattering axis based on the direction from the first interaction to the second. Assuming full energy deposition, one can compute the scattering angle from kinematics using

the deposited energy in the first interaction. The incident direction of the photon and the scattering direction define a scatter plane. However, because the incident photon direction is not directly measured, the orientation of the interaction plane is not known, so that the angle of the incident gamma ray around this scattering axis is ambiguous, resulting in a cone of possible source directions. A diagram of this cone geometry is shown in Fig. 3.1

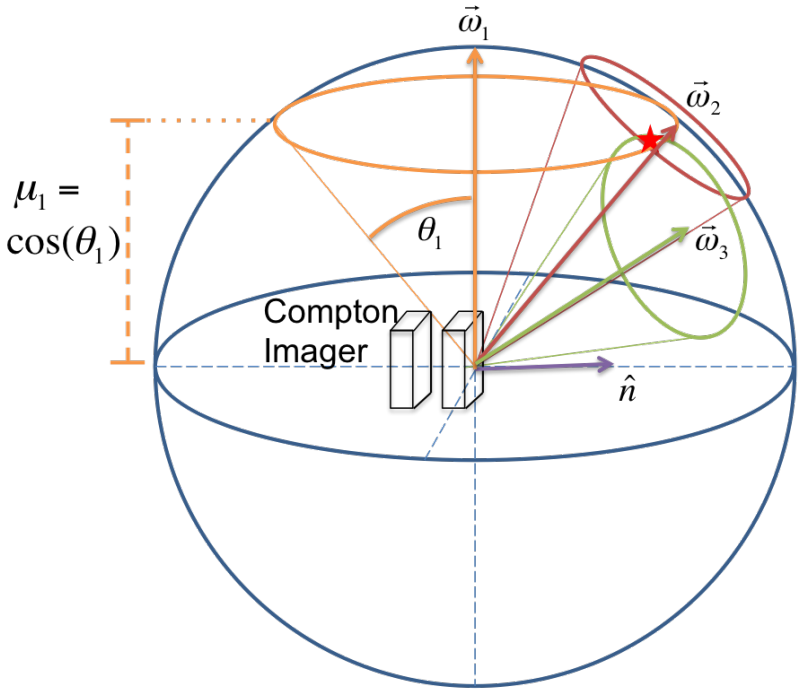

Figure 3.1: This schematic diagram illustrates three Compton events originating from a point source represented by a red star. Each event is characterized by a scattering axis represented by a unit vector $\vec{\omega}_n$ and a cone opening angle θ_n (which is labeled only for the first cone). All of the cones intersect the point source at the star. Two planes of detectors similar to CCI2 with the detector normal $\vec{n}$ are shown for reference. However, the actual location of interactions within the detector are unimportant, only the relative positions of interactions (which determine the scattering axis) are important in the far-field approximation.

Even if the scattering directions and opening angles (as determined by energy deposition and kinematics) where perfectly known, simple back-projection of this data would produce a blurred image. Thus, inversion methods are needed to enhance collective correlations in the data to overcome the ambiguity of individual cones. The most common reconstruction methods for Compton cone data include direct filtered back-projection (FBP) [52] or iterative Maximum Likelihood-Expectation Maximization (ML-EM) [48]. Filtered back-projection is a direct inversion method that requires representing the imaging modality as an integral equation. FBP approaches are generally more computationally efficient and can offer insights into a detector systems response, whereas ML-EM can be more computationally intensive.

The quality of an ML-EM reconstruction depends on the level of system detail. This makes a direct comparison between ML-EM and FBP methods challenging as ML-EM implementations are system-specific, while FBP is more system agnostic. In this chapter the focus will be on filtered back-projection methods.

This work incorporates several assumptions commonly employed in the analysis of Compton telescope data. One is that the energy of the incident radiation is known, based on either (1) *a priori* knowledge of the source spectrum or (2) determined from the measured spectrum. Relativistic kinematics then determines the opening angle of the Compton cone from the energy deposited at the initial Compton-scattering site. Implicit in this kinematic analysis is the assumption that the sequence of the gamma-ray interactions within the detector is known. In most Compton cameras, the timing resolution is inadequate for such interaction sequencing; the sequence must be determined computationally from analysis involving detector geometry, efficiency and differential scattering cross-sections. Improper sequencing of interactions will assign an incorrect Compton cone to an event, thereby causing imaging artifacts that can reduce image sensitivity. Despite these problems, we will assume for the remainder of this work that the interaction sequence is known unambiguously. Finally, we use a far-field approximation by only using the relative positions of interactions within the detector. The specific location of the initial interaction is not significant. This is demonstrated in Fig. 3.1. The diagram shows a generic Compton camera consisting of two planar detectors at the center of a sphere. The planes are shown for reference, however, neither the specific design nor the exact position of the initial interaction in the detector is required, only the scattering direction, determined as the vector connecting successive interactions, is used. This diagram is also used as a reference for results shown later in this paper. For Compton telescopes this far-field assumption is trivially satisfied, but for applications where the source is near the Compton camera, such as medical applications, this assumption may pose problems because the flux direction may vary significantly within the detector. Failure of the far-field approximation will blur the reconstructed distribution.

Previous Work

In the past several filtered back-projection solutions were found for Compton telescope data [29], [52]. These solutions involved modeling the back-projection as a convolution of a general point spread function (PSF) on the sphere. This approach does not explicitly express the cone geometry inherent to Compton imaging but instead applies generally to 4π directional imaging. Consequently, the PSF must be computed for the system, either analytically or by simulation. Based on this assumption of a generalized PSF, spherical harmonics are used to deconvolve the source distribution.

A more recent approach used Fourier techniques to deconvolve the source distribution by modeling the cone geometry explicitly via back-projection[16]. This was accomplished by stereographically mapping the spherical imaging surface to a plane. Stereographic projection onto a plane permits one to write the imaging equation as a convolution integral on the plane, which can be solved using Fourier techniques, thereby avoiding spherical harmonics.

Unfortunately, stereographic projection requires the selection of an arbitrary projection direction that is mapped to infinity on the projection plane. As a result, multiple projections are required in practice to cover the whole sphere. In the end, each of those multiple projections must be merged, which can result in imaging artifacts. The work presented here is an extension of the techniques used in that work.

In recent years several designs for Compton imaging systems have been developed; for example [47], [57] and [20]. The reconstruction algorithms associated with these systems are either simple back-projection or system specific ML-EM. An alternative reconstruction method that is easy to implement and robust while requiring relatively little information about the system is inherently valuable. The algorithm described here satisfies those requirements. This method is also useful for characterizing the parameters of a Compton camera, such as imaging resolution. This is advantageous over other reconstruction methods because ML-EM can produce artificially fine resolution due to its ambiguous stopping conditions, whereas, simple back-projection produces artificially broad resolution.

3.2 New Algorithm Formulation

The geometry of Compton cone data was illustrated in Figure 3.1, which shows how the cones intersect the imaging sphere to create rings. The key observation of this algorithm is the fact that a plane also intersects a sphere creating rings. Thus each individual cone can be substituted with the plane that creates the equivalent ring on the image sphere. This set of planes relates Compton camera reconstruction to the 3-D Radon transform, which can be inverted analytically (e.g. with a filter back-projection algorithm). Now this approach will be described mathematically.

The mathematical formulation of this approach involves the mapping between two distribution functions. First, one defines the incoming gamma-ray flux, $f(\vec{\Omega})$ with gamma direction $\vec{\Omega} \in S^2$ and units of photons per sec steradian, where $|\vec{\Omega}| = 1$. Then one defines $g(\vec{\omega}, \mu)$ as the measured cone distribution distribution with direction $\vec{\omega} \in S^2$ and cone opening angle $\mu = cos(\theta)$. The units of $g(\vec{\omega}, \mu)$ are events detected per sec steradian. The cosine of the scattering angle, μ is computed from kinematics using the energy deposited in the first interaction and the incident gamma-ray energy.

The measured data $g(\vec{\omega}, \mu)$ is given in terms of the incident flux distribution by the following integral equation:

$$g(\vec{\omega}, \mu) = \int_{|\vec{\Omega}|=1} \mathrm{d}^2\vec{\Omega} f(\vec{\Omega}) \delta(\mu - \vec{\omega} \cdot \vec{\Omega}) \tag{3.1}$$

The delta function in this equation ensures that the kinematic angle and the geometric angle are equivalent, where μ is from the scattering kinematics and the dot product of $\vec{\Omega} \cdot \vec{\omega}$ is the geometric cosine between the photon directions. This function generates cone data from the incident flux distribution.

Equation 4.1 can also be written as follows:

$$g(\vec{\omega},\mu) = \int \mathrm{d}^3\vec{x} f(\vec{x})\delta(|\vec{x}|-1)\delta(\mu-\vec{\omega}\cdot\vec{x}) \tag{3.2}$$

where the integration is now over R^3 instead of S^2. This allows us to combine terms as follows:

$$F(\vec{x}) = f(\vec{x})\delta(|\vec{x}|-1) \tag{3.3}$$

where $\vec{x} \in R^3$. This equation represents the incident flux as a 3-D distribution, albeit a somewhat artificial 3-D distribution whose only purpose is to facilitate the mathematical solution. The delta function in equation 3.3 will be used to recover the desired solution on the sphere at the end of the inversion. Using Eq. 3.3, Eq. 3.2 can be written as:

$$g(\vec{\omega},\mu) = \int \mathrm{d}^3\vec{x} F(\vec{x})\delta(\mu-\vec{\omega}\cdot\vec{x}) \tag{3.4}$$

This equation represents the measured Compton cone distribution as an integral over planes intersecting the spherical source space. We note that Eq. 3.4 is the 3-D Radon transform of $F(\vec{x})$. In this form, μ represents the distance to the plane and $\vec{\omega}$ is the normal to the plane. This is demonstrated in Fig. 3.4 where the colored points are the cone axis $\vec{\omega}$ plotted with their color as μ for a measured point source. This plot reveals the planar nature of the data as shown by horizontal iso-colors containing the same μ value. This shows that $g(\vec{\omega},\mu)$ can be thought of as a projection of the data in the source space onto the scattering axis, $\vec{\omega}$ at a distance of μ. Relating Compton imaging to the 3-D Radon transform is convenient because it has several known solutions. What follows is a solution convenient for list mode Compton imaging.

One now defines a back-projection integral that converts the measured cone distribution into a distribution of incident flux:

$$b(\vec{x}) = \frac{1}{2\pi}\int_{-1}^{1} \mathrm{d}\mu \int_{|\Omega|=1} \mathrm{d}^2\vec{\omega} g(\vec{\omega},\mu)\delta(\mu-\vec{\omega}\cdot\vec{x}) \tag{3.5}$$

This back-projection generates planes in R^3 from the measured cone distributions. For list-mode image reconstruction, this means that each cone generates a 2-D plane in the 3-D back-projection space. An example back-projection of 10 events is shown in Fig. 3.2. Defining this back-projection in 3D as opposed to the desired S^2 directional imaging space is key for the inversion.

Combining Eq. 3.4 and Eq. 4.3 one finds that:

$$b(\vec{x}) = \int \frac{\mathrm{d}^3\vec{y} F(\vec{y})}{|\vec{x}-\vec{y}|} \tag{3.6}$$

This is the 1/r result expected for a Radon transform. Interestingly this shows that the theoretical PSF from Compton imaging, or any form of cone based imaging, is the intersection

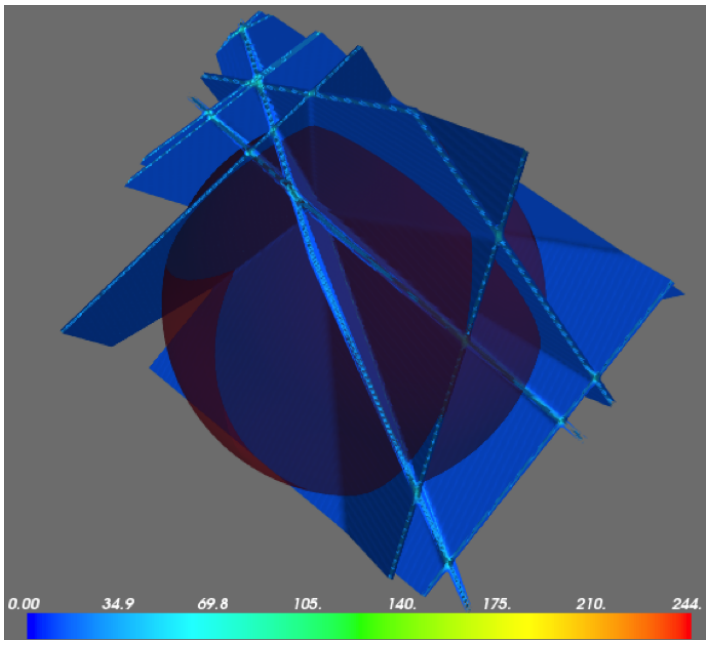

Figure 3.2: This shows an example back-projection for 10 events in the 3-D reconstruction space. Each plane corresponds to an individual Compton event. The red sphere represents the S^2 surface that indicates the location of the imaging solution. The colorbar is the intensity of the planes as they have widths that are determined by the Gaussian width of the back-projection as described in Eq. 3.11. The extent of the planes are limited by the 3-D grid on which the back-projection is computed. The intersection of the planes indicates the source direction.

of the unit sphere with 1/r in 3D. A sample back-projection of about 6.0×10^4 measured events from a point source is shown in Fig. 3.3. This figure shows the expected 1/r shape.

Taking the Fourier transform of Eq. 3.6, one recovers

$$\tilde{F}(\vec{k}) = |\vec{k}|^2 \tilde{b}(\vec{k}) \tag{3.7}$$

where $\tilde{F}(\vec{k})$ and $\tilde{b}(\vec{k})$ are the 3-D Fourier transforms of the source distribution $F(\vec{x})$ and the back-projection $b(\vec{x})$ respectively. This is the expected result for a Radon transform in R^n, which has the known $|\vec{k}|^{n-1}$ filter solution where n is the number of dimensions. The resulting $|\vec{k}|^2$ filter in 3D amplifies the high frequencies in compensation for the blurring introduced by the $1/r$ convolution of Eq. 3.6. Unfortunately, actual measurements include noise that is preferentially amplified at high spatial frequencies by this $|\vec{k}|^2$ filter. The effects of noise can be suppressed by many different strategies. For this work, Tikhonov regularization was used. For this application, the Tikhonov regularization fives a modified filter of the form:

$$\tilde{F}(\vec{k}) = \frac{|\vec{k}|^2 \tilde{b}(\vec{k})}{1 + \lambda^4 |\vec{k}|^4} \tag{3.8}$$

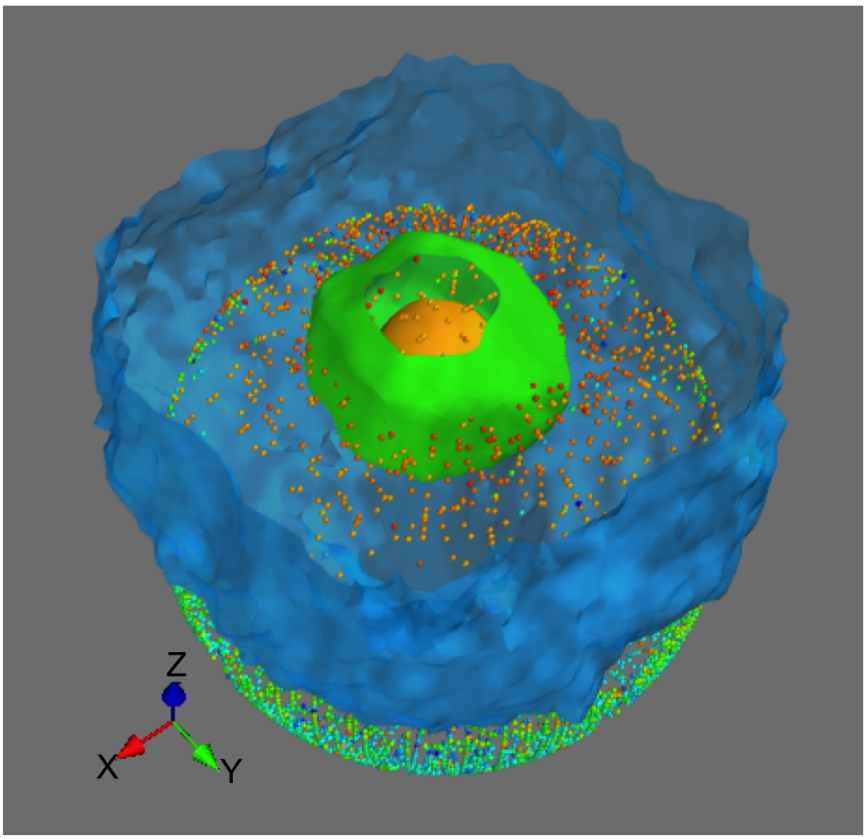

Figure 3.3: This shows an example back-projection of about 60 thousand measured events from a Cs-137 in the 3-D reconstruction space. The source is in the positive z direction. The iso-surfaces depict the back-projection intensity. The expected 1/r response shape is shown by the spherical iso-surfaces that encapsulate the source position. The blue surface has a somewhat square shape that comes from the 3-D square grid the back-projection was computed on. The plotted points correspond to the scattering axes for the individual cone events used to calculate this back-projection. The color of the points depicts the cosine of the cone opening angle, μ as computed from kinematics. Plotting the data points also shows the surface of the sphere where the desired image solution lies.

Here, λ is the Tikhonov parameter that can be adjusted as a trade-off between noise and resolution. Higher values of λ reduce high-frequency noise but at a cost of poorer image resolution from image biasing towards lower frequency.

One advantage of this approach over previous FBP solutions is that it reduces imaging artifacts inherent in other methods. This benefit is the direct result of the fact that the reconstruction is solved in a higher dimension than the image. Many artifacts that appear in the 3-D back-projection volume are subsequently discarded in the reconstructed 2-D image.

An example of filtered back-projection in the 3-D space is shown in Fig. 3.4. The surface at the right of the plot represents the filtered image result. The scatter points are the cone

data as described previously. The cone data is plotted to demonstrate the planar nature of the data and it shows the spherical surface where the desired image solution lies.

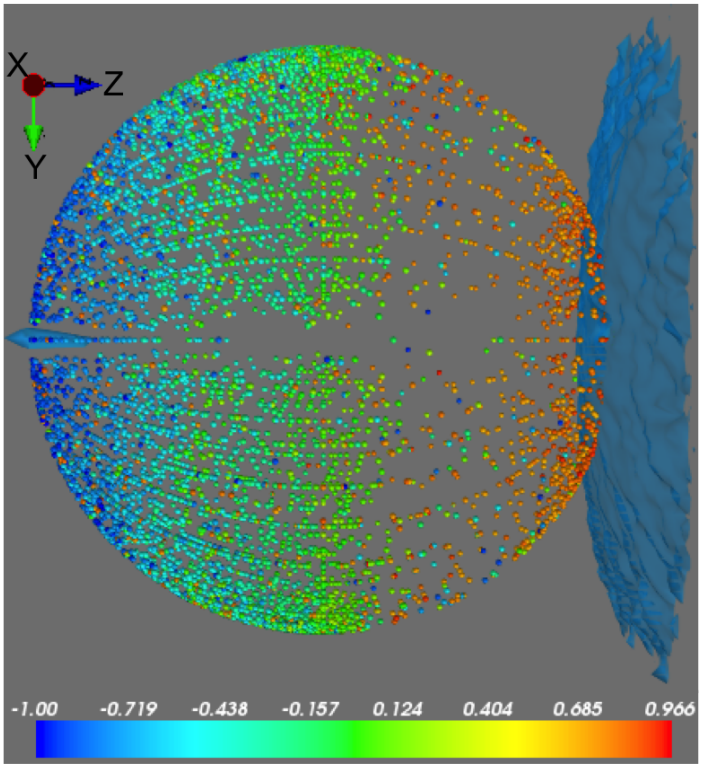

Figure 3.4: This plot shows two pieces of information: the Compton scattering data and the reconstructed surface. The point data is the Compton scattering direction with the color representing the scattering angle measured in detector. The surface data on the right of the figure is the filtered 3-D reconstruction. The point data is shown to indicate where the reconstructed image solution lies in this 3-D space. The point source is at the right side of the graph. The reconstructed surface is not point-like in 3D because of a reconstruction artifact on the edge of this space. However, this artifact does not affect the desired image on the surface of the sphere as shown in Figure 3.5. The small structure on the left corresponding to $\mu = -1$ is an artifact likely from mis-sequenced events.

After filtering the back-projection, a trilinear interpolation is then used to recover the desired image on the unit sphere as dictated by the delta function in Eq. 3.3. The final image from the data shown throughout this section is shown in Fig. 3.5 and is discussed in a later section.

3.3 Practical Implications and Implementation

As this method applies to Compton cones in general, it can be applied to any Compton imaging detector system without needing to explicitly compute the system response. In the previously presented formulation, detector effects were neglected and uniform distributions of scattering angles were assumed. Most Compton imaging systems have highly biased data due to coupling of system geometry with scattering distributions, represented by the Klein-Nishina formula. Extensive work has been done to account for those effects [52], [23] [45] and thus they will not be a major focus of this work. To incorporate some of these effects, the cone data generating equation, Eq. 4.1, can be modified to take into account various effects as follows:

$$g(\vec{\omega},\mu,p) = \int_{|\Omega|=1} \mathrm{d}^2\vec{\Omega} f(\vec{\Omega})\delta(\mu-\vec{\omega}\cdot\vec{\Omega})W_1(\vec{\omega},\mu,p)W_2(\vec{\Omega}) \tag{3.9}$$

where $W_1(\vec{\omega},\mu,p)$ represents efficiency relating only to the data parameters and p is an n-dimensional vector to keep track of additional data parameters, such as interaction positions $\vec{x}_1$ and $\vec{x}_2$. In practice we use:

$$W_1(\vec{\omega},\mu,L) = \frac{1}{L^2} \tag{3.10}$$

where $L = |\vec{x}_1 - \vec{x}_2|$ is the distance between interactions, often called the lever arm, for each event. This is a geometric factor that accounts for the fact that events with a shorter lever arm are more likely to occur. A straightforward way to determine this factor is to assume that once an interaction occurs, the probability that the next interaction will occur geometrically is $d^2/(\pi L^2)$ where d is the pixel dimension. If the assumption is made that all pixels are spheres then this becomes a constant for all events, then d^2/π can be ignored as it is constant for all events. Because these equations are inverted, each individual Compton event weighting will my multiplied by L^2. This has an added benefit because events with a shorter lever arm have worse angular resolution and as a result of this factor will have smaller weight. This reduces the need to make cuts in the data based on the value of the lever arm. The $W_2(\vec{\Omega})$ function encapsulates efficiency as a function of incident direction. For this work, this function is set to one. This function can be used to account for detector sensitivity anisotropies. These functions W_1 and W_2 must be greater than zero or properly regularized. Additionally due to the $\delta(\mu-\vec{\omega}\cdot\vec{\Omega})$ term of Eq. 3.9, effects dependent on $\vec{\omega}\cdot\vec{\Omega}$ can be incorporated into W_1. W_1 and W_2 can be incorporated into modified versions of $g(\vec{\omega},\mu)$ and $f(\vec{\Omega})$ respectively and the inversion is still solvable.

If these effects are not taken into account, this method can result in biased images, especially for extended sources where detector response is more critical. However, for point sources, which are often of interest in search and security applications, this imaging method is more robust to the exclusion of detector response.

The steps for computing this algorithm are as follows:

1. Compute the 3-D back-projection in Eq. 3.11 on a uniform 3-D rectilinear grid

2. Compute the 3-D FFT of the back-projection
3. Filter in Fourier space based on Eq. 3.7
4. Compute the inverse FFT of the filtered result
5. Generate points on the unit sphere and interpolate the image at those points from the 3-D filtered back-projection

These steps will now be discussed in more detail.

The first step is to compute the back-projection in Eq. 4.3. While that function includes a delta function, in practice a Gaussian function is used as an approximation. The equation for computing the back-projection from n events is as follows:

$$b(\vec{x}) = \sum_{i=1}^{n} \frac{1}{w_i \sigma_i \sqrt{2\pi}} \exp\left(\frac{(\vec{x} \cdot \vec{\omega_i} - \mu_i)^2}{2\sigma_i^2}\right) \tag{3.11}$$

where:

- the sum index i is over the list of cone events
- w_i is the weight for the individual cone, computed by Eq. 3.10
- σ_i is the Gaussian width of the cone in the cosine space

Here the width, σ_i can correspond to the uncertainty of the cone angle or be some small value. Using a cone width equal to the uncertainty in cone angle double counts the error, artificially worsening image resolution, Thus in practice it is best to use a small value, lower than the expected resolution, which also prevents pixelization effects of the individual cone. The result of this equation is that an individual plane is summed into the total back-projection for each measured Compton event.

The back-projection is computed on a uniform 3-D rectilinear grid to accommodate the computation of the Fourier transform in the filtering space. The range of that grid is from $[-(1+\alpha), 1+\alpha]$, where α is a small number to ensure that the edges of the unit sphere are fully enclosed within the grid. In practice a value of $\alpha = 0.5$ has been used. α should be sufficiently large to ensure that edge effects show in in Fig. 3.4 do not degrade the image quality. Using too large of a window will reduce the resolution of the grid used for computation.

Improving the speed of the back-projection computation can be achieved by taking advantage of the plane geometry of events. To achieve this for a single plane, two of the three back-projection dimensions are fixed based on the back-projection grid, then the third dimension is computed based on the equation for a plane. The contribution to the total back-projection from that individual event is then summed near the corresponding grid points.

This reduces the 3-D back-projection computation from $O(n^3)$ to $O(n^2)$, where n is the number of pixels in each dimension. This optimization dramatically reduces the computation time for the back-projection.

Steps 2 and 3 involve computing the 3-D Fourier transform of the back-projection; then applying the appropriate $|\vec{k}|^2$ filter with the Tikhonov factor. For real-time applications, the Tikhonov parameter can be implemented as a user controllable parameter. This allows the user to broaden the resolution for low count rate situations, such as at the beginning of an image acquisition when there are fewer counts and a noisier image. As more counts are collected the Tikhonov parameter can be reduced to improve resolution.

3.4 Measured Results

Point Source Results

In this section we demonstrate measured results taken with a two plane double sided strip HPGe detector [44]. As a simple demonstration measurement, a 50 μCi Cs-137 point source was positioned perpendicular to the detector planes at a distance of about 1 m for 1.5 hours. This results in about 4 degrees error from the far-field approximation. All detected and reconstructed 662±3 keV events were used in these images, resulting in 61,423 events. The image resulting from this measurement is shown in Fig. 3.5. To construct this image, events were selected in the 662 keV energy window. The origin in the following images corresponds to the detector normal. The data shown in this image is the result of interpolating the 3-D filtered back-projection as given by step 5. The angular width of the reconstructed source is 8.2 by 9.1 deg FWHM. Fig. 3.6 shows the same data with a lower Tikhonov value to demostrate the trade off between noise and resolution. The image in that figure has a resolution of 6.2 by 7.6 deg FWHM but the signal-to-noise ratio is degraded.

This algorithm can also perform with a small number of events. This is demonstrated in Fig. 3.7 that contains the first 100 full-energy events from the same data set that was used to create the images in Figs. 3.5 and 3.6. This number of events corresponds to the first 9 seconds of acquisition time and demonstrates that the source is localized quickly, albeit with a relatively noisy image. To produce the image, a higher Tikhonov filtering value is needed to compensate for the lower number of events, which results in degraded resolution compared to the high count rate case in Fig. 3.5.

Extended Source Results

This reconstruction method was also tested with extended sources. A 50 μCi Cs-137 point source was rotated in a plane parallel to the detector planes at a distance of 35 inch from the front of the detector. The radius of rotation was 14 inch with a measurement time of 148 min. The experimental setup is shown in Figure 3.8.

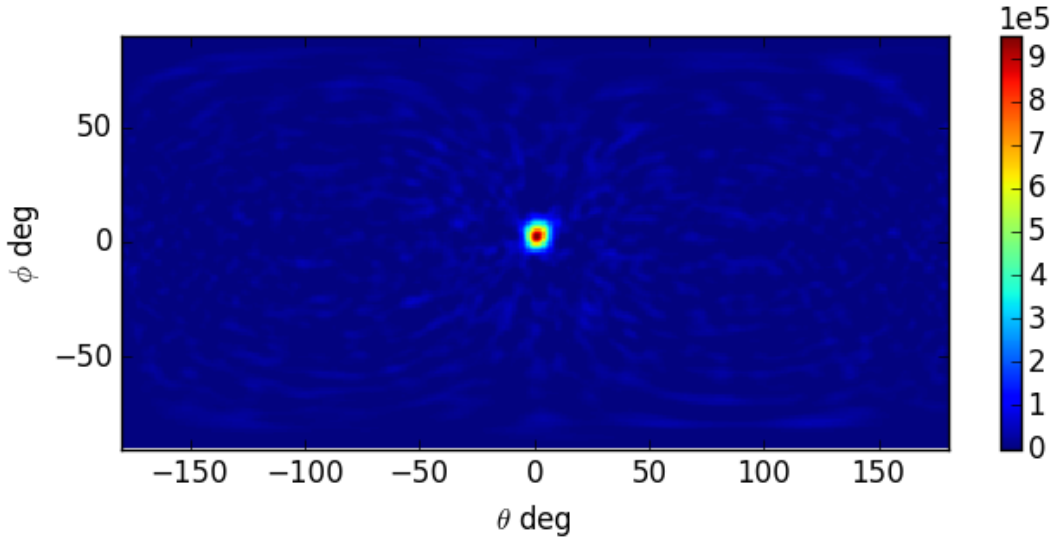

Figure 3.5: Example point source image placed in front of detector planes. The Tikhonov parameter is 0.045 which gives a resolution of 8.2 and 9.1 deg FWHM in each angular dimension.

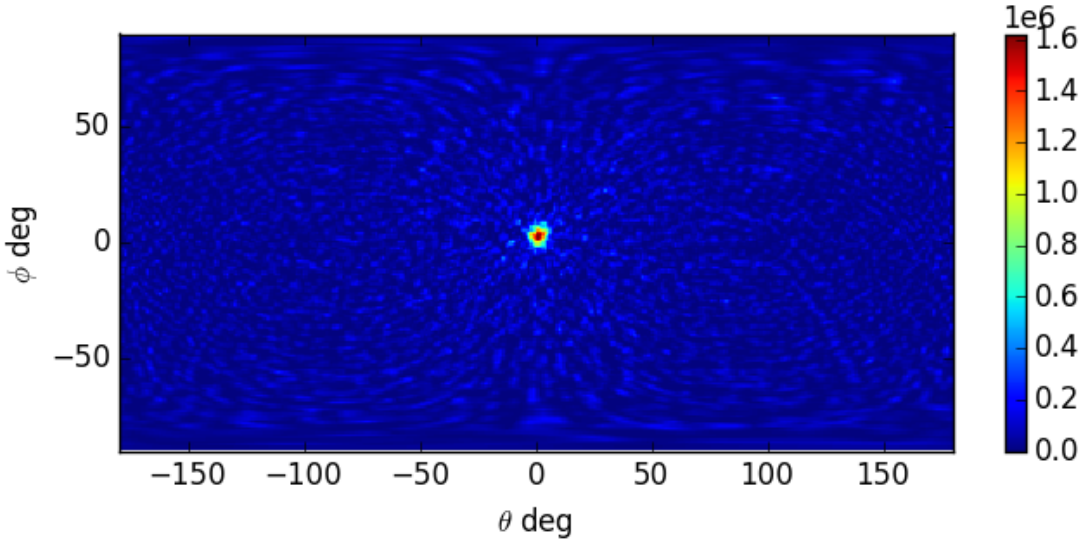

Figure 3.6: Example point source with same data from Fig. 3.5 with a Tikhonov value of 0.031. The resolution is improved to 6.2 and 7.6 deg FWHM, but with a reduction of signal-to-noise in the image.

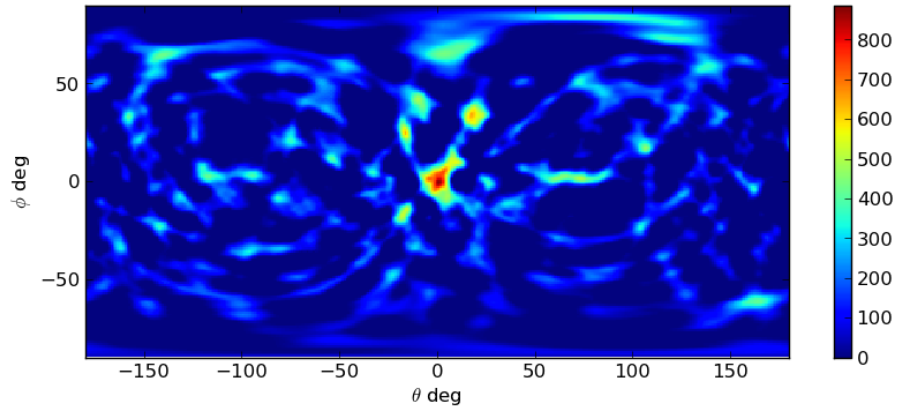

Figure 3.7: This shows an example point source with same data from Fig. 3.5 using only the first 100 events, which is equivalent to 9 sec of acquisition for 50 μCi at 1 m. The Tikhonov value is 0.447 with a resolution of 10.6 and 14.5 deg FWHM for each dimension.

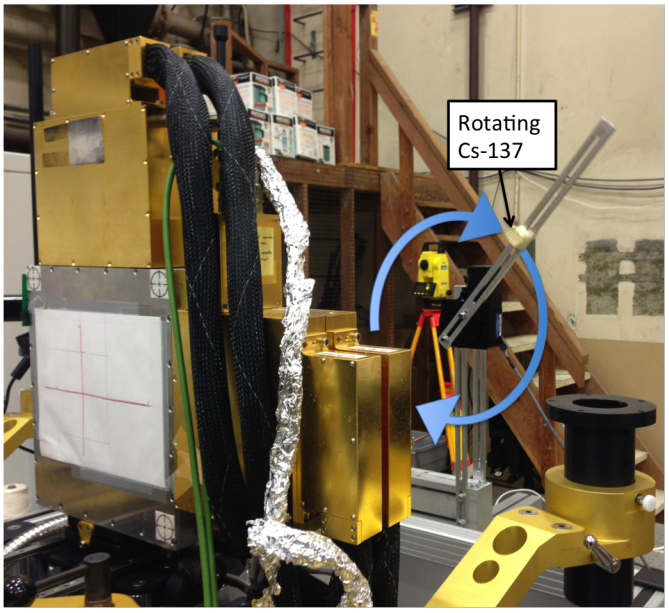

Figure 3.8: The experimental setup for a rotating Cs-137 source is shown.

This measurement resulted in 34,779 Compton coincidence events that were all used in the image. The simple back-projection before this algorithm is applied is shown in the Fig. 3.9 for comparison. The application of the filtered back-projection algorithm to this rotating source data is shown in Fig. 3.10. The width of this reconstructed ring is 9.85 deg. Accounting for the geometric weighting as described in Eq. 3.10 was vital for the result of this image.

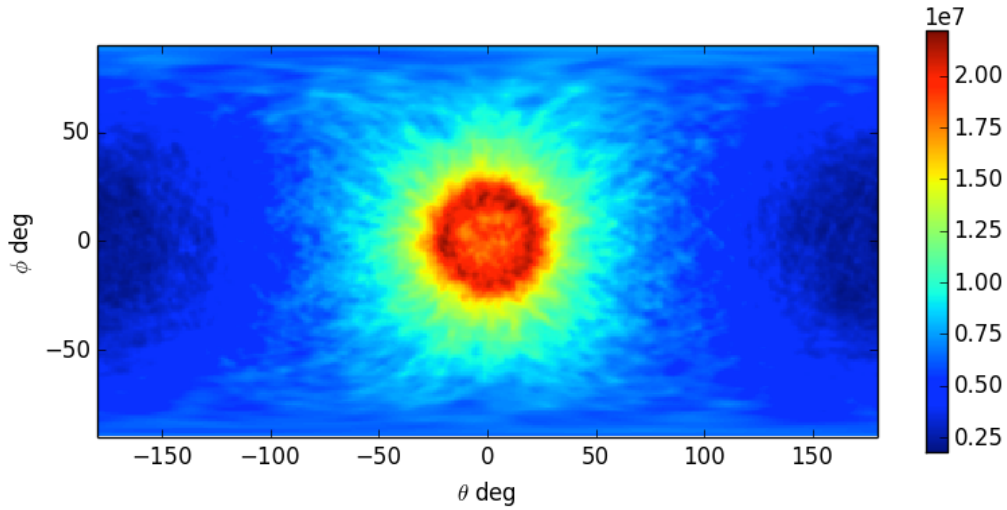

Figure 3.9: A simple back-projection of a ring source measurement from 34,779 events.

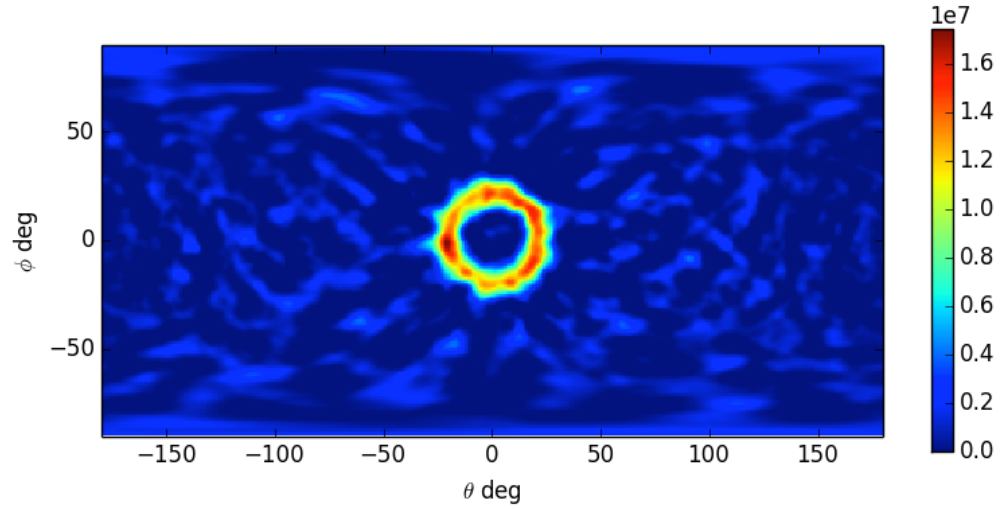

Figure 3.10: A filtered back-projection of a ring source measurement, the same as Figure 3.9 from 34,779 events. The Tikhonov parameter was 0.305.

3.5 Tikhonov Parameter Choice

It should be noted at this point that the Tikhonov values chosen for these images are somewhat arbitrary. They were chosen by the author by an interactive method where changing the parameter changed the image in real-time. More research is needed to quantify the choice of value for this reconstruction method as it is a trade-off between biasing, which degrades resolution, and signal-to-noise. The choice of an optimal parameter can be task dependent. For example, if a point source and distributed source are imaged resulting in the same number of events, a larger value would be needed for the distributed source.

Chapter 4

Gamma-ray Momentum Reconstruction from Compton Electron Trajectories by FBP

This chapter focuses on reconstructing the gamma-ray momentum (direction and energy) incident on an electron tracking detector. The results of this chapter require measuring the electron trajectory, but do not need coincident gamma-rays interactions. This is the only chapter with results from the CCD electron tracking detector. In this imaging modality there are 3 reconstructed dimensions: two of direction and one of energy. This is an increase of one energy dimension compared to Ch. 3, and also a change of modality. This imaging modality assumes a stationary detector with no auxiliary sensors.

Gamma-ray imaging utilizing Compton scattering has traditionally relied on measuring coincident gamma-ray interactions to map directional information of the source distribution. This coincidence requirement makes it an inherently inefficient process. This chapter presents an approach to gamma-ray reconstruction from Compton scattering that requires only a detector capable of tracking individual electrons resulting from a single Compton scattering event, thus removing the coincidence requirement. From the Compton scattered electron momentum distribution, this algorithm analytically computes the incident photon's correlated direction and energy distributions. Because this method determines the distribution of the source energy and direction, it is useful in applications where prior energy and direction information about the source distribution is unknown. While this method was demonstrated with electron tracks in a Si-based CCD, detector it is applicable to any detector that can measure electron direction and energy, or equivalently the electron momentum. In particular, it can significantly increase the sensitivity of gas-based systems that suffer from limited efficiency in coincident detection tasks.

4.1 Introduction

While conventional Compton imaging circumvents some limitations of collimator-based systems, it is inherently limited by (1) the requirement of at least two time-coincident interactions, (2) the knowledge or measurement of the gamma-ray energy, and (3) the reconstruction of the incident angle to only a cone. By using the measured scattering kinematics and by employing (ML-EM) iterative techniques it is possible to reconstruct the gamma-ray momentum, the incident gamma-ray energy and the two incident angles[50]. However, these methods are computationally intensive because they include detailed information about the detector system. No analytical solution for energy-image inversion for gamma-ray tracking Compton imaging has yet been found.

By measuring the initial direction of the Compton-scattered electron, some of these limitations can be avoided or reduced. For example, the azimuthal symmetry of the Compton scattering process that results in the reconstruction of a cone can be broken and the scatter cone can be reduced to an arc [6]. In addition, the electron-track information makes the gamma-ray tracking less error-prone. However, past electron-tracking based Compton imaging concepts and systems have relied on at least two interactions. In the following a concept and associated algorithm is described that enables the analytical and therefore efficient reconstruction of the gamma-ray momentum based only on the measurement of Compton-scatter electron tracks.

4.2 Algorithm Overview

The algorithm differs from previous algorithms in two crucial ways. First, the algorithm uses data from electron-tracking rather than gamma-tracking data (i.e. data from the electron trajectories, rather than from coincident photon interactions) as depicted in event A in Figure 1.2. The analysis uses the direction of the electron motion as the axis for the reconstruction cones. Second, in contrast to other analytical methods, the energy of the incident radiation (E) is no longer assumed known. Instead of assigning each event to a cone, each event is associated with a class of cones sharing the same axis, but with different opening angles depending on the incident energy and deposited energies. Thus, one now determines the incident flux in three dimensions (i.e., the flux depends on both the energy and direction of the radiation). Each event is characterized by the energy deposited in the detector (ϵ) and the direction of the scattered electron motion ($\vec{\omega}$). Therefore, the input data can be described by a three-dimensional distribution of observed electron trajectories. The mathematical inversion problem posed by this system produces the incident flux distribution (in 3D) from the observed distribution of electron trajectories (also in 3D, albeit a different space).

The proposed algorithm offers several advantages. By using only the electron-tracking data the measurement efficiency is greatly improved by removing the requirement for coincident gamma-ray interactions. Consequently, all Compton scattered events in the detector could theoretically be used for imaging. The use of electron tracks also eliminates the need

for gamma-ray sequencing. Furthermore, the algorithm analytically deconvolves the incident energy by a direct method not requiring iteration. Given these improvements this method would be especially useful in applications where the source energy and direction are not known *a priori*.

4.3 Mathematical Formulation

The mathematical formulation of this problem involves the mapping between two distribution functions. First, one defines the incoming gamma-ray flux, $f(\vec{\Omega}, E)$ with gamma direction $\vec{\Omega} \in S^2$, energy E and units of photons per sec keV steradian. Then one defines $g(\vec{\omega}, \epsilon)$,the measured electron track distribution, with direction $\vec{\omega} \in S^2$, deposited electron energy ϵ, and has units electrons detected per sec keV steradian.

The measured data $g(\vec{\omega}, \epsilon)$ is given by incident flux in the following integral equation:

$$g(\vec{\omega}, \epsilon) = \int_{E_{min}(\epsilon)}^{\infty} \mathrm{d}E \iint \mathrm{d}\vec{\Omega} \frac{f(\vec{\Omega}, E)}{\sqrt{\epsilon(\epsilon + 2m_e)}} \delta(\nu(E, \epsilon) - \vec{\omega} \cdot \vec{\Omega}) \tag{4.1}$$

where the function $\nu(E, \epsilon)$ is the cosine of the angle between the incident photon with energy E and the measured electron track with energy deposited ϵ. Relativistic kinematics yield that:

$$\nu(E, \epsilon) = \sqrt{\frac{\epsilon}{\epsilon + 2m_e}} \left(\frac{E + m_e}{E} \right) \tag{4.2}$$

where m_e is the electron rest mass. Eq.4.2 is factorable into separate functions of E and ϵ. The limit to the energy integration in Eq. 4.1 is the minimum gamma-ray energy that could have deposited ϵ energy in the electron track as defined by scattering kinematics.

Next one defines a back-projection integral that converts the measured electron distribution into a distribution of incident flux:

$$b(\vec{\Omega}, E) = \int_{0}^{\epsilon_{max}(E)} \mathrm{d}\epsilon \iint \mathrm{d}\vec{\omega} \frac{g(\vec{\omega}, \epsilon)}{\epsilon + 2m_e} \delta(\nu(E, \epsilon) - \vec{\omega} \cdot \vec{\Omega}) \tag{4.3}$$

where $\epsilon_{max}(E)$ is the maximum energy that can be deposited by a gamma ray with energy E as defined by scattering kinematics.

The surface of all possible incident gamma-ray directions and energies for a single electron track is hyperbolic. However, this surface can be remapped to a plane as depicted in Figure 4.1. This mapping is accomplished by the following transformation:

$$(E, \vec{\Omega}) \rightarrow \vec{u} = \frac{m_e E}{E + m_e} \vec{\Omega} \tag{4.4}$$

with inverse:

$$E = \frac{m_e |\vec{u}|}{m_e - |\vec{u}|}, \vec{\Omega} = \frac{\vec{u}}{|\vec{u}|} \tag{4.5}$$

This combines $E \in R$ and $\vec{\Omega} \in S^2$ into a single vector $\vec{u} \in R^3$ where $|\vec{u}| \in [0, m_e)$. The hyperbolic surface goes to infinity while the remapped plane is contained in a sphere with radius m_e. In other words, this transform maps the incident energy from $[0, \infty)$ to $[0, m_e)$. This space will be referred to as $\vec{u}$-space.

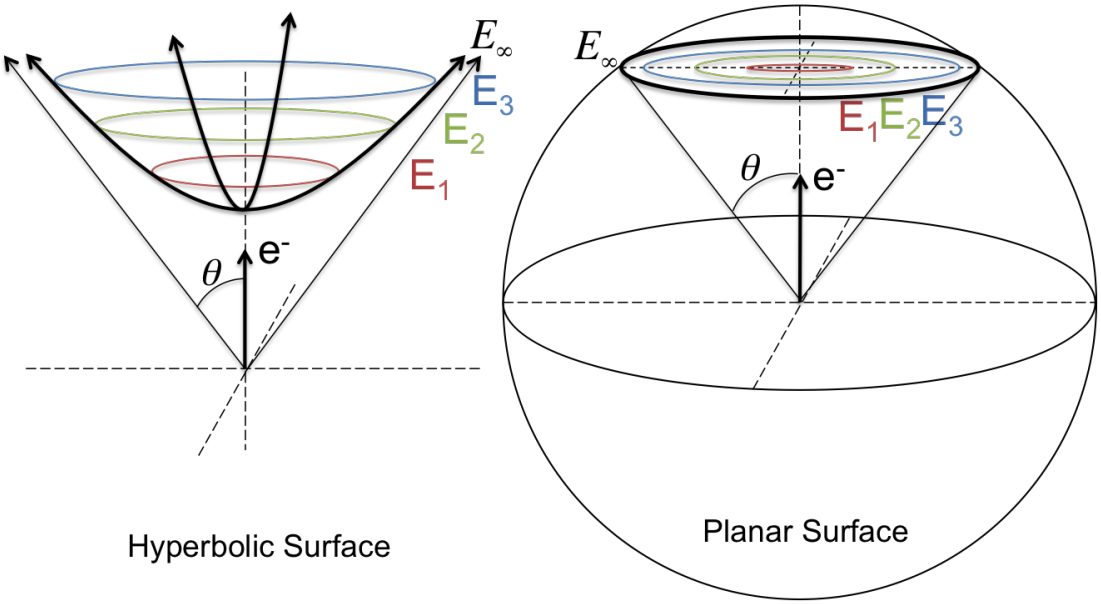

Figure 4.1: The left image shows, in $(\vec{\Omega}, E)$ spherical coordinates, the hyperbolic surface of all possible incident gamma-ray directions and energies for a single electron trajectory. The right figure shows this surface remapped to a plane in $\vec{u}$-space. Three example energies are shown to demonstrate how they map from one surface to the other.

Applying this transform to the source space results in new functions $f_1(\vec{u}) = f(\vec{\Omega}, E)$ and $b_1(\vec{w}) = b(\vec{\Omega}, E)$. Using these transformed functions and grouping terms gives:

$$B(\vec{w}) = \frac{m_e}{|w|} b_1(\vec{w}) \tag{4.6}$$

$$F(\vec{u}) = \frac{m_e}{|\vec{u}|} \frac{f_1(\vec{u})}{(m - |\vec{u}|)^2} \tag{4.7}$$

Substituting Eq. 4.1 into Eq. 4.3 and applying the definitions in Eq. 4.6 and 4.7, one finds the convolution integral:

$$B(\vec{w}) = \iiint \frac{\pi F(\vec{u})}{|\vec{u} - \vec{w}|} \, \mathrm{d}\vec{w} \tag{4.8}$$

The Fourier transform of this equation yields:

$$\tilde{F}(\vec{k}) = |\vec{k}|^2 \tilde{B}(\vec{k}) \tag{4.9}$$

where $\tilde{F}(\vec{k})$ and $\tilde{B}(\vec{k})$ are the 3D Fourier transforms of $F(\vec{u})$ and $B(\vec{\omega})$ respectively. The resulting $|\vec{k}|^2$ filter in 3D will amplify high frequencies, which can be dampened using Tikhonov regularization resulting in:

$$\tilde{F}(\vec{k}) = \frac{|\vec{k}|^2 \tilde{B}(\vec{k})}{1 + \lambda^4 |\vec{k}|^4} \tag{4.10}$$

Here, λ has units of keV and is the Tikhonov parameter that can be adjusted as a trade-off between noise and resolution. Higher values of λ reduce high-frequency noise but at a cost of image resolution.

The steps for computing this algorithm are as follows:

1. Individual electrons are measured from Compton scattered gamma-rays. The ensemble of these electrons create the distribution $g(\vec{\omega}, \epsilon)$.
2. Compute the back-projection on a 3-D rectilinear grid in the energy transform space, corresponding to Eq. 4.3.
3. Compute the 3-D FFT of the back-projection.
4. Filter in Fourier space based on Eq. 4.10.
5. Compute the inverse FFT of the filtered result.
6. Interpolate the filtered result from the energy transform $\vec{u}$-space to a grid on $(\vec{\Omega}, E)$ to recover the $f(\vec{\Omega}, E)$ distribution.

The range of the back-projection grid is from $[-m_e, m_e]$ in each dimension to account for the energy being transformed from $[0, \infty)$ to $[0, m_e)$. The uniform grid in $\vec{u}$-space leads to larger energy bins at higher energies because of the hyperbolic nature of the $\vec{u}$-space transform.

4.4 Experimental Demonstration Cs-137

The proposed algorithm was demonstrated with electron trajectories measured with a scientific Si-based charge-coupled device (CCD) [43]. Measurements from an uncollimated Cs-137 source was acquired to demonstrate this algorithm for a 662 keV source. The results shown here were computed with 256 pixels in each $\vec{u}$-space dimension.

The Cs-137 source was positioned at a 22 degree angle off of the detector plane. The data includes 36k electron tracks with energies greater than 200 keV. The angular resolution of the electron tracks in this CCD detector degrades significantly below 200 keV.

Figure 4.3 shows the reconstructed source in the 3-D energy-image space. This 3-D image can be difficult to interpret so slices are taken to show images at specific energies. Figure 4.4 shows the directional image at 662 keV. The source has an angular resolution of 30 by 21 deg FWHM as determined by Gaussian fit, which is consistent with the angular

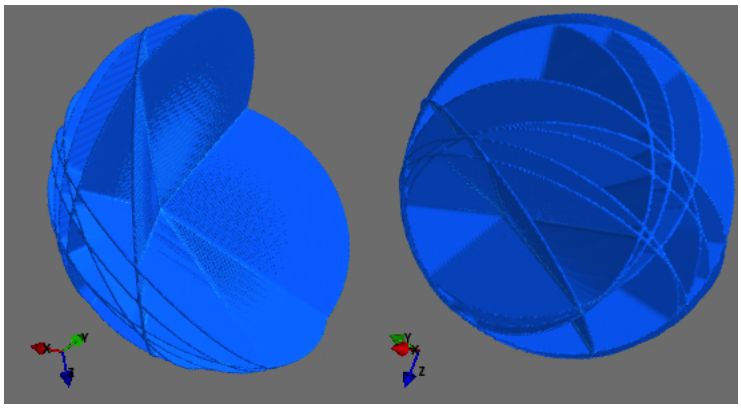

Figure 4.2: Shown here is an example of back-projection in the 3D energy transform space for ten simulated events. The two images show two different viewpoints of the same back-projection. The intersection of the planes in this 3D space determines the source direction and energy.

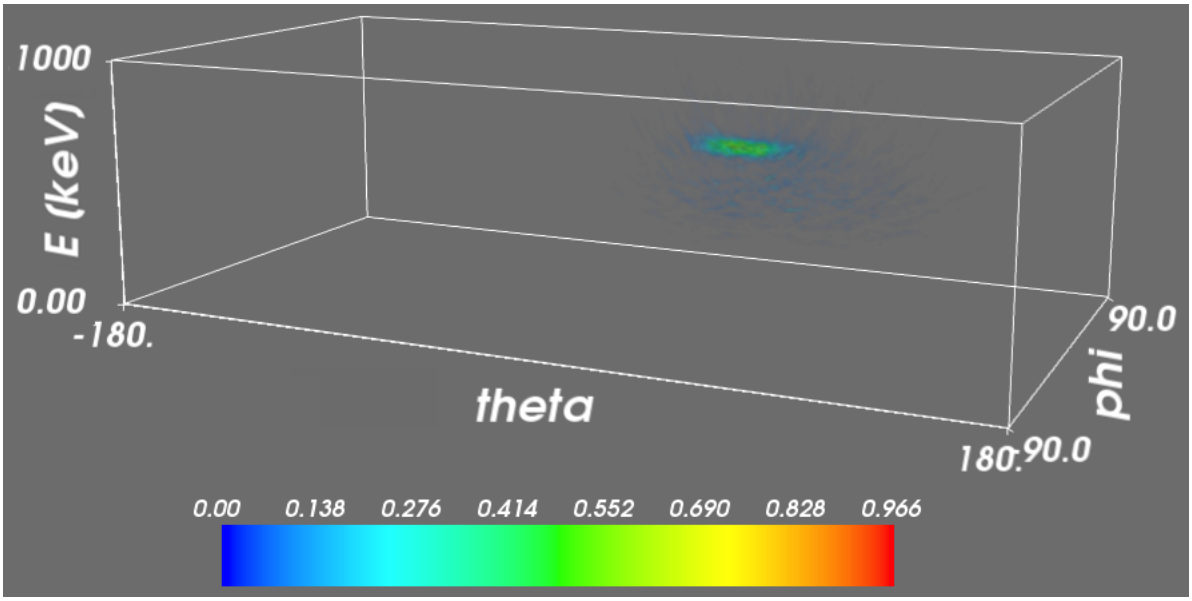

Figure 4.3: This image shows a 3-D representation of the energy image from a Cs-137 source measurement.

resolution of the detector. A detector with finer angular resolution would produce a sharper image, the resolution is not inherently limited by this method. Directional spectra can also be observed as seen in Figure 4.5. This spectra shows a reconstructed source energy of 647.6 keV with a resolution of 36 keV FWHM as determined by a Gaussian fit of the peak. The reconstructed energy is lower than the expected 662 keV energy and the exactly cause of this is not currently known. This could have been caused by electron tracks escaping

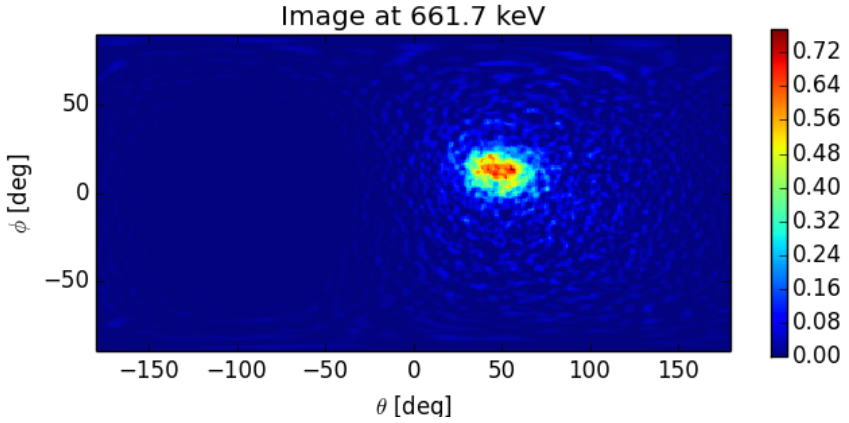

Figure 4.4: An image at the source energy of 662 keV with a resolution of 30 by 21 deg FWHM.

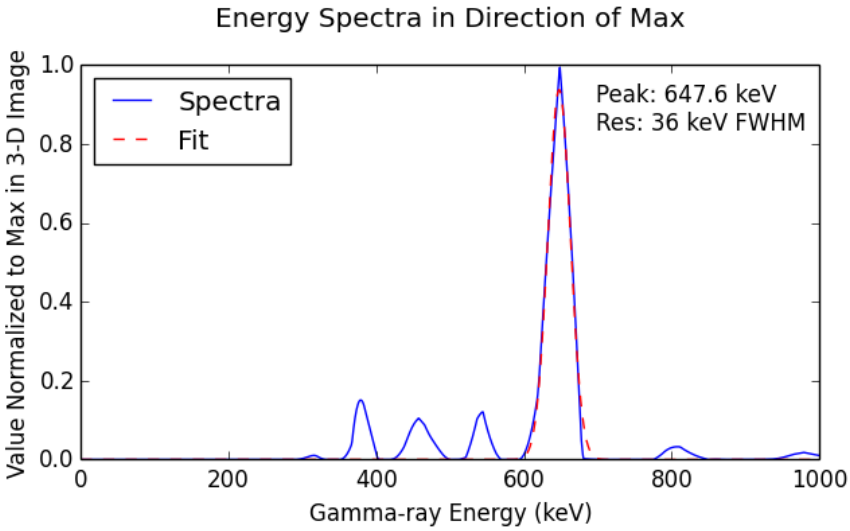

Figure 4.5: The spectra through the source maximum value. The 662 keV peak is observed. The peaks above and below 662 keV are caused by noise. They can be removed by increasing the Tikhonov value, but at the cost of broadened resolution.

the CCD detection volume and not depositing their full energy. No assumption about the source energy were made in this reconstruction. Figure 4.6 shows the energy spectrum of the electron tracks used in the image, showing that no photo-peak was directly observed. In this image a Tikhonov regularization value of 15.8 keV was used to compensate for the noise. This contributes to the large resolution of the 662 keV source line. A lower Tikhonov value could be used and better energy resolution would be achieved at the expense of increasing image and spectral noise.

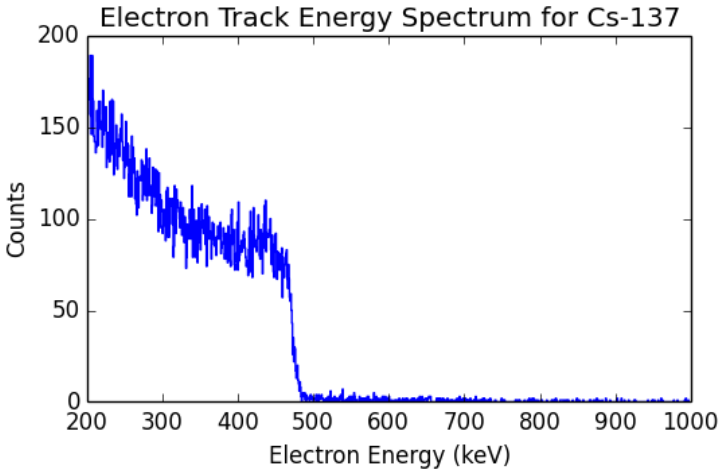

Figure 4.6: The measured electron track spectrum is shown. One notes that the 662 keV photo-peak is not observed. Electron energies less than 200 keV are excluded from the reconstruction. Knowledge of the incident energy must be deconvolved from the electron directional information.

4.5 Ba-133 Measurement

Measurements were taken with a Ba-133 to test lower energy gamma-ray sources. Ba-133 also provides an additional challenge because it emits multiple gamma rays, each with lower energy than the Cs-137 source. At these lower energies the CCD has worse angular resolution because lower energy electrons traverse fewer pixels. The different energies could be imaged however at this stage reconstructing the different energies required changing the energy threshold of the electron tracks used to generate the image.

The gamma rays of interest from Ba-133 for this measurement are 356 keV and 384 keV. To accommodate these energies, the energy cutoff was lowered to 150 keV. This degrades angular resolution but is needed for the lower 356 keV source energy of Ba-133. As with the Cs-137 source, a full energy-image was reconstructed from the Ba-133 data. This reconstruction is then visualized as spectra in a particular direction or directional maps at a particular energy. The 3-D reconstruction is not shown as it is visually similar to the Cs-137 result. The reconstructed energy spectrum through the source max is shown in Figure 4.7. This reconstructed spectra reveals the 356 keV source energy, but not the 384 keV source energy. This shows the reconstructed 356 keV peak with an energy spread of 26 keV FWHM. The reason the lines are not simultaneously observed is due to the poor angular resolution of the CCD and the lower branching ratio of the 384 keV line. This requires a high Tikhonov value to overcome the noise, which then also blurs the image in energy. The directional image with a 150 keV cutoff from measuring Ba-133 is shown in Figure 4.8. The angular resolution of this source is worse than that of Cs-137 because the lower electron track energies have

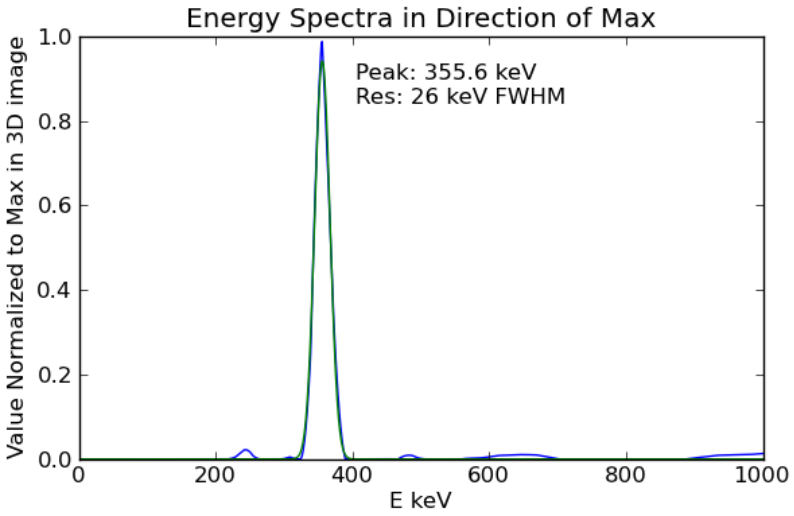

Figure 4.7: This shows the energy spectra in the direction of the maximum image intensity. For this reconstruction, a 150 keV energy cutoff was used.

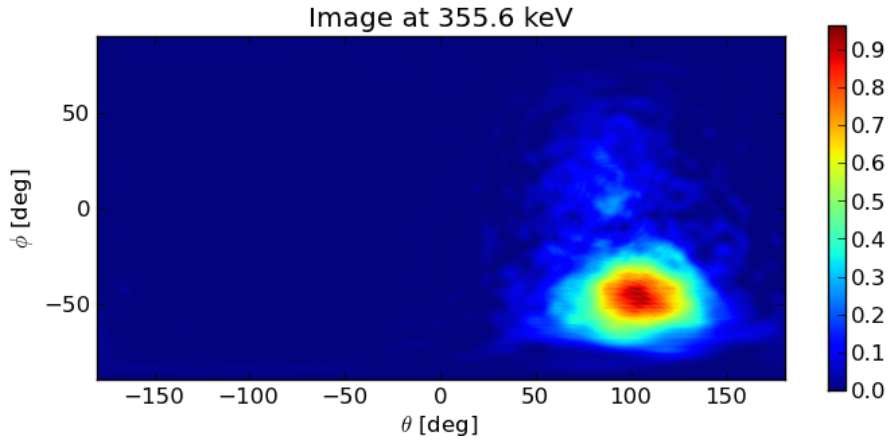

Figure 4.8: This shows a Ba-133 directional image from a 150 keV cutoff energy.

broader angular resolution.

The 384 kev line can be observed by increasing the energy cutoff up to 207 keV, which is near the Compton edge of the 356 keV line. The different electron track energy spectra used for imaging each line are plotted in Figure 4.9. All events above 150 keV were used for the image that reconstructed the 356 keV source. The spectra used to reconstruct the 384 keV line is the portion above 207 keV. The image from the 384 keV source is shown in Figure 4.10 and the corresponding spectra is shown in figure 4.11. This 384 keV line is observed with a resolution of 26 keV. It is interesting to note the small portion of events that actually contribute to this source from the electron spectrum in the range 207 to the Compton edge

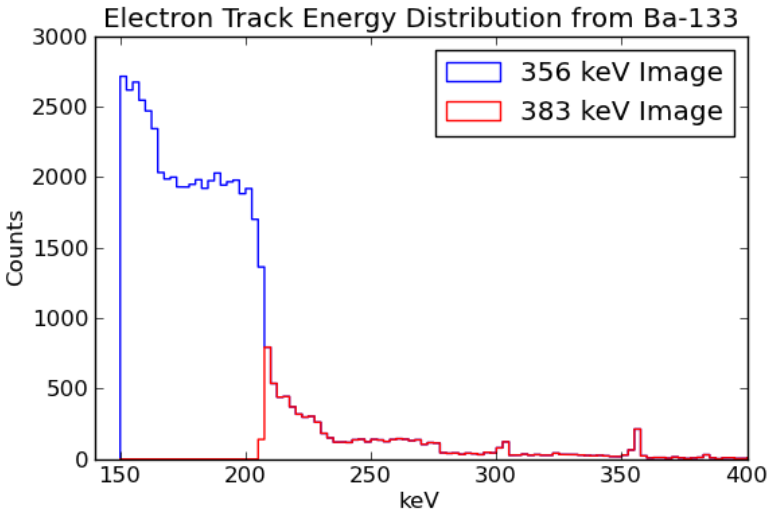

Figure 4.9: This shows the measured electron spectra in the CCD for the Ba-133 source. All Events above 150 keV were used for the 356 keV image and all events above 207 keV were used for the 384 keV image.

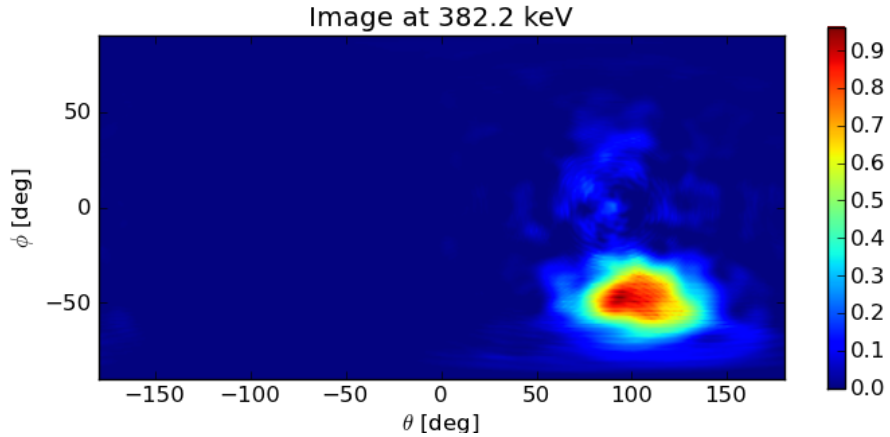

Figure 4.10: This shows the reconstructed directional distribution from a Ba-133 point source at 384 keV.

at 230 keV. It is also interesting to note that the reconstructed energies were closer to the actual source energies for Ba-133 than compared to the Cs-137 measurement.

4.6 Co-60 Measurement

A Co-60 measurement was taken to test the reconstruction of higher energy gamma rays. The higher energy gamma rays generate higher energy electron tracks, which results in longer

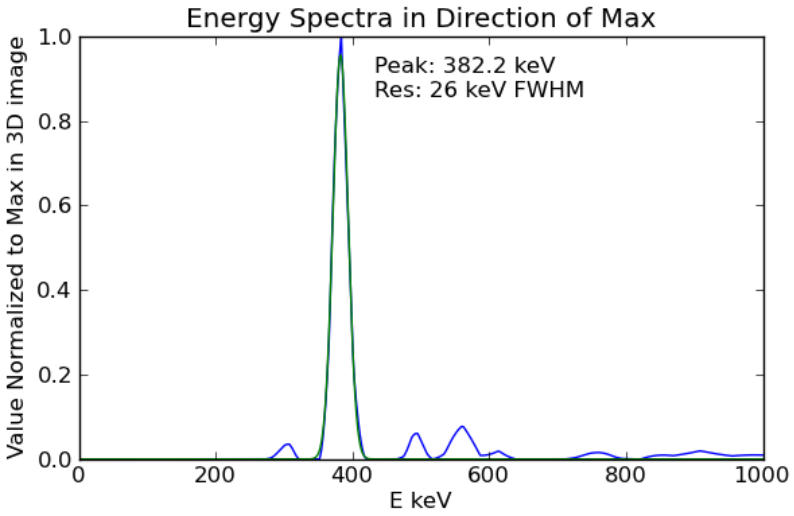

Figure 4.11: This plot shows the reconstructed spectra from a Ba-133 measurement with an electron track energy cutoff of 207 keV.

track lengths that are more likely to escape the CCD and not deposit their full energy. As a result, higher energy cutoffs are needed to reconstruct the source energies. Many events with measured energies between 200 keV to 750 keV are from electrons that deposited a fraction of their initially higher kinematic energy. This lead to the hypothesis that as the energy cutoff is increased, the fraction of events that deposit their full energy also increases. This is supported by the fact that higher energy cutoffs made reconstructing the higher source energies of Co-60 possible. A cutoff of 750 keV was sufficient for reconstruction of the 1173 keV gamma-ray energy. The threshold can then be raised to observe the 1332 keV line. The reason these lines are not observed simultaneously is more complicated than the Ba-133 case and is not yet fully understood. Possible factors include: poor angular resolution, larger energy bins at this source energy from the reconstruction energy transform, different detector efficiencies for the two energies, or high loss of events from 1332 keV line due to its higher energy. The resulting images from the Co-60 are not shown as they are similar to the Ba-133 and Cs-133 images, however the reconstruction values are tabulated in Table 4.1. This table also compares the reconstruction results from all the sources described in this chapter, including the different cutoff values and resolution values.

4.7 Conclusions

A full gamma-ray momentum distribution reconstruction was developed and demonstrated experimentally utilizing only electron track measurements from Cs-137, Ba-133 and Co-60. The Ba-133 and Co-60 measurements demonstrate some limits of the CCD system. Additional work should be done to reconstruct multiple energies simultaneously. The algorithm

Source	Energy	ϵ cut	Reconstruction		Resolution FWHM		
			# Tracks	Engergy	Eng (keV)	Theta	Phi
Ba-133	356	150	56k	355.6	26.3	37.9	58.8
	384	207	8k	382.2	26.1	21.5	53.7
Cs-137	662	200	36k	647.6	35.8	21.5	30.4
Co-60	1173	750	3630	1162.4	87.6	33.6	53.3
	1332	950	715	1312.8	27.6	27.6	53.1

Table 4.1: This table lists the reconstruction results from all the sources discussed in this chapter. All energies are in keV and angles in degrees. ϵ cut refers to the low energy cutoff below which electron track events are removed from the reconstruction. The measurement time for each source varied so the number of events used is not an indication of efficiency for each energy. The number of tracks listed is after the energy cut was applied.

reconstructed the sources full energy using the electron track direction and energy without directly measuring the source energy. This algorithm offers two main improvements for gamma-ray imaging. The first is the increase in imaging efficiency by only requiring electron track data and thus removing the requirement of coincidence measurement. The second advantage is analytically inverting the gamma-ray energy by direct method. This algorithm was demonstrated with measured electron tracks in a Si CCD detector with a source energy of 662 keV. The quality of the image is limited by several factors associated with the CCD such as poor angular resolution, electrons escaping the detector volume and the algorithms used to determine the electron trajectory[32]. This method would work for other systems that measure Compton electron trajectories such as TPC gas systems[38], and the quality of images from such devices needs to be investigated. Thus these results are intended as a demonstration of this method and not as an indication of its limits.

Chapter 5

3-D Compton Imaging with Visual Data Fusion

In this chapter 3-D spatial reconstruction is demonstrated with the CCI system, which was described in section 2.2, thus we are returning back to gamma-ray tracking based Compton imaging. This will focus on far-field 3-D mapping as opposed to near-field 3-D imaging which is common in medical imaging research [28]. To gain a 3rd dimension of spatial information, the Compton camera is moved throughout the mapping area. Position tracking of the system is achieved with a Microsoft Kinect as an auxiliary sensor. The reconstruction method used in this chapter is a slightly modified ML-EM algorithm to accommodate the visual data input. The ML-EM algorithm is simplified to ensure near real-time operation. There is no convenient FBP method for this imaging domain, especially for the low count rates used to demonstrate this method.

5.1 Overview

The goal of this chapter is the demonstration of the ability to locate sources in complex real-world environments. Such environments could include outdoor urban environments or nuclear processing facilities for safeguards applications. The focus of this work is a description of the reconstruction method used to recover the 3-D distribution of gamma-ray emitting sources. A more thorough description of the system setup and processing pipeline, including the visual data processing, are the focus of Ross Barnowski's PhD work and are the subject of a publication in progress[2]. For this demonstration, a cluttered lab environment is used with a Cs-137 source.

To achieve 3-D imaging, a Microsoft Kinect is used as an auxiliary sensor. The Kinect serves two purposes:

- position the Compton camera in the scene

- build a visual model of the scene which is incorporated into the gamma-ray reconstruction.

This is achieved by a Simultaneous Localization and Mapping (SLAM) algorithm [10]. The code for this algorithm is freely available within the framework of the Robot Operating System and thus we were able to use it for our system. To build the model, successive frames from the Kinnect are merged together in 3D so that the visual model expands as the detector cart moves through the scene and more visual data is collected. The output of this algorithm is a visual point-cloud. In this chapter the term "point-cloud" refers to the 3-D visual data in the form of a set of points. Each point has six values: a 3-D position coordinate and 3 color values representing RGB.

The visual data can help overcome two main issues with 3-D gamma-ray mapping. One is the low count rate expected for Compton coincidence events over a short period of time. For example, a path about 1.5 m from a 50 μCi Cs-137 source produces on the order of 100 full energy events per minute in the CCI2 detectors. Another issue is in the sampling path of the cart as it moves arbitrarily through a scene. If the cart is going to be pushed through an environment on an arbitrary path it is unlikely that orthogonal projections needed to fully reconstruct the source space will be acquired. This leads to an ill-posed reconstruction problem, which will inaccurately reconstruct the source distribution. The visual data adds an additional constraint to the reconstruction, which can help regularize the solution and overcome these sampling limitations.

5.2 ML-EM Overview

This chapter utilizes the ML-EM reconstruction algorithm, which will now be generally described. Independent of image reconstruction, Maximum Likelihood-Expectation Maximization is a method for maximizing a likelihood function that describes a distribution when another distribution is observed. ML refers to maximizing a likelihood function that relates the data and the computed image, which in the case of gamma-ray imaging obey Poisson statistics. In general, EM refers to the mathematical method of maximizing a likelihood function when there is a latent, unobserved variable. The original solution to ML-EM for emission tomography utilized this approach [37]. In the case of gamma-ray imaging, the latent variable is a variable that describes exactly which image element (voxel, pixel, etc. depending on the dimensionality) a single measured data event originated. For Compton imaging, the Compton cone dictates a set of pixels from which the source could have originated. This latent variable corresponds to exact knowledge of which element the gamma-ray originated. Later solutions found algebraic approaches to arrive at the same answer[7].

This method was later applied to list mode data [3] and then to Compton list mode data[48]. The equations used here are as follows:

$$\lambda_i^{(n+1)} = \frac{\lambda_i^{(n)}}{s_i} \sum_{j \bigcap l} \frac{a_{ij}}{\sum_{l \bigcap j} a_{lj} \lambda_l^{(n)}} \tag{5.1}$$

where:

- n is the iteration number
- i is the image element index
- j is the data index
- $\lambda_i^{(n)}$ is the image value in voxel i at iteration n
- a_{ij} is the system matrix value
- s_i is the sensitivity for image element i

In this case, the image elements are voxels. Because this is list mode reconstruction, the sensitivities cannot be computed directly from a_{ij} and thus in practice they must be computed by some other means. However, to ensure as close to real-time computation as possible, uniform sensitivities are used. In general this assumption results in imaging artifacts for complicated source distributions, but it works sufficiently well for the point sources of this imaging task.

5.3 ML-EM with Visual Data

The gamma-ray reconstruction can be computed with or without the aid of the visual information. To perform the reconstruction with the visual reconstruction, a constrained ML-EM method is used. The constraint comes from the 3-D point cloud data from the Kinect. Using visual 3-D point cloud data, the space is voxelized around the point clouds. An occupancy grid is created from the visual point cloud based on the assumption that gamma-ray emitting objects will only be contained on or inside visual objects. When the ML-EM reconstruction is constrained by the visual data, it is only computed in the voxels that are occupied by the visual grid. This strategy not only improves the reconstruction results, this also improves the computation time because a limited number of voxels are used for the reconstruction. The reconstruction is performed in near real-time, so that both the visual space and the distribution of gamma-ray emitters are reconstructed as the data is collected.

Alternatively, the reconstruction can also be computed without constraining the solution with the visual point cloud data. This is done by voxelizing the entire space surrounding the cart path to a fixed distance. The extent of the grid is determined from the length of the cart path because the depth sensitivity is limited by the cart path length. This can be advantageous because the Compton camera has a 4π field of view whereas the Kinect has a much more limited FOV. Thus there could be cases where the Compton camera localizes a source that was not in the view of the visual camera.

5.4 Computational Structure

The computational thread structure is shown in Figure 5.1. There are two main components

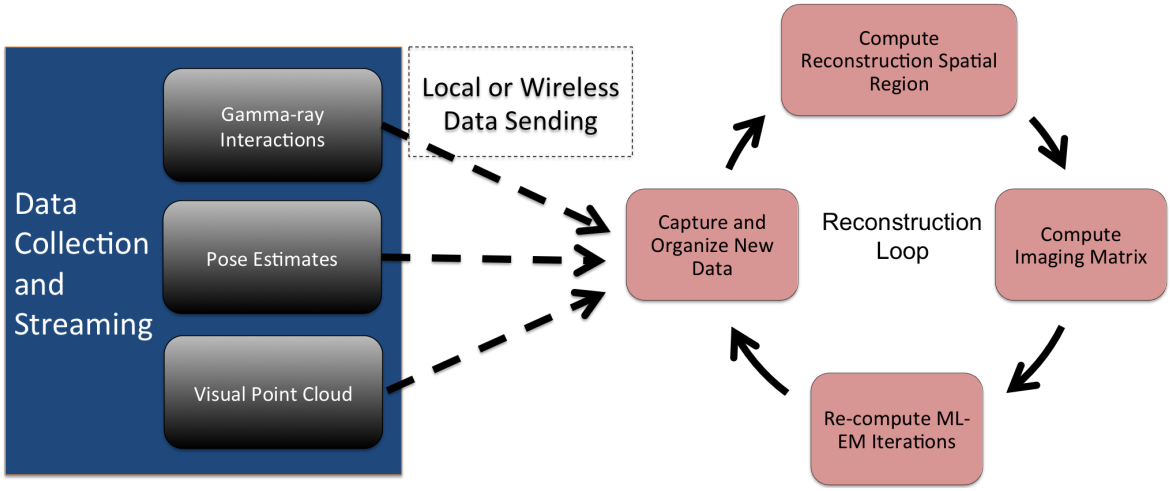

Figure 5.1: This diagram shows the structure of the software used to acquire and reconstruct the volumetric data. There are two main components: acquisition and reconstruction.

to the reconstruction structure: acquiring the data and reconstructing the imaging space. In practice these can both be on one acquisition computer or on separate computers. Separate computers is advantageous because it allows for data analysis to happen at a stationary location while the detector is being moved through the scene. The acquisition part includes the visual processing, both of which are the focus of Ross Barnowski's work.

Here we will focus on the reconstruction portion of the software. The reconstruction loop consists of four main parts:

1. Capture and organize data
2. Determine the area where the reconstruction will be computed
3. Recompute the imaging matrix
4. Compute ML-EM reconstruction iterations

Step 1 requires syncing the data based on time stamps. Also data can be sent at irregular intervals and thus a fixed collection time is used before a new reconstruction is performed. This is also needed to control when the reconstruction is recomputed. There should be sufficient new data to allow for a new reconstruction to proceded. In Step 2 the limits of the volumetric reconstruction grid are determined based on the pose estimates, the point-cloud data, or both. The reconstruction space changes as the point-cloud expands and more pose estimates are collected. Step 3 computes the imaging matrix for this newly computed space.

The voxels where the image is reconstructed can be limited by the visual point cloud data at this step. The final step is to perform the ML-EM iterations. This step is relatively fast because the imaging matrix is precomputed in step 3. Also, the iteration Eq. 5.1 can be written as matrix operations so that fast matrix multiplication and numerical array operations in Numpy are utilized.

The version of this software described here is not directly scalable to large mapping areas. To accommodate this, future versions will use data caching by only computing the image near where new data has been recently collected. Then this locally updated reconstruction can be merged to a larger global reconstruction. The global reconstruction would also need an optimized storage method, likely based on octrees.

5.5 Measured Results

As a demonstration measurement, a 50 μCi Cs-137 source was placed in a cluttered lab environment. The CCI2 cart system was pushed through this lab environment. Figure 5.2 shows the reconstruction of a Cs-137 source in 3D without using the visual data to constrain the ML-EM. This plot shows several pieces of data related to the measurement including:

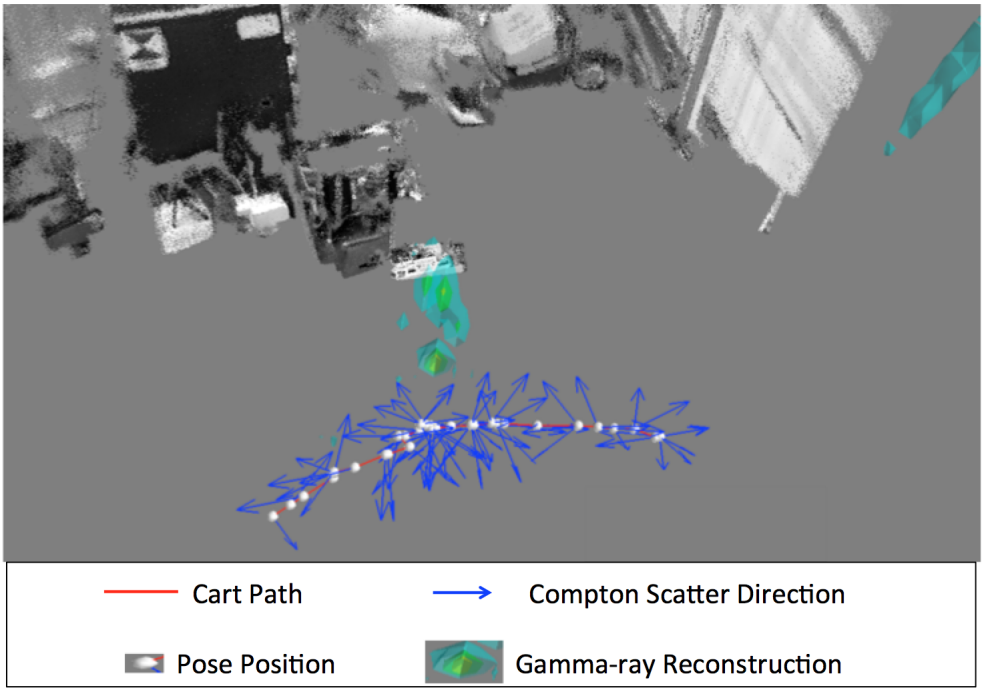

Figure 5.2: 3-D ML-EM reconstruction without using the visual point-cloud data. The entire space around the detector path was voxelixed and reconstructed. The source location is blurred and there are image artifacts. The measurement time was 34 seconds which produced 74 events for imaging at 662 keV.

the visual point-cloud reconstructed by the SLAM algorithm, the Compton camera pose estimates, individual Compton scatter events and the reconstructed source distribution. The SLAM algorithms produces a visual point-cloud and a rotation and translation for each frame, which together create the pose estimate. This rotation and translation is the position of the Kinect in the scene. An additional rotation and translation is then used to map the Compton camera in the scene from that data. The reconstruction shows the source being reconstructed to the wrong location, likely due to the inadequate sampling of the cart path. This also shows some reconstruction artifacts in air where no source was located.

Figure 5.3 shows the result when the visual data is used to constrain the reconstruction voxels. The result from the constrained reconstruction is improved and correctly locates the

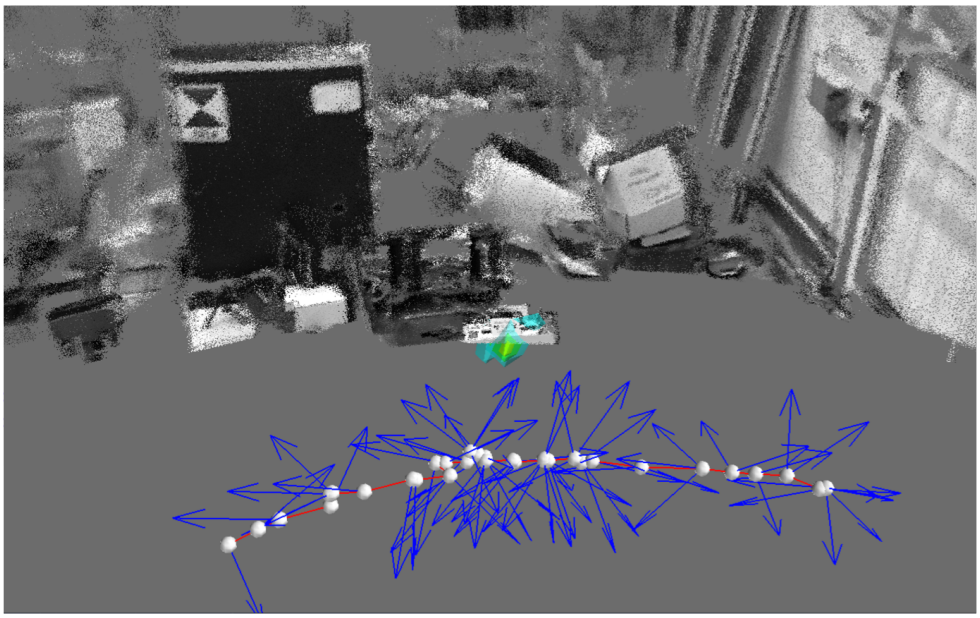

Figure 5.3: This shows the 3-D constrained by the visual point cloud.

source in 3-D. The imaging artifacts when the point-cloud is not used are removed.

While the results shown here are for one example measurement, this method appeared to be robust across a variety of measurements similar to the one shown here. Further work is needed to quantify the effectiveness of this method to locating sources by this data fusion approach.

Chapter 6

Imaging with HEMI

This chapter focuses on Compton imaging results with the HEMI system. The major advantage of this system is its size and weight. The imaging hardware and electronics weigh less than 10 lb. and are highly portable. However, this small size does come with some imaging performance downsides. These issues will be discussed, as well as proposed solutions. Additionally, HEMI was used in field measurements taken in Fukushima, Japan as a demonstration of the ability to map the cesium contamination. To accomplish this, HEMI was packaged with auxiliary sensors and mounted to a remote control RMAX helicopter system. The Fukushima imaging environment proved challenging and the analysis of those issues will be discussed here. A combination of data analysis, lab measurements and simple simulations were used to enhance the understanding of what was limiting the image performance in such an environment. The imaging results shown in this chapter are at the 662 keV line of Cs-137.

6.1 Measurement Challenges

The goal of mapping the contamination in Fukushima, Japan is the localization of hot spots to aid in the decontamination and monitoring process, which could lead to people being able to return to currently evacuated regions. Mapping cesium, specifically Cs-137, contamination in Fukushima is technically challenging for several reasons. The imaging scenario consists of a relatively constant background cesium level, with concentrated hotspots, likely due to water flow and rain.

Several measurement campaigns were performed in Namie, an evacuated town in Fukushima prefecture. The chosen location was a riverbed, where hotspot concentrations have developed due to water flows in this area. These measurements were performed in collaboration with the Japanese Atomic Energy Agency (JAEA) and the University of Tokyo through Prof. Hiroyuki Takahashi. In these measurements HEMI was packaged with several auxiliary sensors and mounted to a remote controlled RMAX helicopter. The auxiliary sensors included GPS with IMU, visual camera and onboard computer. The riverbed where the

measurements where taken are depicted in Figure 6.1. This area is of interest because it

Figure 6.1: This picture shows the area where HEMI was flown on a helicopter in May 2014. The cone indicates a known hotspot several meters out in the grass. The tress in this scene make the imaging environment challenging because their contamination level is not known. The river is behind the trees.

contains concentrated hotspots due to the river flow. The orange cone in the picture indicates a known hot spot. The trees in this scene make the imaging task challenging for several reasons. The contamination level in the trees is not known. Also, HEMI will be more sensitive to the trees as they are closer to the detector when the helicopter is flying over them. These measurements proved extremely challenging to reconstruct the ground source distribution. These challenges lead to the systems imaging analysis described in this chapter. The accurate reconstruction of the scene is the subject of continuing research and will need to build off the work described here.

Compton imaging with HEMI in the Fukushima contamination environment proved challenging for several reasons. The challenges that are specific to the HEMI system include:

- False coincidences
- Sampling issues
- Mis-sequenced events
- Down scatter events

False coincidences refers to events randomly occurring in the Compton coincidence timing window and thus creating a random background of events. Sampling issues are related to the data collected from HEMI, including scattering direction and distribution, as was discussed in section 2.5. These sampling issues relate to data sufficiency conditions, which are currently not clear for Compton imaging. Mis-sequenced events are events for which the interactions are incorrectly sequenced. Down scatter events come from gamma rays that Compton scatter and deposit part of their energy where this partial energy deposition correlates to another imaging energy of interest. Specifically for cesium contamination, one example is of the 796 keV line from Cs-134 down-scattering to 662 keV. Each of these issues are discussed further in the following sections.

6.2 False Coincidences

Random coincidences are a result of the relatively high count rate of the Fukushima environment combined with the 1 cm^3 cube size of HEMI. The 1 cm size of the detector cubes broadens the time resolution due to the drift across the length of the detector crystal. This broadened time resolution means that as the event rate increases, so does the false coincidence rate. These false coincidences then get tagged as Compton coincidence events, which can create noise in the image.

A similar issue of false coincidences can occur in PET imaging systems. To account for this issue, a time delayed signal is used to create a false coincidence signal. This is then subtracted from the true coincidence signal at the data (sinogram) level. This subtraction changes the Poisson statistics and requires modified reconstruction algorithms [11]. This compensation approach is possible with PET when the data is processed in bin mode. However, this technique is not directly applicable to list mode data and thus not easily applied to Compton imaging. A variation on this technique can be used to analyze the effect of random coincidences on the image, and to create an image generated from the random events. This type of analysis is applicable to any Compton imaging scenario where high count rates are expected, such as proton beam depth verification from prompt gamma rays.

To generate a false coincidence signal for Compton data, several steps are needed. First, the individual interactions for the whole system are sorted by time. Then a small time offset that is greater than the coincidence window is added to every other event. This time delay breaks the time coincidence of the true Compton events. However, this will overestimate the false coincidence rate due to the fact that the true coincidences are also mixed into the signal. Because the offset breaks the true coincidence events, this creates an alternate list

mode data set that represents the false coincidence signal. This delayed time data is then resorted by time as it was unsorted due to the offset of half the events. A time difference spectrum is then used to observe the magnitude of the true coincidence and false coincidence. The false coincidence time spectra can be subtracted from the full signal to estimate the true event rate. Also, any metric that can be observed for the unprocessed signal can be analyzed for the delayed signal, for instance the coincidence event energy spectra. Finally, a signal-to-noise ratio (SNR) can be computed as a comparison between the unprocessed signal and the delayed signal.

Measurements were taken to demonstrate this effect. First, a low count rate Cs-137 measurement was used as a baseline. This data is from the same measurement that was used in section 2.5 to show HEMI's data sampling. From that data, a time coincidence histogram is shown in Figure 6.2 on the left as the blue line. This plot shows a true coincidence peak

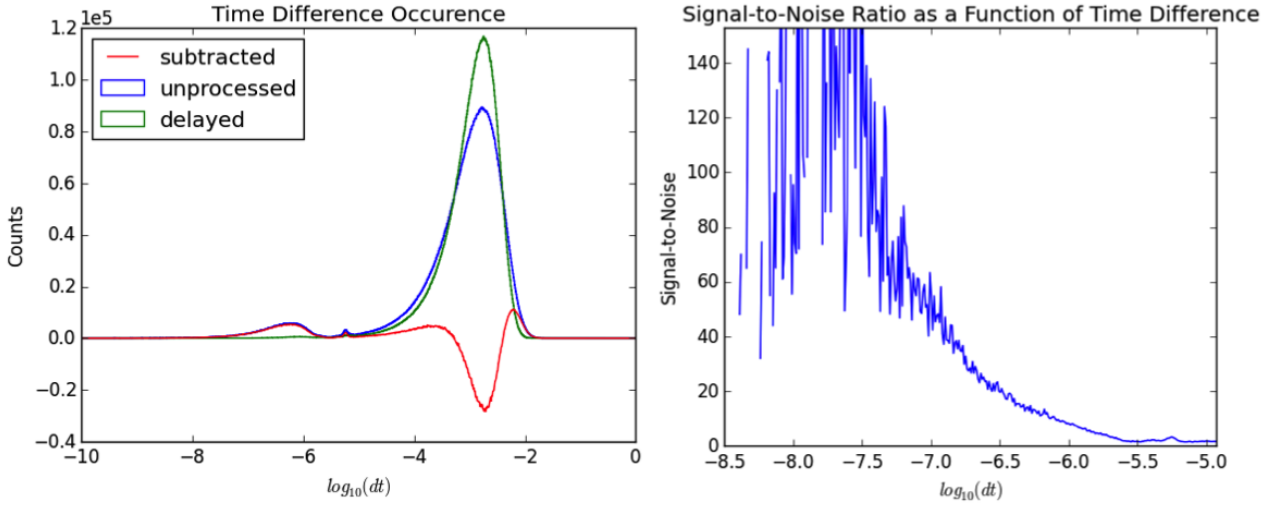

Figure 6.2: On the left, time difference histograms are shown for an unprocessed and a delayed signal. The plot on the right shows a signal-to-noise ratio (SNR) plot as a function of time difference. The SNR is computed by the ratio of the unprocessed signal to the delayed signal. The noise at lower values of the SNR plot is due to the smaller number of events with those time difference values.

near 1 μs (-6 on the plot due to the log scale) and a large false coincidence peak at a longer time scale. It also shows an anomaly peak in the middle from electronic cross-talk, which has been previously documented[13].

To estimate the false coincidence rate, a delayed signal was created with a delay time of 0.1 sec. The time spectra from this delayed signal is also shown in Figure 6.2 on the left as the green line. The delayed time spectra is then subtracted from the unprocessed data to estimate the true coincidence rate in the coincidence window. In the random coincidence region above 1 μs, the subtracted spectra is negative. This is because the delayed signal is an overestimate of the false coincidences as it also contains the true coincidences. From this

data, a signal-to-noise ratio (SNR) can be computed as a ratio of the delayed time spectra to the unprocessed time spectra. This plot is shown in Figure 6.2 on the right. However, these time difference plots do not tell the full SRN story for imaging because energy cuts are also applied before computing the image. Thus an energy spectrum can be compared for delayed coincidence and the unprocessed coincidence events. This energy spectrum comparison is shown in Figure 6.3 on the left. This plot shows the coincidence energy spectra from the

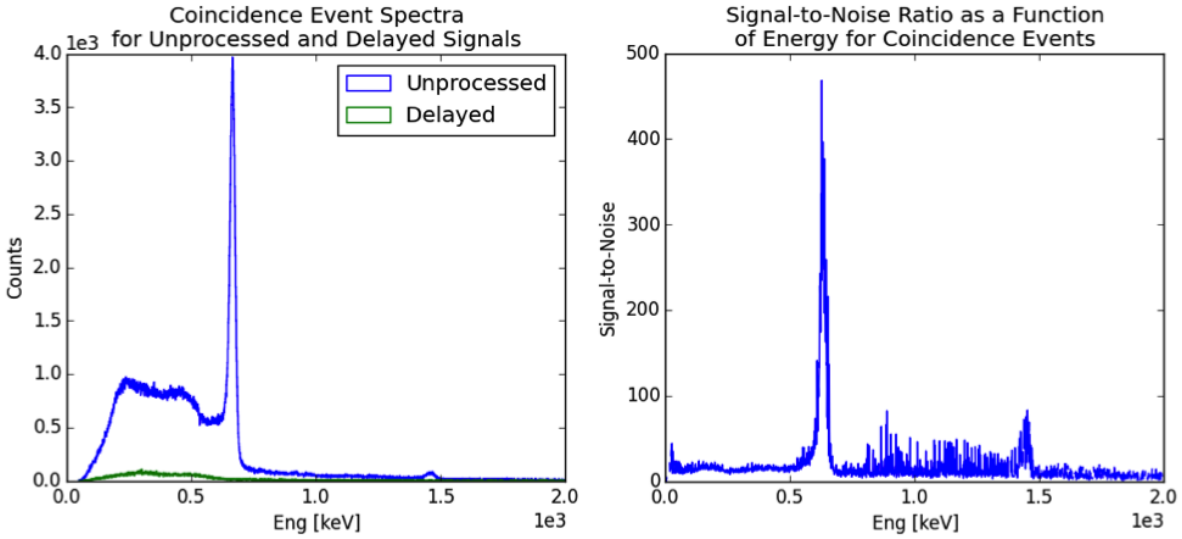

Figure 6.3: The left plot shows the coincidence spectrum for the unprocessed and delayed signals. The right plot shows the SNR as a function of energy as computed by the ratio of the unprocessed coincidence spectra to the delayed spectra. The peak in SNR occurs at the 662 keV peak. There is also an SNR peak at 1461 keV that comes from the K-40 background in the lab.

unprocessed signal and from the delayed signal. The delayed spectra does not show the 662 keV peak. From these two spectra, a SNR can be computed as a function of total event energy. This is shown in Figure 6.3 at the right. There is a peak in SNR at 662 keV from the Cs-137 with a value of 468. Also note that this SNR value is higher than that observed on the time difference plot, which is reasonable because the time difference SNR is for all energies. Another property to note about this SNR plot is that in the Compton shelf of 662 keV, which goes up to 477 keV, the SNR is significantly worse. This means that using these events for energy-image deconvolution could reduce the SNR when compared to only using photo-peak events.

A second measurement was taken to compare with a high count rate case. For this comparison, a 1 mCi source was placed 48 cm in front of HEMI. As the event rate increases, the location of this false coincidence peak shifts towards shorter times, thus creating noise under the true coincidence peak. This is shown in the time spectrum plot from this measurement in Figure 6.4. This time difference spectra shows that the true coincidence peak has been

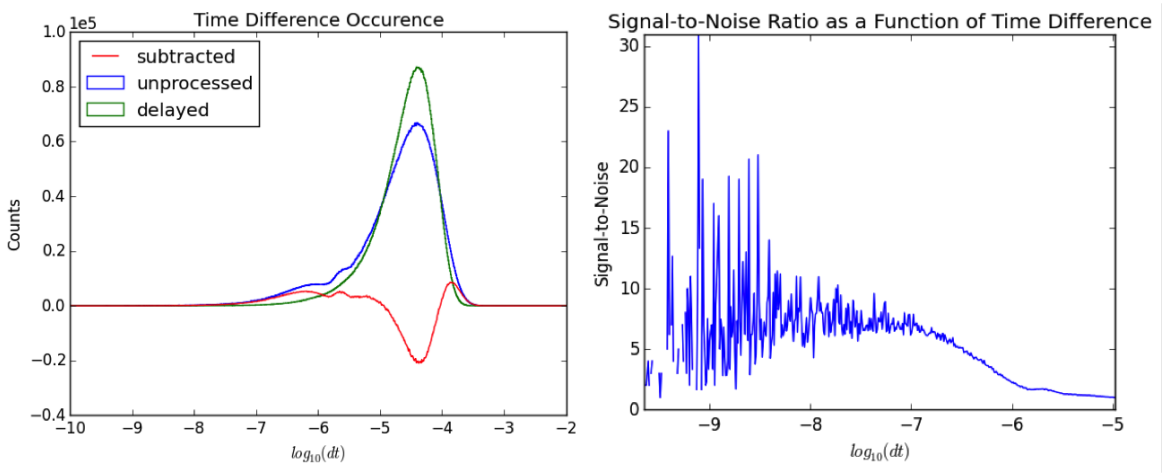

Figure 6.4: On the left, time difference histograms are shown for an unprocessed and a delayed signal. The plot on the right shows a signal-to-noise ratio (SNR) plot as a function of time difference. The SNR is computed by the ratio of the unprocessed signal to the delayed signal.

degraded by false coincidences.

As with the low count rate data, a delayed time spectra is used to estimate the true coincidence rate. The time histogram for this delayed signal is also shown in Figure 6.4 on the left figure in green. In this high count rate case, the subtracted spectra is noticeably less than the unprocessed spectra. Again this delayed signal is used to estimate the SNR as a function of time difference, which is shown in Figure 6.4 on the right. This plot shows the SNR is degraded compared to the low count rate.

As with the low count rate case, the SNR can be computed as a function of total event energy for the coincidence events as shown in Figure 6.5. This plot shows the coincidence spectra on the left, and the SNR as a function of energy on the right. The computation of SNR as a function of energy for the high count rate case shows that the SNR is degraded compared to the low count rate. For the high count rate measurement, the SNR at the 662 keV peak is 25 compared to 468 for the low count rate. However, it is not clear exactly how this will effect the image reconstruction as this degradation of SNR can be spread over the whole image and is not necessarily correlated to the source position. This can be shown by reconstructing an image from the delayed signal events.

Accounting for the false coincidence events in the image reconstruction is challenging given the list mode approach to Compton imaging. An image can be generated from the delayed, false coincidence events. This image could then be subtracted from the full signal events, however this would increase the image noise. Thus for lower count rate images where noise is already an issue, this is not a feasible approach.

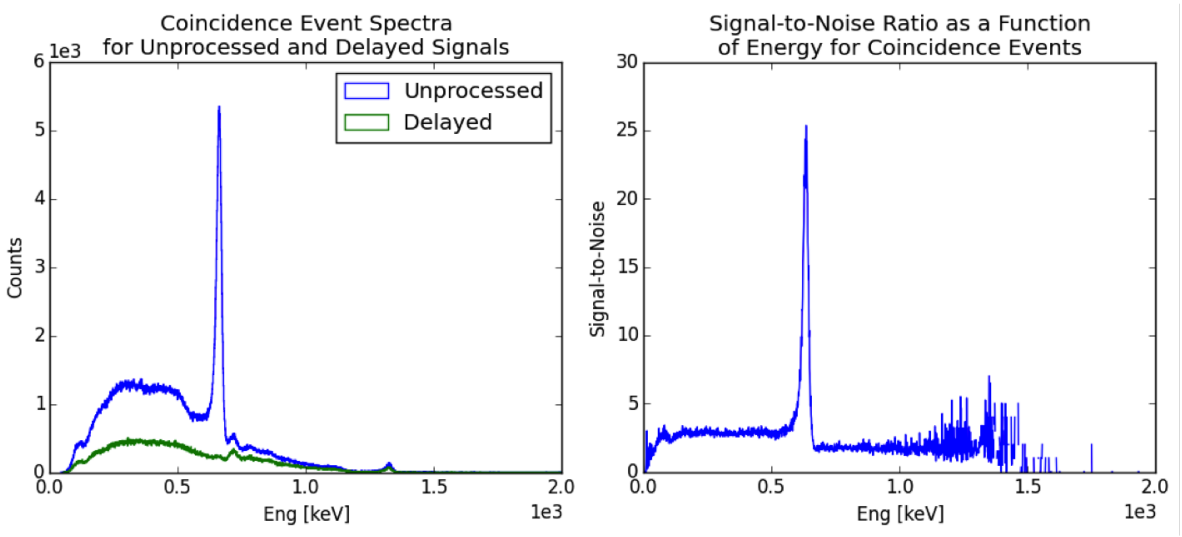

Figure 6.5: The left plot shows the coincidence spectrum for the unprocessed and delayed signals. The right plot shows the SNR as a function of energy as computed by the ratio of the unprocessed coincidence spectra to the delayed spectra. The peak in SNR occurs at the 662 keV peak.

6.3 Sampling Effect on Imaging

Section 2.5 displayed the sparseness of HEMI's scattering data sampling. A simplified simulation was done to isolate the effect of HEMI's scattering distribution on reconstructing distributed sources. To test this effect, a simple simulation was performed. In this simulation kinematics are ignored and only the geometry is considered. Thus source points are photon directions without a specific energy. When a source photon is generated, a random scattering direction is also generated. These vectors define the cone open angle. The combination of opening angle and scattering direction creates the simulated data set. The source used for this idealized simulation is uniform over a limited angular range. The sampled source distribution is depicted in Figure 6.6.

In the reference case, cones were generated with uniform scattering distributions. These events were reconstructed using the FBP method described in Ch. 3. These results are shown in Figures 6.7. Because the reconstruction surface is on a sphere, it can be depicted in 3-D space. This is shown in Figure 6.8. In this image, the bowl like structure represents the reconstructed source. The planar structure below that is a reconstruction artifact caused by the edges of the 3-D grid used for reconstruction. This does not however alter the reconstructed source because the limits of this 3-D space were far enough from the reconstruction sphere as to not alter the reconstructed source. If the grid limits are too small, this can cause biasing in the reconstruction on areas of the sphere that are close to the edge of the 3-D cube.

Now we will observe this reconstruction when HEMI's data sampling is used. For this

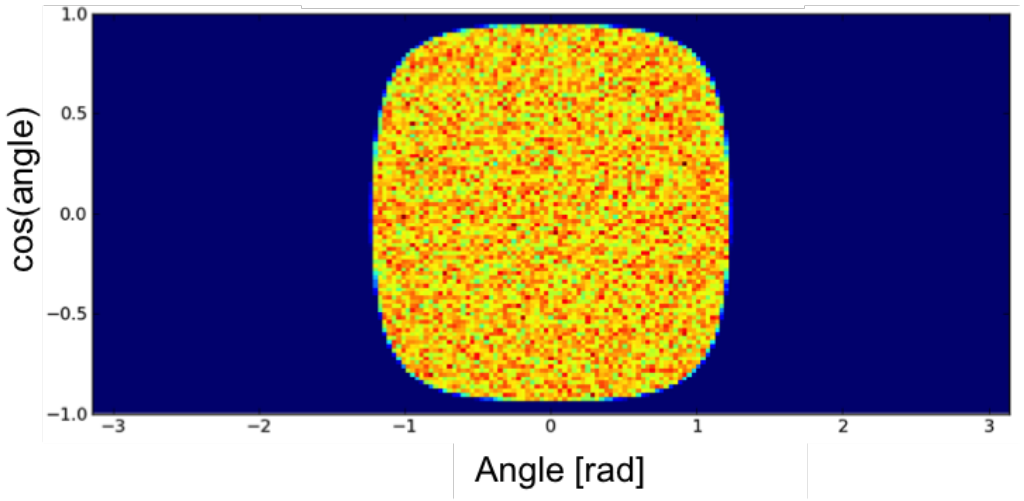

Figure 6.6: This shows the distribution of the simulated uniform angular distribution. The poisson noise is clear. The events are binned into angle versus cos(angle) space. This is used because the cos(angle) space has equal area bins.

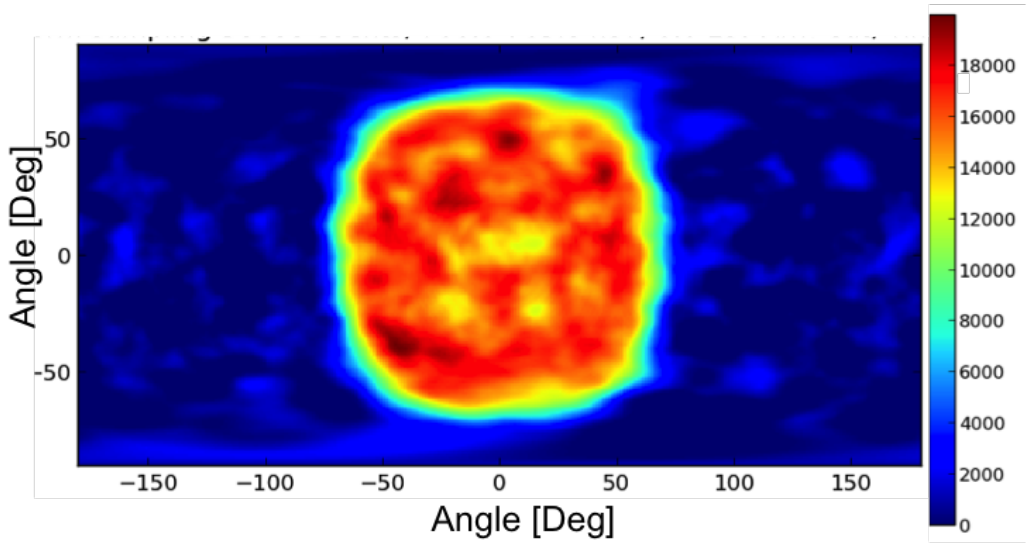

Figure 6.7: Uniform angular source reconstructed from uniform scattering angle distribution using FBP.

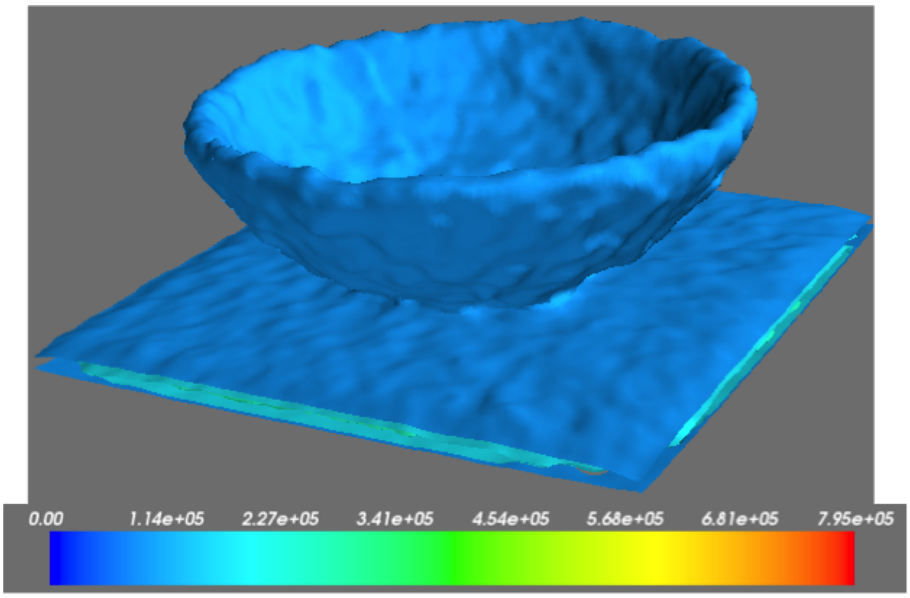

Figure 6.8: This shows a 3-D representation of the uniform source reconstruction. The bowl-like structure is from the simulated source. The planar structure below it is an artifact caused by the edges of the 3-D reconstruction grid.

case, the randomly generated scattering directions were sampled from the possible directions that HEMI can measure. A reconstruction was performed on that data with limited scattering directions and is shown in Figure 6.9. The reconstructed result from the HEMI scattering

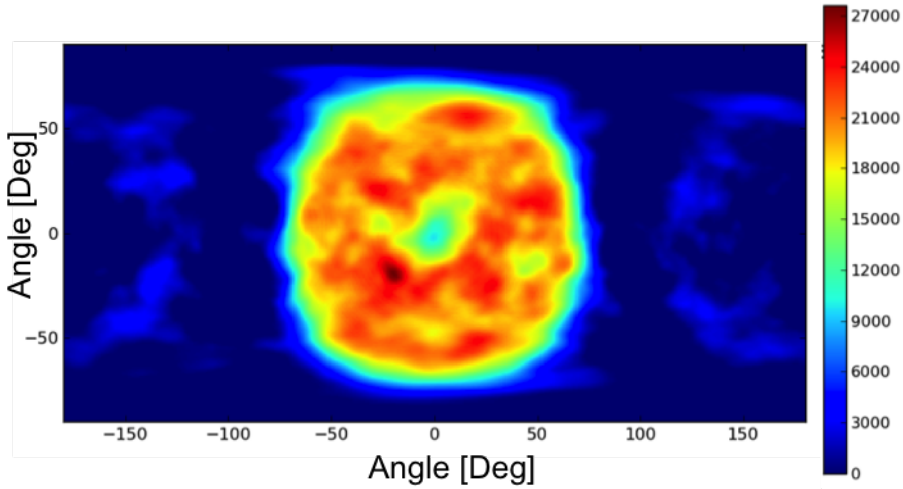

Figure 6.9: Uniform angular source reconstructed from HEMI's scattering angle distribution using FBP. This shows the reconstruction bias caused by HEMI's limited direction sampling.

distribution shows image bias not seen when the uniform scattering directions are used. Ad-

ditionally, there is some aliasing of the source in the reverse direction that is not present in the uniform scattering reconstruction. This aliasing creates correlated noise in the image, which is challenging to overcome. This is one demonstration that the scattering distributions produced by HEMI are problematic for reconstructing distributed sources. Further effort is needed to better understand the data sufficiency conditions needed for Compton telescope data.

6.4 Wavelet De-noising Reconstruction Algorithm

In this chapter thus far, it has been shown that HEMI has sampling issues. Additionally, Compton imaging measurements are often dominated by Poisson statistics from low count rate measurements. Thus a reconstruction method is desired that can account for both of these issues. It has been shown that under certain sampling conditions a function can be perfectly recovered from sampling less than the Nyqvist sampling rate. [5]. This has lead to the field of compressive sensing, which has is also especially useful for MRI applications[25]. There are two main requirements to satisfying compressive sensing. First the data must be sampled in a non-coherent pattern. Second, the desired distribution must have a sparse representation in some domain. Two popular algorithms to accomplish this are wavelet de-noising by soft thresholding [9] and total variations methods [36]. Interestingly, both of these methods were widely used before it was proven that they could exactly recover information from under-sampled signals. Implementing these methods requires optimizing a cost function. In the case of MRI, the data is modeled as Gaussian noise and thus least squares optimization methods are applicable to that imaging modality. However, Compton imaging is better modeled by Poisson statistics and thus a different approach is desired.

The wavelet transform is a basis decomposition method. It is similar to the Fourier transform in that it decomposes a signal into frequency componenets. Wavelets differ from the Fourier transform because the Fourier transform does not retain location information over the range where the transform is computer. This means that when Fourier filtering is applied to a signal, an alteration of frequencies is applied over the whole signal. This is especially consequential at high frequencies where noise and edge information are contained. Alternatively, wavelets do retain location information of frequencies. This means that they can preserve edge information in some regions and remove noise in other regions.

Many signals, especially images, have sparse wavelet coefficients. This sparcity can be used in the reconstruction method. This is acheived by using the L-1 norm on the wavelet coefficients, which enforces sparcity.

The usefulness of using wavelets with Poisson images has been discussed in [40], where wavelets were applied to photon-limited images. The wavelet transform allows for multi-level photon counting in the image, which helps reduce the noise of the reconstruction.

It is not clear if HEMI qualifies as a compressive sensing device given that its data sampling is regular in Cartesian space. However, the data space for reconstruction is actually projection vectors in 3-D space, which are not regularly spaced. Additionally, HEMI also

has random missing elements to create the coded mask in the front plane. Given that a reconstruction method is desired that can account for the Poisson statistics and the undersampling of data, a reconstruction scheme was developed to merge the conventional ML-EM approach with wavelet de-noising. The scheme is as follows:

1. Perform one iteration of ML-EM
2. Perform one iteration of wavelet soft-thresholding
3. Repeat

Wavelet soft thresholding was chosen over total variations because it can accept an image as input and output a de-noised image, whereas total variation returns a numerical value that needs to be minimized. This makes wavelet de-noising more computationally compatable with this method.

One typical approach to image reconstruction is by cost function optimization. Cost function optimization is formulated as follows:

$$f_{est} = \underset{f}{\operatorname{argmin}}\, D(g, Af) - \beta B(f) \tag{6.1}$$

Where f contains the image values, g is the data, $D(g, Af)$ is a data fidelity term, A is the projection matrix, $B(f)$ is an image regularization term, and β controls the balance between regularization and data fidelity. This cost function can then be optimized be iterative methods. For more information on such methods, see [12]. One typical choice for the data fidelity term is to use least-squares. However, this implicitly assumes Gaussian noise of the measurement, which as previously mentioned is not the best model for Compton imaging. So for the approach described here, $D(g, Af)$ will be treated as the negative Poisson log-likelihood for emission tomography. The second term encapsulates wavelet denoising, where $B(f) = ||Wf||_1$ where Wf is the wavelet transform of the reconstructed image. This is equivalent to having a Laplacian prior on the wavelet coefficients. Minimization of this term is acheived using soft-thresholding.

The approach taken here is to solve the data fidelity term and the image regularization term as two separate steps. This is achieved by alternating between minimizing each term. The data fidelity term is solved with the typical ML-EM for emission tomography iteration equation. The image regularization term is achieved using wavelet de-noising, where β is the soft thresholding cutoff level.

6.5 Rotating Source Measurement

In section 6.3, it was shown how the directional sampling effects the reconstruction of a uniform distributed source. This section attempts to demonstrate this effect with measurements from HEMI. Creating distributed sources in the lab is very challenging. To emulate

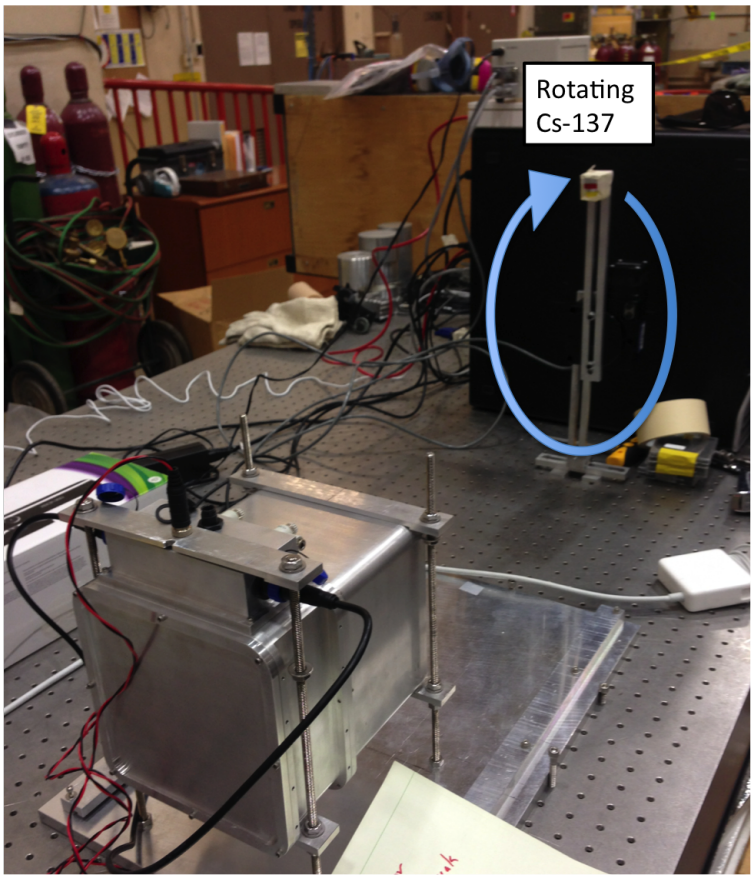

Figure 6.10: This shows the rotating source measurement setup.

an extended source in the lab, a Cs-137 point source was rotated in front of HEMI as shown in Figure 6.10. The source was placed at a distance of 22 inches with a rotation radius of 7 inches. The measurement time was 7.7 hours. An energy window with a width of 20 keV around 662 keV and a lever arm cut of 5 cm was used. This resulted in 100,515 Compton events for image reconstruction. Klein-Nishina weighting was used and both possible cone directions were input into the reconstruction algorithm. Incorporating both cone directions is important to ensure more sampling of the data. At this source distance, the near-field approximation will cause blurring of the source. However, this was used for comparison with the FBP algorithm described in Ch. 3.

The data from this extended source was reconstructed using several methods. Figure 6.11 shows the result of reconstructing the source using the FBP method described in Ch. 3. This image shows ringing artifacts that are typical of sampling issues, especially when high frequencies are missing, as is the case with HEMI.

The data was also reconstructed using standard list-mode ML-EM reconstruction. These results are shown in Figure 6.12. Interestingly, the ML-EM reconstruction still suffers from ringing present in the FBP reconstruction. The ML-EM reconstruction must be regularized

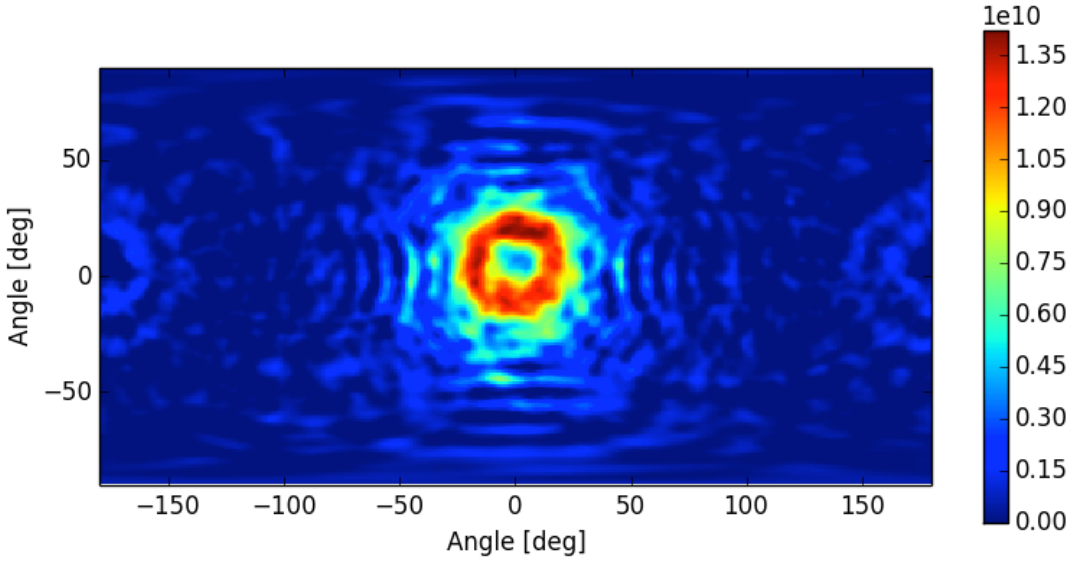

Figure 6.11: A rotating source reconstructed using FBP. For this image a lever arm cut of 5.0 cm was used with a Tikhonov value of 0.27.

in some way. In this approach, a Gaussian blurring was used after each iteration computation.

This data was then used in the hybrid wavelet ML-EM algorithm described in the previous section. The results are shown in Figure 6.13. This hybrid reconstruction has removed the imaging artifacts without blurring the reconstruction result. For this image a Daubechies 4 wavelet was used. The Haar wavelet, which is essentially a flat top wavelet, was also tested but tended to produce more artifacts by sometimes revealing the flat top. The wavelet transform was computed using an open source Python package called pyWavelets[46].

One disadvantage of the wavelet transform is that it is not shift invariant. This can be accounted for with a technique called cycle spinning. This is accomplished by applying several random cyclical-shifts to the image and computing wavelet de-noising on each. The final image is the average of each of these shifted results. This technique fits nicely with Compton imaging because the image boundaries are repeating due to the image being on the surface of a sphere. The image in Figure 6.13 used 10 random cycles at each of the 20 iterations of ML-EM.

6.6 Fukushima Results

Several measurements were taken in Fukushima over two measurement campaigns. For the measurements, HEMI was fitted with auxiliary sensors including a GPS, visual camera and onboard computer, as described in section 2.4. Reconstructing the data from these measurements proved extremely challenging. This section is intended to display some reconstruction tasks at a conceptual level and relate that to the challenges discussed thus far.

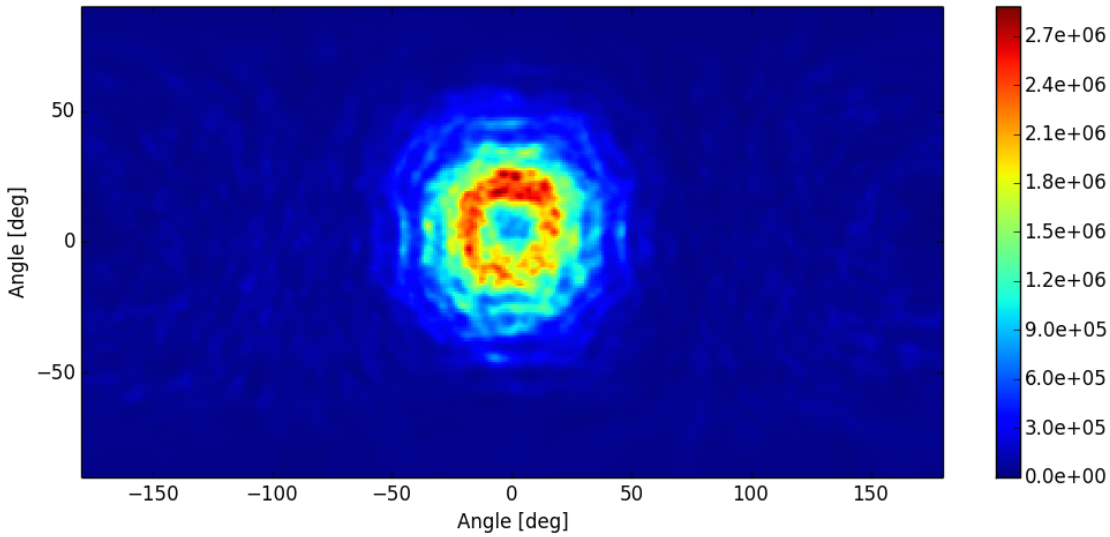

Figure 6.12: A circular source reconstructed using ML-EM is shown. 20 iterations were used with a 0.5 degree Gaussian regularizer.

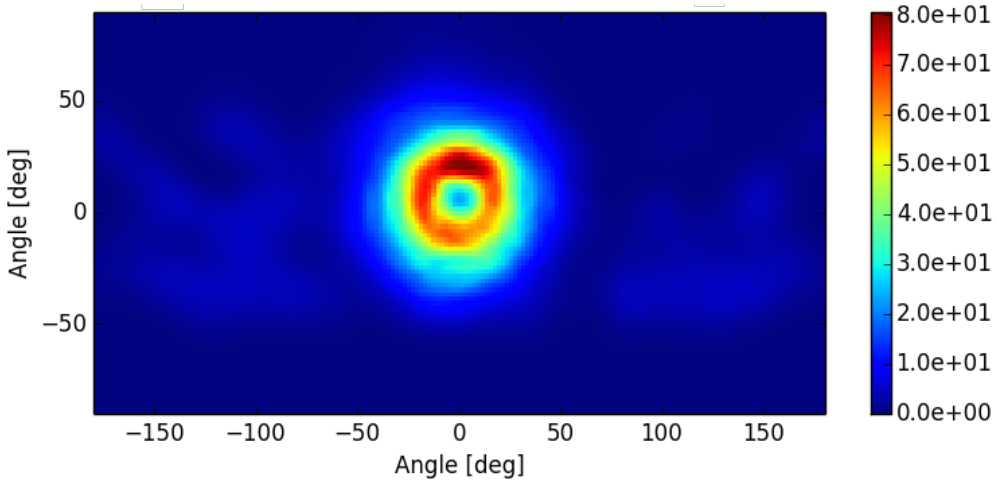

Figure 6.13: A rotating Cs-137 source reconstruction using wavelet regularized ML-EM reconstruction is shown. 20 iterations were used with a db4 wavelet and a soft-threshold value of 2.0.

Two measurement campaigns were performed in Namie, which is a town in Fukushima Prefecture, one in August 2013 and one in May 2014. In August 2013, a ground measurement was taken along with several helicopter flights. The flights from that measurement campaign will not be discussed here, but the ground measurement will. Data analysis from the 2013 flight was discussed previously [14].

For the ground measurement from August 2013, a hotspot was identified in a bush. The HEMI system was directed towards this bush in an attempt to image it from a distance. The hot source location was known, however an entire ground measurement survey was not performed. The technique described in section 6.4 was used to reconstruct the distribution of Cs-137 from the 662 keV line. A pair of reconstructed images are shown in Figure 6.14. A

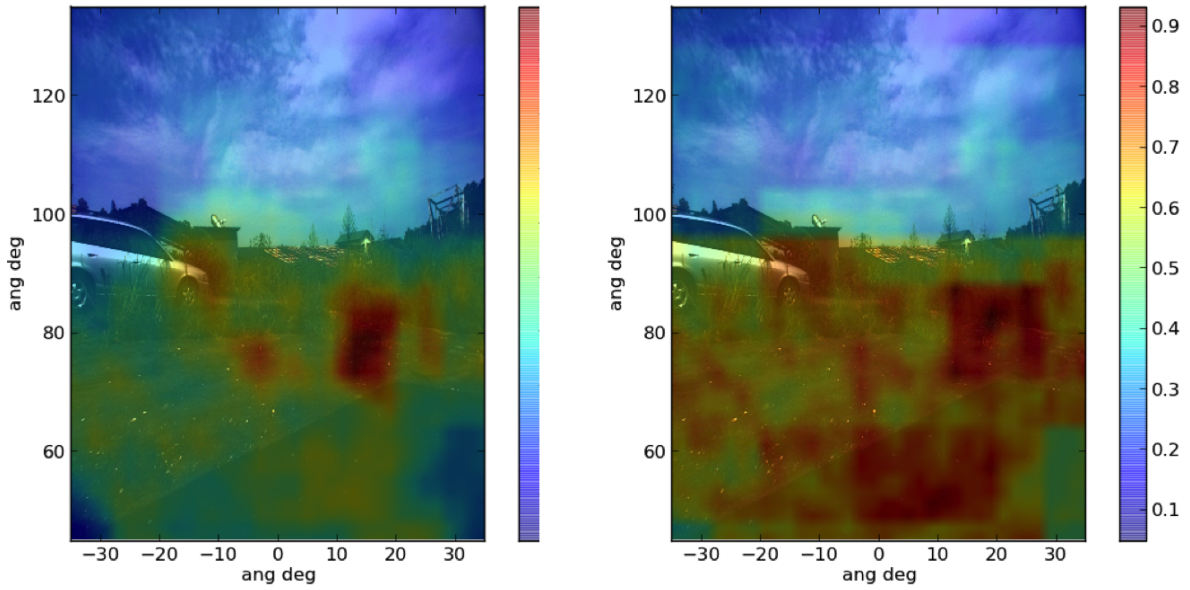

Figure 6.14: A comparison of ground reconstructions from Compton data take of a contaminated region is shown. These images are overlays of Compton image reconstructions with a visual camera image. The different images represent different cutoff values for the wavelet soft-thresholding. The image on the right has a higher cutoff value, resulting in increased noise. However, as expected, the contamination does not extend above the horizon in either image. The image on the left correctly identifies a hot spot that was measured by hand in a bush. There are 8128 events in this image and a lever arm cut of 2.5 cm was used.

DB4 wavelet was used for this reconstruction. This pair of images compares different wavelet soft-thresholding values. The left image shows a prominent hot-spot in the known location of the hot-spot found in a bush. The right image had a lower soft thresholding value and thus shows a noisier reconstruction. These images demonstrate how different thresholding values can result in structural changes in the image reconstruction. This is different than blurring based regularization methods, which create blurrier images as the regularization

parameter is increased. Further studies are needed in regard to the detection efficacy of the wavelet reconstruction method.

Using the same data and reconstruction method, another reconstruction was performed but with the use of the Haar wavelet and without cycle-spinning. This result is shown in Figure 6.15. In this reconstruction the square structure of the Haar wavelet is visible. As

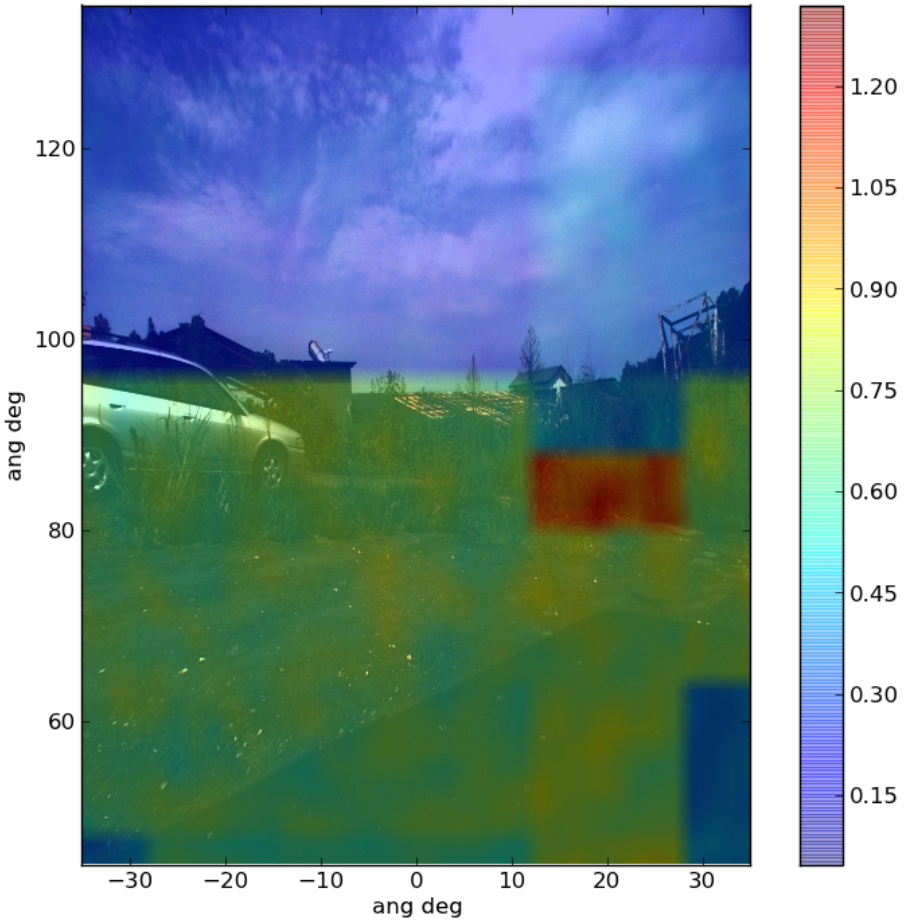

Figure 6.15: This shows a ground reconstruction using the wavelet regularized method. The square structure in the reconstruction is from the use of the Haar wavelet, which is essentially a flat top. A measured hot source is correctly located, and the diffused background contamination is also restricted to the ground regions.

was the previous reconstructions, the hotspot is correctly located. This demonstrates how the wavelet reconstruction can create anomalies when cycle-spinning is not used.

6.7 Fukushima Flight Sensor Data Fusion

This section will focus on helicopter flights taken in May 2014. For these measurements, during whcih HEMI was attached to the helicopter in Fukushima, several flight patterns were tested, including hover flights and scan flights. The results discussed here will focus on one of those scan flights, and show some of the challenges of analyzing this data, and relate it to the observations mentioned previously in this chapter. In several flights, HEMI successfully collected data continuously for nearly 4 hours, stopping only to refuel the helicopter. This demonstrates the stability of the HEMI hardware and software, which at times was operating at temperatures above 40 C as determined by a temperature sensor in the HEMI system. For the particular scan flight to be discussed here, the flight speed was 1 m/s and the total measurement time was 21.2 minutes. This measurement time compares favorably to the several days it takes to perform ground measurements by hand, which is complicated due to the river and the variety of plants in the region. The ultimate goal of these measurements is to map, in 3-D dimensions, the cesium contamination. This section describes the steps towards achieving that goal.

For the flight measurements, HEMI was fitted with a GPS and visual camera. When merging the data from multiple sensors there is a question of where in the processing pipeline the data should be fused. First we will look at some of the raw data from this scan flight measurement. The total count rate for the flight over time is shown in Figure 6.16. The

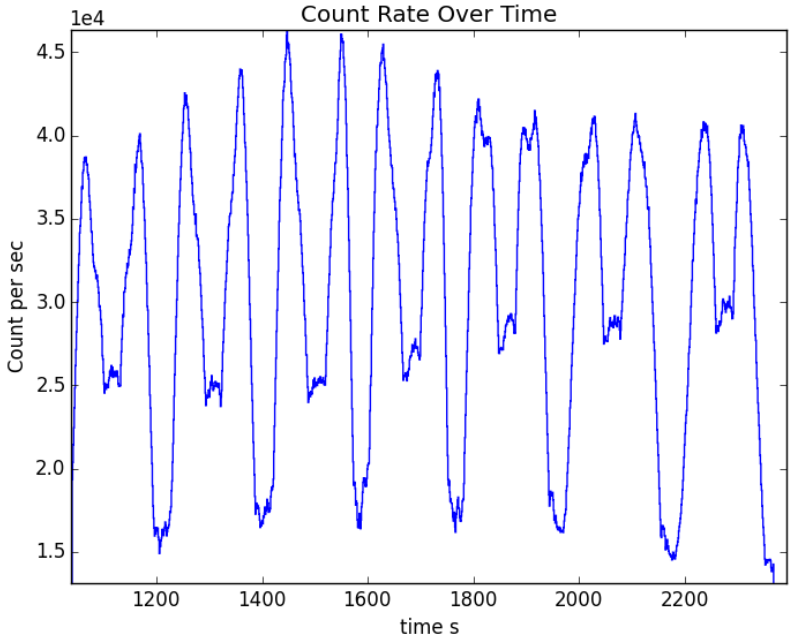

Figure 6.16: This shows the count rate changing over the time of a helicopter scan flight. This count rate is integrated over all energies.

oscilatory nature of the rate measurement during this flight is due to the helicopter passing over a hot region and a cold region. The cold region is a road where rain can wash away the cesium. The hot region is the riverbed where the cesium concentrates from water flow.

The time difference spectrum from this measurement is shown in Figure 6.17. The overlap

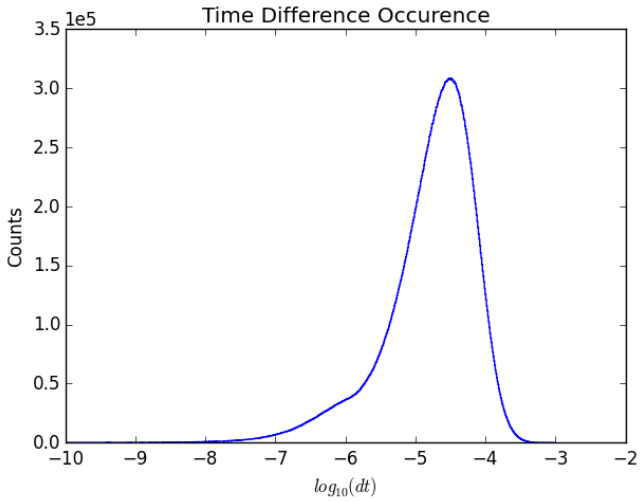

Figure 6.17: This shows the time difference spectra for a scan flight from Namie, Fukushima.

of the true coincidence peak and false coincidences is worse than observed in the lab. This figure shows the histogram for the entire flight, but this will actually change over time as the count rate changes. In particular, this effect is less severe in regions with less cesium activity and therfore lower count rate.

The energy spectra from coincidence events is shown in Figure 6.18. This spectra shows three prominent peaks at 605 keV, 662 keV and 796 keV. The 662 keV line is from Cs-137 and the other two lines are from Cs-134. This spectra displays another challenge with imaging Cs contamination from this data. The 662 keV line is the most prominent, but also contains down-scatter events from higher energies. Specifically, higher energy events deposit a fraction of there energy totaling 662 keV and thus are indistinguishable from actual 662 keV source events.

Having observed some of the raw data, the rest of this section is dedicated to discussions about the actual data fusion. The GPS data can be used with Google earth data to globally position the measurements. Google earth provides a smoothed version of the ground plane that does not include small scale features such as trees or the river bed height. This count rate data can be merged with GPS data to show the change in Cs count rate over space. This can then be interpolated and is shown in Figure 6.19. This figure also shows the flight pattern taken by the helicopter. A river runs through the center of this region. From ground surveys, the area north of the river was known to have higher activity levels than the area south of the river. This mapping of coincidence 662 keV count rate roughly correlates with that knowledge. One approach to improve this mapping would be to perform background

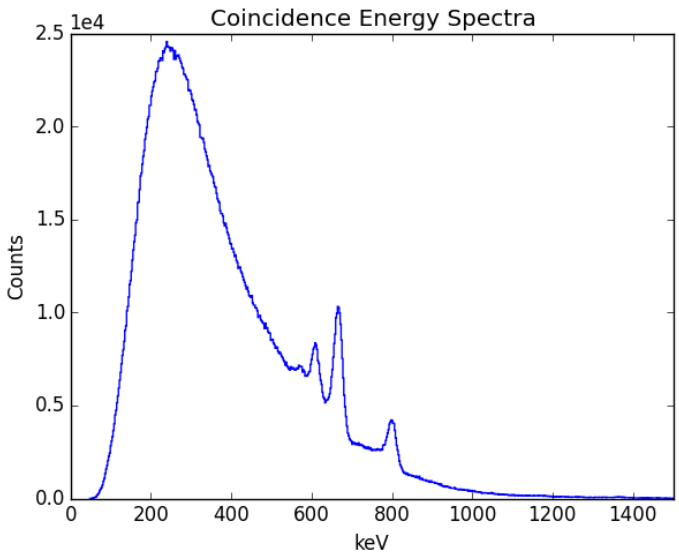

Figure 6.18: This shows the coincidence event energy spectrum for the scan flight, limited to only the actual scan region.

subtraction. However, that background subtraction would need to be a function of time and could increase the noise of this already noisy result. The streaking artifacts in this data are due to the measurement noise combined with the wide flight paths. The known location of three hot-spots is indicated by the green dots in this plot. The heat-map does not correlate very well with these hot spots. This observation lead to the hypothesis that there was contamination in the trees that was contributing to these heat maps. However, at this time the exact cause of this discrepancy is not know. This reveals one limitation of this method of only using GPS data, that it does not take into account the detailed geometry of the objects below the helicopter, and thus cannot account for the trees being closer to the measurement system. This will lead to the system being more sensitive to objects that are closer. This reveals the need to dig deeper into the data streams and try to extract more fine levels of spatial information.

To accomplish a finer level of accuracy, the visual camera data can be used. Pictures were take at a rate of 2 Hz and then used to reconstruct the ground. This serves two purposes, to reconstruct the ground geometry and to position the detector system in the scene. This position includes a translation and rotation. Using time syncing from the onboard computer, the Compton coincidence data can then be correlated to a pose estimate determined from the visual reconstruction. This is useful because of the trees on the ground have unknown radiation levels. Thus visually reconstructing them could lead to determining their contamination levels from air measurements. To perform this reconstruction a general technique of struction from motion (SFM) was used. The ground was reconstructed using a software package called VisualSFM [49]. The general approach to this visual reconstruction

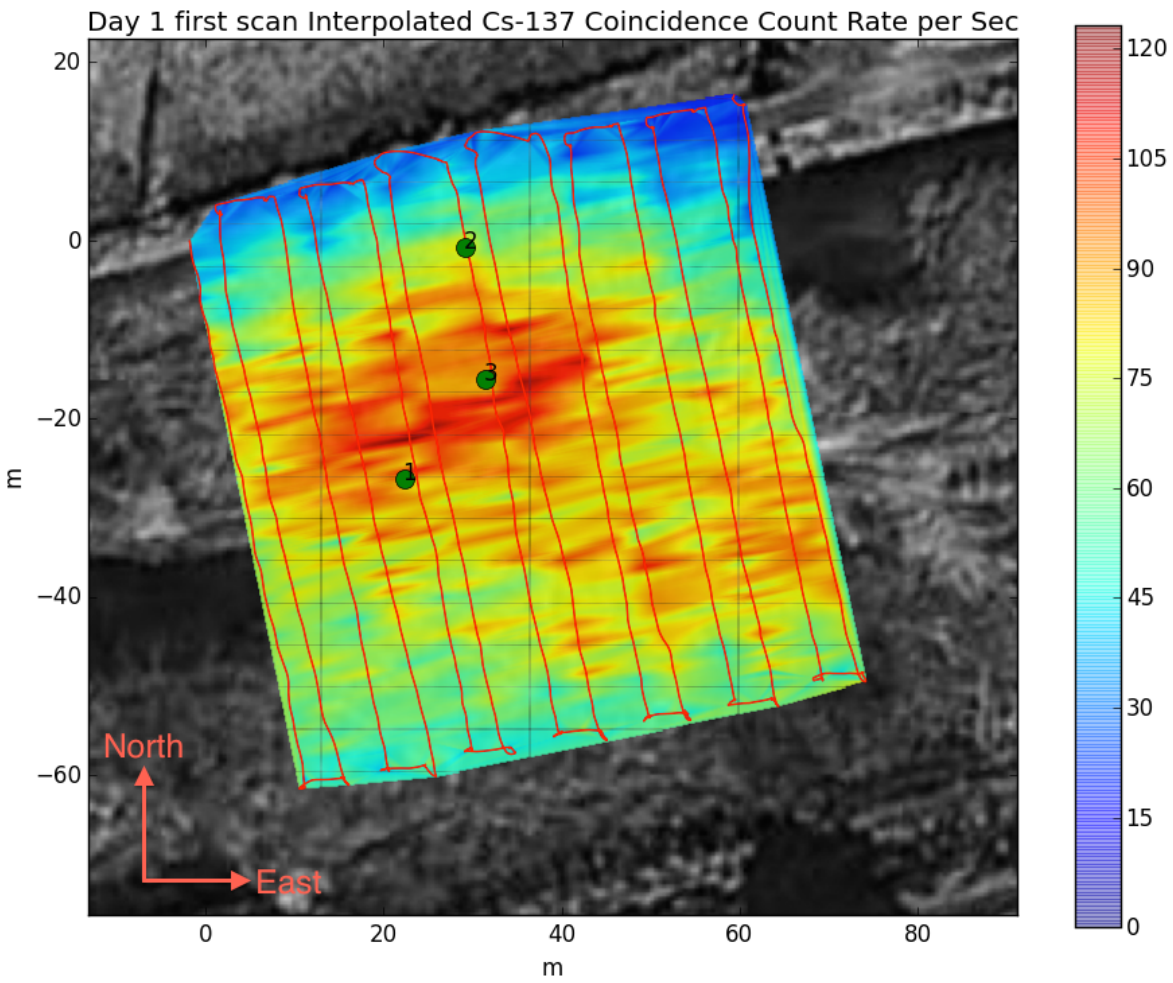

Figure 6.19: An interpolated map of Cs-137 activity from the 662 keV coincidence count rate is shown. The three green dots are from coordinates of known hotspots that were found by doing ground surveys of this area by hand. The red line is the path the helicopter flew, as determined by the GPS data.

technique is as follows:

- Find key-points in each image
- Determined which key-points match across different images
- Compute the transform that relates these images
- After several of these transforms are computed, bundle adjustment is performed to improve the pose estimates

This method does not use the GPS as prior information and is very general for an arbitrary set of images of a scene. This is a sparse reconstruction method that results in a set of 3-D spatial points, as opposed to a dense reconstruction that would provide triangulated surfaces. However, for the purpose of correlating the visual data to gamma ray reconstructed data, this sparse reconstruction is sufficient. The length scale that results from this method is arbitrary, but the actual scale could be determined by correlating with the GPS data. The resulting visual reconstruction is shown in Figure 6.20. This picture shows that the visual

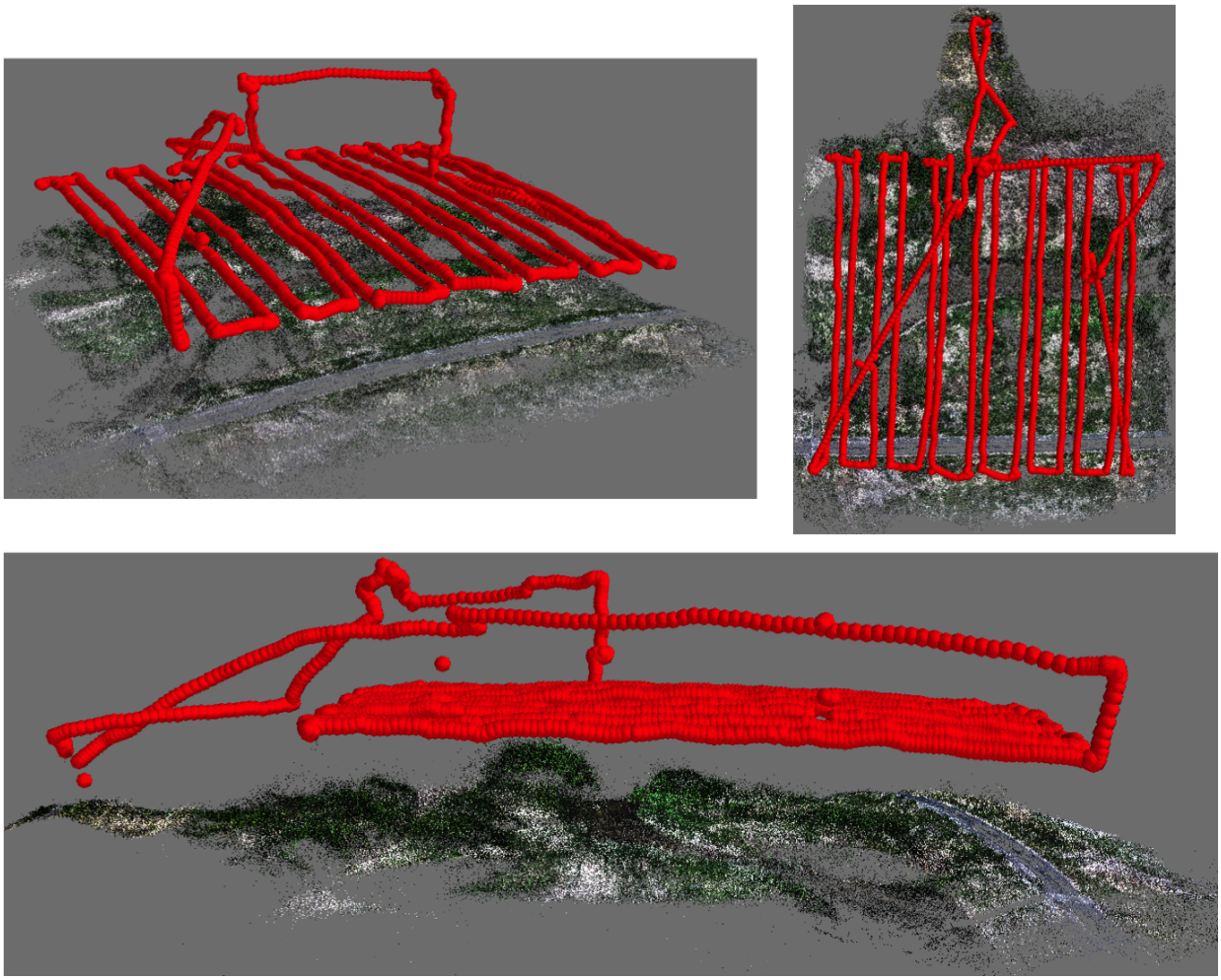

Figure 6.20: This shows multiple perspectives of a 3-D visual reconstruction from the images taken on the helicopter that flew HEMI. The red circles represent the pose estimate for each camera frame.

reconstruction recovered the tree structures in the scene. This result also demonstrates the robustness of this reconstruction method because the helicopter was actually causing the trees to move from the airflow generated from the rotors, so the tree structure was not static throughout the flight.

Now that the visual data is available for the gamma-ray emitter reconstruction, we shift focus to incorporating this data with the Compton scattered data. Similarly to the gamma-ray reconstruction method used in Ch. 5, a voxelized space is constructed around the visual point cloud. This voxelized space is then limited to the voxels where visual point clouds are contained. The back-projection of Compton cones can then be computed in these voxels. This back-projection is shown in Figures 6.21 and 6.22.

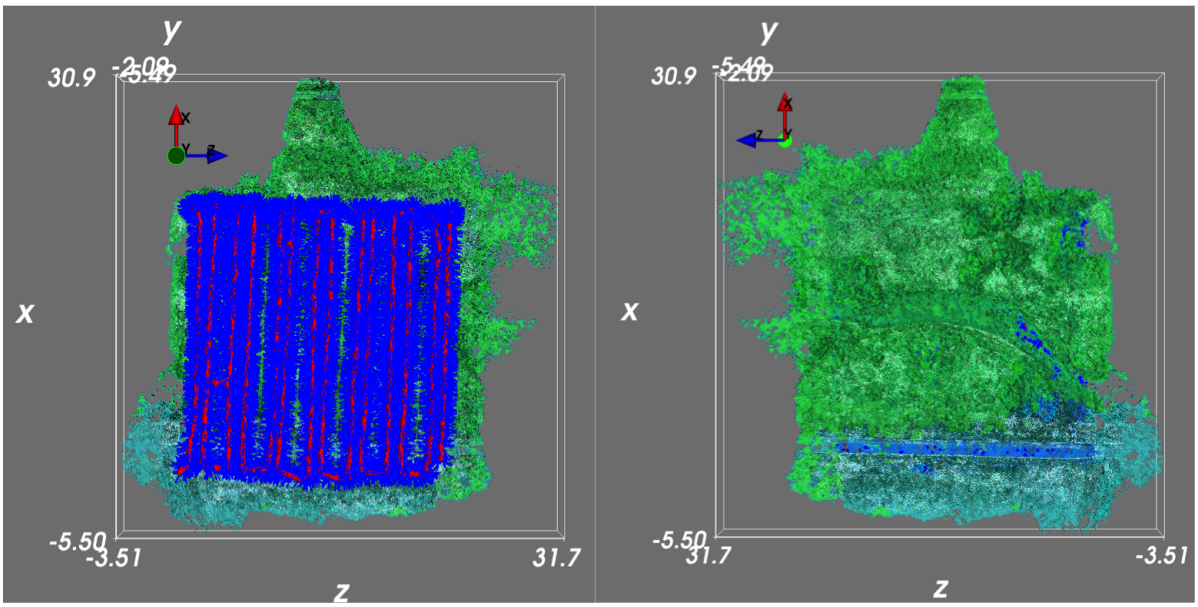

Figure 6.21: This shows a top and bottom view of the merging of Compton cone back-projection with a visual reconstruction. The spatial units are arbitrary pixel values that result from VisualSFM. The top down plot on the left shows the path the helicopter flew where the red lines represent the path. The blue lines around this are individual Compton scatters used for the reconstruction. The blue regions have lower back-projection levels than the green regions.

In this back-projection, the road is not as hot as the rest of the region as expected. However, finite details of the reconstruction do no reveal the known hotspots because the back-projection has artificially poor resolution. Further studies are needed to accurately reconstruct the ground from this data. Also, it is not clear what the reconstruction should produce. This is the case because it is not clear how the reconstruction should match ground measurements, especially considering that the ground measurements did not include surveys of the tress. It is also possible that the count rate from this measurement is too low. Additionally, more research is needed to determine the best methods to account for all the effects described early in this chapter in the reconstruction method. And thus, as is often the case in research, these measurements have opened more questions that need to be answered. But at least those questions are more specific as a result of this work.

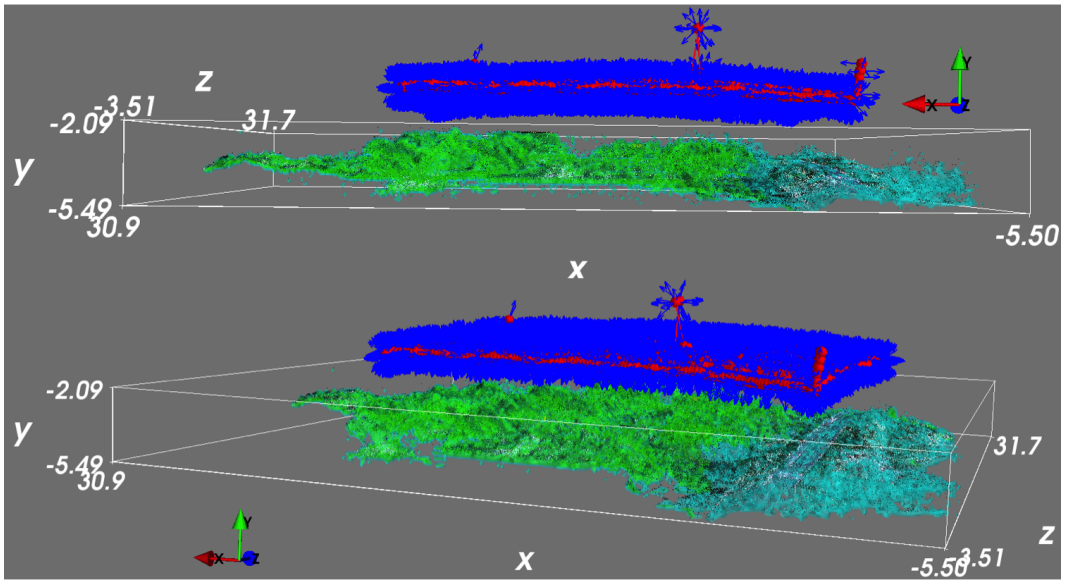

Figure 6.22: This shows a side views of the merging of Compton cone back-projection with a visual reconstruction.

Chapter 7

Conclusions and Future Directions

This work demonstrated several advancements for Compton imaging. At the data level, techniques were shown to analyze the quality of Compton imaging data. More work should be done to better understand the data sufficiency conditions for Compton imaging. Some of these analysis techniques are useful for isolating specific issues related to imaging. These analysis techniques need to be extend so they can be used to improve the image reconstruction, especially for reconstructing the contamination levels in Fukushima, Japan. Progress towards this reconstruction was shown, however more future research is needed to better quantify the limits and capabilities of such an approach.

The importance of data sampling was demonstrated with extended source measurements with HEMI and CCI2. The wavelet regularized algorithm was detailed that can help deal with some of sampling issues with HEMI. Future work is needed to further push the limits of HEMI's imaging capabilities, especially in complex real-world scenarios.

At the physics level, an algorithm was demonstrated to reconstruct gamma-ray flux distributions from electron trajectories. Future work related to this algorithm is in testing the simultaneous imaging of different source energies. Also, this algorithm should be tested with different detection systems, especially gas based systems.

A simplified FBP algorithm was shown that related the Radon transform to Compton image reconstruction. Further work on this algorithm includes quantifying which weighting factors have the highest impact on image reconstruction. Also this method can be used to analyze the noise characteristics of the reconstruction.

Overall, these approaches to Compton imaging are quite varied. As was mentioned in the first chapter, the ultimate goal of this variety of approaches is to move further towards the ideal case of 6-D gamma-ray imaging.

Appendix A

Acronyms

ARM Angular Resolution Measure - A measure of a Compton camera's resolution. It is computed by using a point source with a known location.

CCD Charged Coupled Device

CCI2 Compact Compton Imager 2 - A HPGe based Compton Imaging system with visual auxiliary sensors.

FBP Filtered Back-Projection - In general, an analytic approach to image reconstruction based on Fourier filtering.

HEMI High Efficiency Multi-mode Imager - A CdZiTe based Compton imaging system.

ML-EM Maximum-Likelihood Expectation-Maximization

PSF Point Spread Function

SFM Structure from Motion

SLAM Simultaneous Localization and Mapping

Bibliography

[1] MS Bandstra et al. "Detection and imaging of the Crab nebula with the nuclear Compton telescope". In: *The Astrophysical Journal* 738.1 (2011), p. 8.

[2] Ross Barnowski. "Private Communication".

[3] Harrison H Barrett, Timothy White, and Lucas C Parra. "List-mode likelihood". In: *JOSA A* 14.11 (1997), pp. 2914–2923.

[4] Stefan Behnel et al. "Cython: The best of both worlds". In: *Computing in Science & Engineering* 13.2 (2011), pp. 31–39.

[5] Emmanuel J Candès, Justin Romberg, and Terence Tao. "Robust uncertainty principles: Exact signal reconstruction from highly incomplete frequency information". In: *Information Theory, IEEE Transactions on* 52.2 (2006), pp. 489–509.

[6] D. H. Chivers et al. "Impact of measuring electron tracks in high-resolution scientific charge-coupled devices within Compton imaging systems". In: *Nuclear Instruments and Methods in Physics Research Section A: Accelerators, Spectrometers, Detectors and Associated Equipment* 654.1 (Oct. 2011), pp. 244–249. URL: `http://www.sciencedirect.com/science/article/pii/S0168900211011570`.

[7] Alvaro R De Pierro. "A modified expectation maximization algorithm for penalized likelihood estimation in emission tomography." In: *IEEE Transactions on Medical Imaging* 14.1 (1994), pp. 132–137.

[8] Roland Diehl et al. "COMPTEL observations of Galactic^ 26^ Al emission." In: *Astronomy and Astrophysics* 298 (1995), p. 445.

[9] David L Donoho. "De-noising by soft-thresholding". In: *Information Theory, IEEE Transactions on* 41.3 (1995), pp. 613–627.

[10] Nikolas Engelhard et al. "Real-time 3D visual SLAM with a hand-held RGB-D camera". In: *Proc. of the RGB-D Workshop on 3D Perception in Robotics at the European Robotics Forum*. Vasteras, Sweden, 2011.

[11] Jeffrey A Fessler. "Penalized weighted least-squares image reconstruction for positron emission tomography". In: *Medical Imaging, IEEE Transactions on* 13.2 (1994), pp. 290–300.

[12] Jeffrey A Fessler and ISBI Tutorial. "Iterative methods for image reconstruction". In: *IEEE International Symposium on Biomedical Imaging Tutorial, Arlington Virginia*. 2006.

[13] Michelle Galloway et al. "Simulation and detector response for the High Efficiency Multimode Imager". In: *Nuclear Instruments and Methods in Physics Research Section A: Accelerators, Spectrometers, Detectors and Associated Equipment* 652.1 (2011). Symposium on Radiation Measurements and Applications (SORMA) {XII} 2010, pp. 641 –645. ISSN: 0168-9002. DOI: http://dx.doi.org/10.1016/j.nima.2010.08.101. URL: http://www.sciencedirect.com/science/article/pii/S0168900210018887.

[14] Michelle L Galloway. "Characterization and Applications of a CdZnTe-Based Gamma-Ray Imager". PhD thesis. UC Berkeley, 2014.

[15] Michelle L Galloway et al. "Status of the High Efficiency Multimode imager". In: *Nuclear Science Symposium and Medical Imaging Conference (NSS/MIC), 2011 IEEE*. IEEE. 2011, pp. 1290–1293.

[16] Donald L Gunter. *Filtered back-projection algorithm for compton telescopes*. US Patent 7,345,283. 2008.

[17] A. Haefner et al. "Gamma-ray momentum reconstruction from Compton electron trajectories by filtered back-projection". In: *Applied Physics Letters* 105.18, 184101 (2014), pp. –. DOI: http://dx.doi.org/10.1063/1.4898087. URL: http://scitation.aip.org/content/aip/journal/apl/105/18/10.1063/1.4898087.

[18] Stephen E Holland et al. "Fully depleted, back-illuminated charge-coupled devices fabricated on high-resistivity silicon". In: *Electron Devices, IEEE Transactions on* 50.1 (2003), pp. 225–238.

[19] John D Hunter. "Matplotlib: A 2D graphics environment". In: *Computing in Science & Engineering* 9.3 (2007), pp. 0090–95.

[20] J Kataoka et al. "Handy Compton camera using 3D position-sensitive scintillators coupled with large-area monolithic MPPC arrays". In: *Nuclear Instruments and Methods in Physics Research Section A: Accelerators, Spectrometers, Detectors and Associated Equipment* 732 (2013), pp. 403–407.

[21] I.Y. Lee. "Gamma-ray tracking detectors". In: *Nuclear Instruments and Methods in Physics Research Section A: Accelerators, Spectrometers, Detectors and Associated Equipment* 422.1–3 (1999), pp. 195 –200. ISSN: 0168-9002. DOI: http://dx.doi.org/10.1016/S0168-9002(98)01093-6. URL: http://www.sciencedirect.com/science/article/pii/S0168900298010936.

[22] IY Lee et al. "GRETINA: A gamma ray energy tracking array". In: *Nuclear Physics A* 746 (2004), pp. 255–259.

[23] C.E. Lehner, Zhong He, and Feng Zhang. "4 pi; Compton imaging using a 3-D position-sensitive CdZnTe detector via weighted list-mode maximum likelihood". In: *Nuclear Science, IEEE Transactions on* 51.4 (2004), pp. 1618–1624. ISSN: 0018-9499. DOI: 10.1109/TNS.2004.832573.

[24] P Ni Luke. "Single-polarity charge sensing in ionization detectors using coplanar electrodes". In: *Applied Physics Letters* 65.22 (1994), pp. 2884–2886.

[25] Michael Lustig, David Donoho, and John M Pauly. "Sparse MRI: The application of compressed sensing for rapid MR imaging". In: *Magnetic resonance in medicine* 58.6 (2007), pp. 1182–1195.

[26] Nicholas Mascarenhas et al. "Results with the neutron scatter camera". In: *Nuclear Science, IEEE Transactions on* 56.3 (2009), pp. 1269–1273.

[27] Lucian Mihailescu, Kai Vetter, and Daniel Chivers. "Standoff 3D gamma-ray imaging". In: *Nuclear Science, IEEE Transactions on* 56.2 (2009), pp. 479–486.

[28] Shinji Motomura et al. "Gamma-ray Compton imaging of multitracer in biological samples using strip germanium telescope". In: *Nuclear Science, IEEE Transactions on* 54.3 (2007), pp. 710–717.

[29] Lucas C Parra. "Reconstruction of cone-beam projections from Compton scattered data". In: *Nuclear Science, IEEE Transactions on* 47.4 (2000), pp. 1543–1550.

[30] Fernando Perez and Brian E Granger. "IPython: a system for interactive scientific computing". In: *Computing in Science & Engineering* 9.3 (2007), pp. 21–29.

[31] *PHDS Gamma-ray Imaging Detectors*. URL: http://www.phdsco.com/products/gegi/specs.

[32] Brian Plimley et al. "Reconstruction of electron trajectories in high-resolution Si devices for advanced Compton imaging". In: *Nuclear Instruments and Methods in Physics Research Section A: Accelerators, Spectrometers, Detectors and Associated Equipment* 652.1 (2011). Symposium on Radiation Measurements and Applications (SORMA) {XII} 2010, pp. 595 –598. ISSN: 0168-9002. DOI: http://dx.doi.org/10.1016/j.nima.2011.01.133. URL: http://www.sciencedirect.com/science/article/pii/S016890021100235X.

[33] *Polaris-H Imaging Spectrometer for Nuclear Power Plants*. URL: http://www.h3dgamma.com/nuclearProducts.html.

[34] Prabhu Ramachandran and Gaël Varoquaux. "Mayavi: 3D visualization of scientific data". In: *Computing in Science & Engineering* 13.2 (2011), pp. 40–51.

[35] M-H Richard et al. "Design study of a Compton camera for prompt γ imaging during ion beam therapy". In: *Nuclear Science Symposium Conference Record (NSS/MIC), 2009 IEEE*. IEEE. 2009, pp. 4172–4175.

[36] Leonid I Rudin, Stanley Osher, and Emad Fatemi. "Nonlinear total variation based noise removal algorithms". In: *Physica D: Nonlinear Phenomena* 60.1 (1992), pp. 259–268.

[37] Lawrence A Shepp and Yehuda Vardi. "Maximum likelihood reconstruction for emission tomography". In: *Medical Imaging, IEEE Transactions on* 1.2 (1982), pp. 113–122.

[38] A. Takada et al. "Development of an advanced Compton camera with gaseous TPC and scintillator". In: *Nuclear Instruments and Methods in Physics Research Section A: Accelerators, Spectrometers, Detectors and Associated Equipment* 546.1–2 (July 2005), pp. 258–262. URL: http://www.sciencedirect.com/science/article/pii/S0168900205006625.

[39] S. Takeda et al. "Demonstration of in-vivo Multi-Probe Tracker Based on a Si/CdTe Semiconductor Compton Camera". In: *Nuclear Science, IEEE Transactions on* 59.1 (2012), pp. 70–76. ISSN: 0018-9499. DOI: 10.1109/TNS.2011.2178432.

[40] Klaus E Timmermann and Robert D Nowak. "Multiscale modeling and estimation of Poisson processes with application to photon-limited imaging". In: *Information Theory, IEEE Transactions on* 45.3 (1999), pp. 846–862.

[41] R. W. TODD, J. M. NIGHTINGALE, and D. B. EVERETT. "A proposed [gamma] camera". In: *Nature* 251.5471 (Sept. 1974), pp. 132–134. URL: http://dx.doi.org/10.1038/251132a0.

[42] Heang K Tuy. "An inversion formula for cone-beam reconstruction". In: *SIAM Journal on Applied Mathematics* 43.3 (1983), pp. 546–552.

[43] K. Vetter et al. "First demonstration of electron-tracking based Compton imaging in solid-state detectors". In: *Nuclear Instruments and Methods in Physics Research Section A: Accelerators, Spectrometers, Detectors and Associated Equipment* 652.1 (2011). Symposium on Radiation Measurements and Applications (SORMA) {XII} 2010, pp. 599 –601. ISSN: 0168-9002. DOI: http://dx.doi.org/10.1016/j.nima.2011.01.131. URL: http://www.sciencedirect.com/science/article/pii/S0168900211002336.

[44] K. Vetter et al. "High-sensitivity Compton imaging with position-sensitive Si and Ge detectors". In: *Nuclear Instruments and Methods in Physics Research Section A: Accelerators, Spectrometers, Detectors and Associated Equipment* 579.1 (2007). Proceedings of the 11th Symposium on Radiation Measurements and Applications, pp. 363 –366. ISSN: 0168-9002. DOI: http://dx.doi.org/10.1016/j.nima.2007.04.076. URL: http://www.sciencedirect.com/science/article/pii/S0168900207006481.

[45] Weiyi Wang et al. "Maximum-likelihood deconvolution in the spatial and spatial-energy domain for events with any number of interactions". In: *Nuclear Science, IEEE Transactions on* 59.2 (2012), pp. 469–478.

[46] F Wasilewski. *PyWavelets: Discrete Wavelet Transform in Python*. 2010.

[47] Shin Watanabe et al. "A si/cdte semiconductor compton camera". In: *Nuclear Science, IEEE Transactions on* 52.5 (2005), pp. 2045–2051.

[48] Scott J Wilderman et al. "List-mode maximum likelihood reconstruction of Compton scatter camera images in nuclear medicine". In: *Nuclear Science Symposium, 1998. Conference Record. 1998 IEEE*. Vol. 3. IEEE. 1998, pp. 1716–1720.

[49] Changchang Wu. "Visualsfm: A visual structure from motion system". In: *http://ccwu.me/vsfm/* (2011).

[50] D. Xu and Z. He. "Gamma-ray energy-imaging integrated spectral deconvolution". In: *Nuclear Instruments and Methods in Physics Research Section A: Accelerators, Spectrometers, Detectors and Associated Equipment* 574.1 (2007), pp. 98 –109. ISSN: 0168-9002. DOI: http://dx.doi.org/10.1016/j.nima.2007.01.171. URL: http://www.sciencedirect.com/science/article/pii/S0168900207002549.

[51] Dan Xu. "Gamma-ray imaging and polarization measurement using 3-D position- sensitive CdZnTe detectors". PhD thesis. Ann Arbor, MI: University of Michigan, 2006.

[52] Dan Xu et al. "4-pi Compton imaging with single 3D position-sensitive CdZnTe detector". In: *Optical Science and Technology, the SPIE 49th Annual Meeting*. International Society for Optics and Photonics. 2004, pp. 144–155.

[53] A. Zoglauer, R. Andritschke, and G. Kanbach. "Data analysis for the MEGA prototype". In: *New Astronomy Reviews* 48.1–4 (Feb. 2004), pp. 231–235. URL: http://www.sciencedirect.com/science/article/pii/S1387647303003105.

[54] A. Zoglauer, R. Andritschke, and F. Schopper. "MEGAlib–The medium energy gamma-ray astronomy library". In: *New Astronomy Reviews* 50.7 (2006), pp. 629–632.

[55] Andreas Zoglauer. "First light for the next generation of Compton and pair telescopes: Development of new techniques for the data analysis of combined Compton and pair telescopes and their application to the MEGA prototype". PhD thesis. 2006.

[56] Andreas Zoglauer and Gottfried Kanbach. *Doppler broadening as a lower limit to the angular resolution of next-generation Compton telescopes*. 2003. DOI: 10.1117/12.461177. URL: http://dx.doi.org/10.1117/12.461177.

[57] Andreas Zoglauer et al. "First results of the high efficiency multi-mode imager (HEMI)". In: *Nuclear Science Symposium Conference Record (NSS/MIC), 2009 IEEE*. IEEE. 2009, pp. 887–891.